KU LEUVEN

ARENBERG DOCTORAL SCHOOL
Faculty of Science

Beta-delayed fission in proton-rich nuclei in the lead region

CERN-THESIS-2015-234
01/09/2015

Lars Ghys

Supervisor:
Prof. Dr. P. Van Duppen
Prof. Dr. M. Huyse, co-supervisor
Dr. L. Popescu, co-supervisor
(SCK•CEN)

Dissertation presented in partial fulfillment of the requirements for the degree of Doctor in Science

September 2015

Beta-delayed fission in proton-rich nuclei in the lead region

Lars GHYS

Examination committee:
Prof. Dr. N. Severijns, chair
Prof. Dr. P. Van Duppen, supervisor
Prof. Dr. M. Huyse, co-supervisor
Dr. L. Popescu, co-supervisor
(SCK•CEN)
Prof. Dr. L. C. Pereira
Prof. Dr. R. Raabe
Prof. Dr. M. J. Van Bael
Prof. Dr. A. N. Andreyev
(University of York, UK)

Dissertation presented in partial fulfillment of the requirements for the degree of Doctor in Science

September 2015

Uitgegeven in eigen beheer, Lars Ghys, Celestijnenlaan 200D box 2418, B-3001 Heverlee (Belgium)

Dit werk kwam mede tot stand met steun van het

Fonds voor Wetenschappelijk Onderzoek (FWO) Vlaanderen.

Dankwoord

Deze thesis kon alleen tot stand komen door de hulp en ondersteuning van velen gedurende de afgelopen vier jaar en dit op allerlei verschillende manieren. Iedereen bedanken zou dus een onmogelijke taak zijn, maar hieronder zou ik toch graag een aantal personen in het bijzonder willen aanhalen die cruciaal waren om dit werk tot een goed einde te brengen.

First and foremost, I would like to thank my promotor Piet Van Duppen and co-promotors Mark Huyse and Lucia Popescu for giving me the opportunity to participate in this interesting research on an international level. Despite your busy agendas, your doors were always open for stimulating discussions, which were invaluable for this work.

A special thanks goes to the other members of the examination committee - Nathal Severijns, Lino da Costa Pereira, Riccardo Raabe, Margriet Van Bael and Andrei Andreyev - for carefully reading this thesis and the fruitful discussions during the preliminary defense.

The experiments on which this thesis is based, were carried out with the help of an international team from different institutions. The whole IS466-III and IS534 collaboration is therefore warmly acknowledged for their support before, during and after the experiments.

Het IKS vormde gedurende de afgelopen jaren een aangename werkplek, onder andere door de gratis koffie, maar vooral door de vele toffe collega's. Dankzij deze laatsten was er een leuke sfeer op kantoor en tijdens de lange (nachtelijke) shiften in Louvain-la-Neuve of CERN.
Bedankt Simon, Jytte, Céline, Jan en Nele voor de toffe momenten tijdens en na het werk. Het was ook met veel plezier dat ik Simon en André heb laten winnen met het squashen tijdens de middagen. Also the runs with Sara, Nuno,

Philip, Daniel and other IKS colleagues were an ideal distraction from work. Bedankt ook aan Isabelle, Danielle en Fabienne van het secretariaat voor de hulp bij allerlei praktische zaken, aan Bert en Luc voor het oplossen van allerhande computer-gerelateerde problemen en aan Willy voor het maken van mechanische onderdelen die wij (vaak last-minute) nodig hadden. Ook Hilde en Paul horen in dit rijtje thuis, voor hun hulp met de detectie-systemen.

Bedankt ook aan alle vrienden en familie, te veel namen om op te sommen hier, voor de welkome ontspanning en afleiding buiten het werk.
Een speciale dank gaat naar mijn ouders om mij de kans te geven om verder te studeren en uiteindelijk dit doctoraat te behalen en aan mijn bompa om deze thesis mee na te lezen op taalfouten. En ten slotte is er nog Femke, bedankt voor de niet-aflatende steun, en de kleine en grote dingen van elke dag.

Lars

Preface

This thesis describes the results of an experimental study of β-delayed fission properties of ^{194,196}At and ^{200,202}Fr. The experiments were performed at the ISOLDE facility in CERN-Geneva (Switzerland).
Chapter 1 presents the research subject and a global motivation to study the nuclear fission process. Chapter 2 provides a short overview of the relevant nuclear decay modes, as well as current state-of-the-art experimental and theoretical (β-delayed) fission studies. Since the studied radioactive isotopes have a short lifetime, they have to be produced in a dedicated facility. The experiments presented in this work were performed at the ISOLDE facility in CERN, as described in chapter 3.

The data on the βDF of ^{200,202}Fr and ^{194,196}At were analyzed using the techniques described in chapter 4. The extracted βDF properties, including fission-fragment mass- and energy distributions, are discussed in a published paper

L. Ghys, A.N. Andreyev, M. Huyse, P. Van Duppen, S. Sels, B. Andel, S. Antalic, A. Barzakh, L. Capponi, T.E. Cocolios, X. Derkx, H. De Witte, J. Elseviers, D. V. Fedorov, V.N. Fedosseev, F.P. Hessberger, Z. Kalaninovà, U. Köster, J.F.W Lane, V. Liberati, K.M. Lynch, B.A. Marsh, S Mitsuoka, P Möller, Y Nagama, K. Nishio, S. Ota, D. Pauwels, R.D. Page, L. Popescu, D. Radulov, M.M. Rajabli, J. Randrup, E. Rapisarda, S. Rothe, K. Sandhu, M.D. Seliverstov, A.M. Sjödin, V.L. Truesdale, C. Van Beveren, P. Van den Bergh, Y. Wakabayashi "Evolution of fission-fragment mass distributions in the neutron-deficient lead region", *Physical Review C*, vol. 90, p. 041301(R), 2014.

This publication is fully incorporated in chapter 5. Chapter 6 describes a systematic study of β-delayed fission partial half-lives across the nuclear chart.

These results are published in

L. Ghys, A.N. Andreyev, S.Antalic, M. Huyse and P. Van Duppen, "Empirical description of β-delayed fission partial half-lives", *Physical Review C*, vol. 91, p. 044314, 2015.

The conclusions of this work as well as an outlook for future research are presented in chapter 7.

The setup used for the detection of the fission products consists of a pair of silicon detectors. In order to have a reliable energy calibration of these detectors for fission fragments, additional measurements were performed in ILL (Grenoble, France). The results of this experiment are summarized in appendix A and were employed to extract fission-fragment mass and energy spectra. This calibration procedure was also applied in the detailed analysis of the βDF of ^{180}Tl, which is presented in

J. Elseviers, A.N. Andreyev, M. Huyse, P. Van Duppen, S. Antalic, A. Antalic, A. Barzakh, N. Bree, T.E. Cocolios, V.F. Comas, J. Diriken, D. Fedorov, V.N. Fedosseev, S. Franchoo, **L. Ghys**, J.A. Heredia, O. Ivanov, U. Köster, B.A. Marsh, K. Nishio, R.D. Page, N. Patronis, M.D. Seliverstov, I. Tsekhanovich, P. Van den Bergh, J. Van De Walle, M. Venhart, S. Vermote, M. Veselsky and C. Wagemans. "β-delayed fission of ^{180}Tl", *Physical Review C*, vol. 88, p. 044321, 2013.

Abstract

Nuclear fission is the breakup of an atomic nucleus into two (sometimes three) fragments, thereby releasing a large amount of energy. Soon after its discovery in the late 1930's, the gross properties of the fission phenomenon were explained by macroscopic nuclear models. Certain features however, such as asymmetric fission-fragment mass distributions in the actinide region, require the inclusion of microscopic effects. This interplay of the microscopic motion of individual nucleons on this macroscopic process is, until today, not yet fully understood. The phenomenon of fission has therefore been of recurring interest for both theoretical and experimental studies.

This thesis work focusses on the β-delayed fission (βDF) process, an excellent tool to study low-energy fission of exotic nuclei, which was discovered in 1966 in the actinide region. In this two-step process, a precursor nucleus first undergoes β decay to an excited level in the daughter nucleus, which may subsequently fission.
Recently, an unexpected asymmetric division of ^{180}Hg nuclei was observed in a βDF study of ^{180}Tl. This work presents the experimental investigation of βDF properties of ^{194,196}At and ^{200,202}Fr nuclei, also situated in this scarcely studied region (with respect to the fission process) of the nuclear chart.

The experiments were performed at the ISOLDE facility in CERN (Geneva, Switzerland), where neutron-deficient francium (Fr) and astatine (At) isotopes are formed by bombarding a UC_x target with energetic protons. A purified radioactive ion beam is created by element-selective ionization and subsequent mass separation. For francium, the surface ionization mode was employed, while resonant laser-ionization was used to ionize astatine. The beam was then implanted on one of ten thin carbon foils, mounted on a rotatable wheel. β-delayed fission fragments were recorded by silicon detectors placed on either side of this foil. Fission-fragment masses were extracted from the energy spectra employing mass and momentum conservation laws. A dedicated experimental

campaign to calibrate the silicon detectors was performed at the Lohengrin spectrometer in ILL, where fission products from the neutron-induced fission of ^{235}U are separated based on their mass and energy. Other systematic effects, such as energy loss in the carbon foil or the emission of prompt neutrons, were also investigated. Other physics observables, which can be extracted from the βDF data, are the βDF probability or partial decay half-life.

For the studied isotopes ^{194,196}At and ^{200,202}Fr, βDF was observed and corresponding branching ratios could be extracted. Fission-fragment mass distributions of daughter products ^{194,196}Po and ^{202}Rn were measured for the first time and showed a triple-humped structure, marking the transition between asymmetric fission observed in ^{178,180}Hg and a more symmetric split of ^{204}Rn nuclei, observed in previous studies. A comparison with contemporary fission models, namely the macroscopic-microscopic finite-range liquid-drop model and the self-consistent approach employing the Gogny D1S energy density functional, yields discrepancies. These differences hint to the need for dynamical fission calculations, because for both models the potential-energy surfaces (PES) lack pronounced structures. This is in contrast to the actinide region, where deep valleys in the PES determine the most probable path from ground state to fission.

This work, together with other recent experimental campaigns at ISOLDE-CERN and SHIP-GSI (Darmstadt, Germany), has significantly extended the experimental βDF data in the neutron-deficient lead region. When combined with earlier experimental work in the uranium region, a systematic comparison of βDF-branching ratios became possible for a wide variety of isotopes across the nuclear chart.
From basic assumptions and simplified considerations, a simple exponential dependence of the βDF partial half-life on the difference between the Q value for β decay of the precursor and the fission-barrier height of the daughter is expected. This systematic trend, described with only two free parameters, was confirmed for experimental βDF partial half-lives spanning over seven orders of magnitude. Also for β-delayed fission probabilities, a similar dependence could be inferred and was verified using the available experimental data. These considerations could also be applied to other regions of the nuclear chart where βDF is expected to occur.

Beknopte samenvatting

Kernsplijting, ook wel fissie genoemd, is de splitsing van een atoomkern in twee (soms drie) stukken, waarbij een grote hoeveelheid energie vrijkomt. Niet lang na de ontdekking van dit fenomeen aan het einde van de jaren 1930, werden de algemene eigenschappen van fissie verklaard aan de hand van macroscopische modellen. Nochtans konden bepaalde observaties, zoals de asymmetrische massadistributies van fissiefragmenten in de regio van de actinides, enkel uitgelegd worden door het invoeren van microscopische correcties. Deze interactie van de microscopische beweging van individuele nucleonen met dit macroscopisch proces is tot op de dag van vandaag nog niet volledig begrepen. Hierdoor is fissie een fenomeen van blijvende interesse voor zowel theoretische als experimentele studies.

Dit werk concentreert zich voornamelijk op het proces van β-vertraagde fissie (βVF), een uitstekend hulpmiddel voor het bestuderen van laag-energetische fissie in exotische kernen, dat in 1966 werd ontdekt in de regio van de actinides. βVF is een proces in twee stappen, waarbij de moederkern eerst β-verval ondergaat naar een aangeslagen toestand in de dochter, die dan vervolgens kan splijten.
Een recente studie naar de β-vertraagde fissie (βVF) van ^{180}Tl heeft, onverwacht, aangetoond dat ^{180}Hg kernen asymmetrisch splitsen. Dit werk stelt het experimenteel onderzoek naar de eigenschappen van het βVF-proces in ^{194,196}At en ^{200,202}Fr kernen voor. Deze isotopen bevinden zich in een regio op de kernkaart die slechts sporadisch bestudeerd is op vlak van kernsplijting.

De experimenten werden uitgevoerd in de ISOLDE-faciliteit in CERN (Genève, Zwitserland), waar neutronarme francium (Fr) en astatine (At) kernen worden aangemaakt door het beschieten van een UC_x-trefschijf met hoog-energetische protonen. Uitgezuiverde radioactieve ionenbundels worden gevormd door het gebruik van element-selectieve ionizatietechnieken en vervolgens massaseparatie.

Voor francium is oppervlakte-ionisatie gebruikt, terwijl astatine geïoniseerd werd met behulp van resonante laserionisatie. Deze bundel wordt dan geïmplanteerd op een dunne koolstoffolie, waarvan er tien zijn bevestigd op een wiel. β-vertraagde fissieproducten worden waargenomen door siliciumdetectoren, geplaatst aan weerskanten van deze folie. De massa van de fissie-fragmenten werd afgeleid uit de energiespectra door het gebruik van de behoudswetten van massa en impuls. Er werd een gerichte meetcampagne gehouden aan de Lohengrin-spectrometer van het ILL, waar fissieproducten van de neutrongeïnduceerde fissie van ^{235}U worden gescheiden op basis van hun massa en energie, voor het kalibreren van de siliciumdetectoren. Ook andere systematische effecten, zoals het energieverlies in de koolstoffolie of de prompte emissie van neutronen, werden onderzocht. Andere fysische observabelen, die kunnen worden afgeleid uit de βVF data, zijn de waarschijnlijkheid of partiële halfwaardetijd voor βVF.

Het βVF-proces werd waargenomen voor de bestudeerde isotopen ^{194,196}At en ^{200,202}Fr en bijhorende vervalwaarschijnlijkheden konden bepaald worden. De massadistributies van de fissiefragmenten werden voor het eerst opgemeten voor de dochterkernen ^{194,196}Po en ^{202}Rn en vertoonden een structuur met drie pieken. Deze metingen duiden de overgang aan tussen asymmetrische fissie in ^{178,180}Hg en een meer symmetrische splijting van ^{204}Rn kernen, waargenomen in vroegere metingen. Er werden ook sterke verschillen waargenomen met voorspellingen van twee fissiemodellen. Het eerste model is een macroscopisch-microscopische beschrijving van de kern als een vloeibare druppel met eindige afmetingen, terwijl het tweede model een zelf-consistente aanpak is waarbij de Gogny D1S energiedichtheidsfunctionaal is gebruikt. Deze verschillen wijzen erop dat een dynamische berekening van fissie nodig is. De potentiaaloppervlakken van beide modellen hebben immers geen uitgesproken structuren, in tegenstelling tot de regio van de actinides, waar diepe valleien in de potentiaaloppervlakken het meest waarschijnlijke pad aanduiden tussen grondtoestand en fissie.

De gegevens bekomen in dit werk werden gecombineerd met data van recent experimenteel onderzoek in ISOLDE-CERN en SHIP-GSI (Darmstadt, Duitsland) en eerder werk in de regio rond uranium. Hierdoor werd een systematische studie van de βVF vertakkingsverhouding mogelijk voor een uitgebreide waaier van atoomkernen.
Enkele basisaannamen en vereenvoudigde beschouwingen duiden op een simpele exponentiële afhankelijkheid van de partiële levensduur voor βVF ten opzichte van het verschil van de Q-waarde voor β-verval met de hoogte van de fissiebarrière. Deze trend, beschreven met slechts twee vrije parameters, is bevestigd voor experimentele partiële levensduren die meer dan zeven grootte-ordes overspannen. Ook voor βVF-waarschijnlijkheden kon een dergelijke

afhankelijkheid worden afgeleid en aangetoond aan de hand van de beschikbare experimentele data. Deze beschouwingen kunnen ook worden toegepast op andere regio's van de kernkaart waar βVF kan voorkomen.

List of abbreviations and symbols

At Astatine

$\boldsymbol{B}_{\mathrm{f}}$ Fission-barrier energy

$\boldsymbol{\beta}$**DF** β-delayed fission

CERN Conseil Européen pour la Recherche Nucléaire

EC Electron Capture

EM ElectroMagnetically

ETFSI Extended Thomas-Fermi plus Strutinsky Integral

FF Fission Fragment

Fr Francium

FRDM Finite-Range Droplet-Model

FRLDM Finite-Range Liquid-Drop Model

FWHM Full Width at Half Maximum

Ge Germanium

GPS General Purpose Separator

GSI Gesellschaft für SchwerIonenforschung

HRS High Resolution Separator

ILL Institut Laue-Langevin

ISOLDE Isotope Separator On Line DEvice

LDM Liquid Drop Model

MD Mass Distribution

$\boldsymbol{P_{\beta \mathrm{DF}}}$ β-delayed fission probability

PES Potential-Energy Surface

PHD Pulse Height Defect

PIPS Passivated Implanted Planar Silicon

PP Proton Pulse

PSB Proton Synchrotron Booster

Po Polonium

$\boldsymbol{Q_\beta}$ Q value for β decay

RMSD Root-Mean-Square Deviation

Rn Radon

RILIS Resonance Ionization Laser Ion Source

SC Super Cycle

SHIP Separator for Heavy Ion reaction Products

Si Silicon

SSB Silicon Surface Barrier

$\boldsymbol{T_{1/2\mathrm{p},\beta \mathrm{DF}}}$ β-delayed fission partial half-life

TF Thomas Fermi

TKE Total Kinetic Energy

Tl Thallium

U Uranium

WM 'Windmill' detection setup

Contents

Chapter 1

Introduction and motivation

The Greek philosopher Democritos postulated, already in 400 B.C., that each kind of material consists of indivisible particles, so called 'atoms'. Their existence was indeed verified by scientific experiments in the early 19th century. However, later research showed that a neutral atom, having a size of about $\sim 10^{-10}$ m, consists of Z electrons orbiting a core of A nucleons with N neutral neutrons and Z positively charged protons. Most of the atomic mass is concentrated in this nucleus, although its radius is in the order of only 10^{-15} m. The nucleus is bound by the attractive strong force between nucleons, which opposes the electric repulsion between the charged protons. Nuclei with an unfavorable neutron to proton ratio can transform into nuclei with a higher average binding energy per nucleon. For example, one of the neutrons can be converted into a proton, or vice-versa, by a process called β decay. Alternatively, one or several particles, such as an α particle, can be emitted from the core. In fact, only 254 isotopes, out of the more than 3300 isotopes known today [1], are stable against such nuclear transformations.

In the late 1930's, Hahn and Strassmann discovered that uranium nuclei may split into two smaller fragments of roughly the same size when bombarded with neutrons [2] . This dramatic form of nuclear disintegration, called fission, was then quickly employed in various applications, such as weaponry and electricity production. From a fundamental point of view, the complex interplay between the microscopic effects of individual nucleons on this macroscopic many-body decay mode is not yet fully understood. The fission phenomenon therefore continues to be of interest for both experimental and theoretical nuclear-physics studies. One important observable in such studies is the fission-

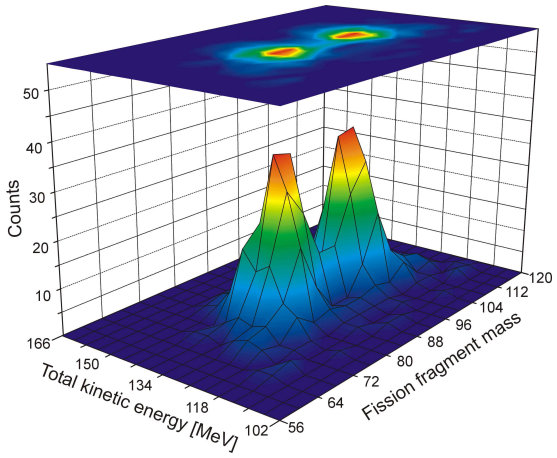

Figure 1.1: (In color) Mass and TKE distribution of FFs resulting from the fission of ^{180}Hg. An asymmetric mass distribution was observed with the most probable FFs situated around mass numbers 80 and 100. Figure taken from [3]

fragment mass distribution, which shows whether fission proceeds symmetrically or asymmetrically. In the first case, both fragments have the same mass, while one of the fragments is significantly heavier than the other in the latter case. Recent fission studies have found a new type of asymmetric fission in ^{178,180}Hg nuclei, unanticipated by contemporary fission models [3, 4]. Figure 1.1 shows the observed asymmetric mass distribution in the fission of ^{180}Hg at low excitation energies, with the most probable fission-fragment mass numbers equal to 80 and 100. These results triggered a renewed experimental and theoretical interest to learn about low-energy fission in the neutron-deficient lead region. This thesis work, in particular, discusses the fission properties of ^{194,196}Po and ^{200,202}Rn, which were experimentally investigated at the ISOLDE-CERN facility in Geneva (Switzerland) by means of β-delayed fission. In this two-step decay process, fission is preceded by β decay. This study allows to map for the first time the transition region between asymmetric fission of ^{178,180}Hg nuclei, and a symmetric division observed in ^{204}Rn nuclei [5, 6]. In addition, these data revealed several discrepancies with predictions from contemporary fission models.

Next to the interest in the fission phenomenon as such, an accurate description of the fission process for nuclei far from stability is needed, for example, to model the astrophysical r-process in explosive stellar environments, responsible for the formation of the heaviest element in the universe. During this process, the rapid capture of neutrons by lighter nuclei and the subsequent β^- decay

produces increasingly heavier nuclei. However, the probability for spontaneous, β-delayed or neutron-induced fission also rises for higher mass numbers. Fission is thus expected to terminate the r-process in the super-heavy region ($A \gtrsim 280$), while neutrons can again be captured by the fission fragments. This so-called fission recycling process has an influence on the resulting elemental distribution and is mainly determined by the fission-fragment masses and fission probabilities [7–9]. However, these super-heavy neutron-rich elements are inaccessible to present-day experimental techniques, and their decay and fission properties are thus inferred from theoretical models. As illustrated in Figure 1.2, predicted fission probabilities may strongly depend on the model. Therefore, (β-delayed) fission data from exotic nuclei, for example from the neutron-deficient lead region, are vital to benchmark contemporary models.

In chapter 2, an overview of fission and other relevant nuclear decay modes is given. Also, a description of β-delayed and other experimental fission studies is provided, as well as a general summary of observed fission-fragment mass distributions across the nuclear chart. In addition, contemporary theoretical approaches to the fission process are discussed.
The production of purified radioactive ion beams at ISOLDE-CERN is discussed in chapter 3, together with the setup for the detection of fission fragments and other types of radioactive decay.
In chapter 4, the purity of the ISOLDE beams in the different experimental campaigns is investigated. Furthermore, β-delayed fission probabilities and partial half-lives are extracted from the data. The calibration techniques for a precise determination of fission-fragment kinetic energies and masses are also provided.
Chapter 5 then shows the observed fission-fragment mass and total-kinetic energy distributions, which mark the transition region between asymmetric fission in ^{178,180}Hg and symmetry in ^{204}Rn. These results are compared with current fission models.
A systematic trend for the measured partial β-delayed fission half-lives throughout the nuclear chart is demonstrated in chapter 6, thereby including data from this work. Interestingly, this trend was found to arise naturally from simple theoretical considerations.
Finally, chapter 7 provides a conclusion of the present work and an outlook for possible new experimental campaigns on β-delayed and other low-energy fission studies.

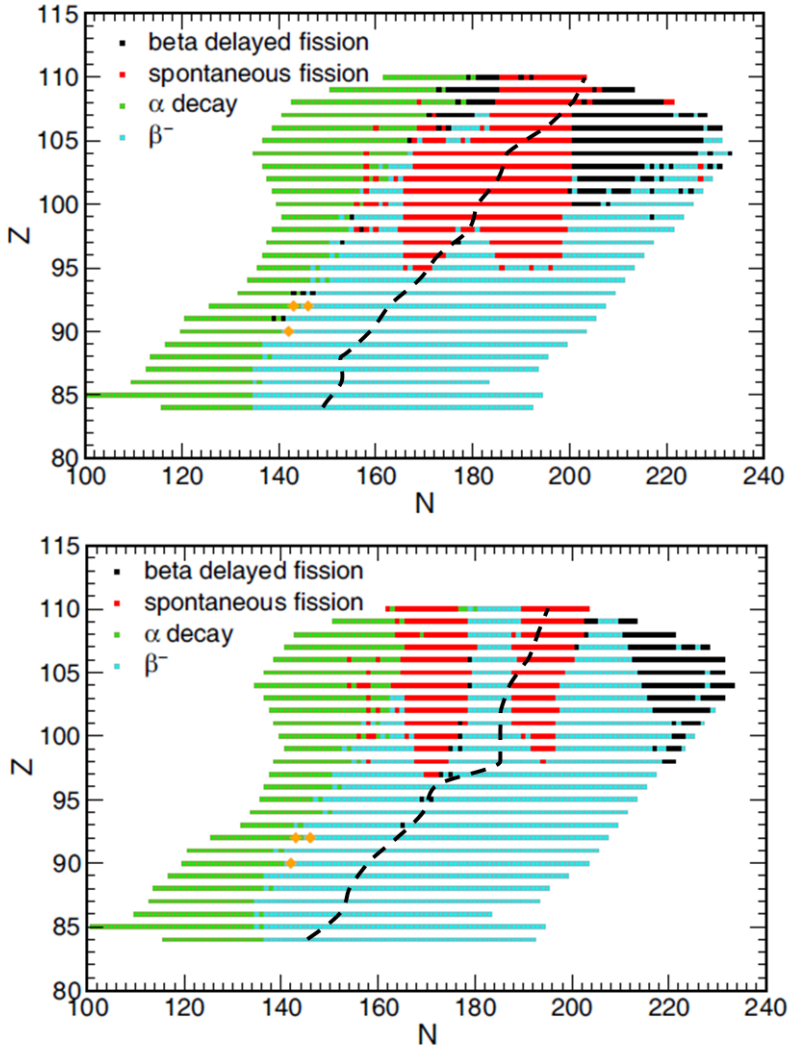

Figure 1.2: (In color) Dominant decay channels for nuclei with $Z \geq 84$ using different theoretical models for both nuclear masses and fission-barrier energies. In the top figure, a combination of the Thomas-Fermi(TF) [10] and Finite-Range Droplet-model (FRDM) [11] are used for the respective calculation of barriers and masses. For the bottom figure, the extended Thomas-Fermi plus Strutinsky Integral (ETFSI) approach [12, 13] was employed. The yellow diamonds indicate the naturally occurring nuclei ^{232}Th and ^{235,238}U. Nuclei to the right of the black dashed line have a Q value for β-decay exceeding the neutron-separation by at least 3 MeV, according to the corresponding mass model FRDM (top) or ETFSI (bottom) (see section 6.3 for more details). Figure taken from [8].

Chapter 2

Fission and other nuclear decay modes

Since its discovery in 1938 [2, 14], the fission process was studied through a wide variety of experimental techniques. In addition, several theoretical frameworks were developed to account for the experimental observations. This chapter aims at providing a summary of the past experimental and theoretical fission studies as well as other basic nuclear-physics concepts which are relevant to this work. The first section reviews relevant nuclear decay modes, including α, β, γ and fission decay. Section 2.2 provides an overview of experimental low-energy fission studies, thereby emphasizing β-delayed fission, the subject of this thesis work. A brief summary of observed fission properties across the nuclear chart, mainly including mass- and total kinetic energy distributions, is given in section 2.3. Finally, some contemporary fission models are described in section 2.4.

2.1 Nuclear decay modes

2.1.1 α,β and γ decay

A neutron in a nucleus can be converted into a proton, or vice-versa, via the weak interaction. In β^- decay, one of the neutrons is converted into a proton by emitting an electron and anti- neutrino $\bar{\nu}$. Similarly, one of the protons can be transformed into a neutron by β^+ decay, thereby emitting a positron and neutrino ν, or through the competing electron-capture (EC) decay, whereby an

atomic electron from one of the inner orbitals is consumed in the process and a neutrino is emitted. These three processes, commonly denoted as β decay, are thus summarized as

$$\begin{array}{lcll} {}^{A}_{Z}X_N & \rightarrow & {}^{A}_{Z+1}Y_{N-1} + e^- + \bar{\nu} & (\beta^- \text{ decay}), \\ {}^{A}_{Z}X_N & \rightarrow & {}^{A}_{Z-1}Y_{N+1} + e^+ + \nu & (\beta^+ \text{ decay}), \\ {}^{A}_{Z}X_N + e^- & \rightarrow & {}^{A}_{Z-1}Y_{N+1} + \nu & (\text{EC decay}). \end{array} \tag{2.1}$$

The energy released in a nuclear decay is defined by the Q-value and is calculated as the energy difference between the initial and final state. In the case of β decay, Q_β values are calculated by [15]

$$\begin{array}{lcll} Q_{\beta^-} & = & [m({}^{A}_{Z}X_N) - m({}^{A}_{Z+1}Y_{N-1})]c^2 & (\beta^- \text{ decay}), \\ Q_{\beta^+} & = & [m({}^{A}_{Z}X_N) - m({}^{A}_{Z-1}Y_{N+1}) - 2m_e]c^2 & (\beta^+ \text{ decay}), \\ Q_{EC} & = & [m({}^{A}_{Z}X_N) - m({}^{A}_{Z-1}Y_{N+1})]c^2 - B_n & (\text{EC decay}), \end{array} \tag{2.2}$$

with m representing neutral atomic masses, m_e the mass of an electron and B_n the binding energy of the captured electron from the shell with principal quantum number n. The transition rate λ_β (s^{-1}) can be expressed as [16]

$$\lambda_\beta = \sum_n \int_0^{Q_\beta} S^n_\beta(E) F_n(Z, Q_\beta - E) dE, \tag{2.3}$$

whereby $F_n(Z, Q_\beta - E)$ and $S^n_\beta(E)$ are the respective Fermi-integral function and beta-strength function of the n-th forbidden β transition to an excited level with energy E. For a β transition with $n = 0$, denoted as allowed decays, the spin change Δ I between initial and final state is 0 or 1 and there is no change in parity : $\Delta\pi = 1$. In general for n-forbidden decays, one has the relation [17]

$$\Delta I \leq n + 1 \qquad \Delta\pi = -1^n. \tag{2.4}$$

If n increases by one unit, the corresponding β-decay transition rate decreases by roughly four orders of magnitude [15]. Allowed decays are thus strongly favored and, for most nuclei, λ_β can in first order be approximated by only considering the term with $n = 0$ in equation 2.3. If the index n is dropped, equation 2.3 reduces to

$$\lambda_\beta = \int_0^{Q_\beta} S_\beta(E) F(Z, Q_\beta - E) dE. \tag{2.5}$$

The Fermi function $F(Z, Q_\beta - E)$ is a phase-space integral and can be approximately written for allowed decays as [17]

$$F(Z, Q_\beta - E) \simeq g(Z)(Q_\beta - E)^a, \tag{2.6}$$

whereby $a \simeq 2$ for EC and $a \simeq 5$ for $\beta^{+,-}$ decay [18, 19] and $g(Z)$ incorporates the dependence of F on Z. The β-strength function S_β mainly depends on the overlap of the initial and final-state nuclear wave functions and the energy-level densities and may exhibit sharp resonances [20]. The form of S_β is for many (exotic) nuclei experimentally undetermined and must be estimated. Therefore, as shown in, for example, [21], the shape of S_β as a function of E is strongly model dependent.

Another decay mode involves the emission of one or several nucleons, which may be in the form of an α particle. This two-body process can be written as

$${}^{A}_{Z}X_N \rightarrow {}^{A-4}_{Z-2}Y_{N-2} + \alpha, \tag{2.7}$$

In the neutron-deficient lead region, this disintegration process is often the dominant decay mode. Therefore, parasitic α-decay data were obtained during the investigation of the β-delayed fission properties in this region.

After, for example, α or β decay, the nucleus might be left in an excited state. The subsequent de-excitation can happen through the emission of energetic photons, denominated as γ rays. The surplus of energy can also be carried by atomic electrons from the inner orbitals in a process known as internal conversion. Another possibility of deexcitation is through fission.

Due to the uncertainty principle in quantum mechanics, the energy of any state with a mean lifetime τ has a certain width $\Gamma = \hbar/\tau$. Considering different decay possibilities (here indicated by i), the total width of a nuclear state is determined by the sum of the different partial decay widths Γ_i. For example, the partial width for γ decay of a certain state is denoted here by Γ_γ.

2.1.2 Fission

The most dramatic form of nuclear disintegration is fission, whereby a nucleus splits into two or more parts of about the same mass, thereby releasing a large

amount of energy. Normally, fission is a binary process, whereby only two primary fragments are formed. Much less frequently, a nucleus can split into three fragments, called ternary fission (see for example [22]). Fission can either happen spontaneously or after excitation of the fissionable isotope.
The first theoretical explanation of this process, whereby the nucleus is represented as a liquid drop, was already provided shortly after the experimental discovery of the fission process [23]. Despite several shortcoming of this macroscopic model (see also section 2.4.1), a reasonable qualitative and quantitative description of fission is given. Although the original model only considers binary fission, also ternary fission can be interpreted within the framework of a liquid-drop model [24, 25]. However, since the latter process occurs rarely, only binary fission will be considered here.

In the liquid-drop model, the nucleus in its ground state is represented by a spherical charged liquid drop of radius R_0. The energy needed to deform such a drop, $E_{\rm def}$, whereby the deformation is defined by the parameter ϵ, then equals [22]

$$E_{\rm def}(\epsilon) = E_s(\epsilon) + E_c(\epsilon) - E_s(0) - E_c(0). \tag{2.8}$$

E_s represents the surface energy and is proportional to the surface area of the drop, while the Coulomb energy is represented by E_c. In general, the deformation of a nucleus is described by

$$R(\theta,\phi) = R_0[1 + \sum_{\lambda,\mu} a_{\lambda\mu} Y_{\lambda\mu}(\theta,\phi)] \tag{2.9}$$

and the parameter ϵ can be described through some combination of $a_{\lambda\mu}$. For small distortions, only a pure quadrupole deformation is considered ($\epsilon = a_{20}$), and one may write

$$\begin{array}{rcl} E_s(\epsilon) & = & E_s(0)(1 + 2/5a_{20}^2), \\ E_c(\epsilon) & = & E_c(0)(1 - 1/5a_{20}^2) \end{array} \tag{2.10}$$

A spherical drop will thus only be stable against small deformations if $E_c(0) < 2E_s(0)$. This has led Bohr and Wheeler [23] to define the fissility parameter x as

$$x = E_c(0)/2E_s(0) \tag{2.11}$$

Since E_s is assumed to be proportional to R_0^2 and E_c to Z^2/R_0, the fissility parameter goes like Z^2/A. For most nuclei in the actinide region, the fissility parameter x is situated at values around 0.7.
Another important parameter in equation 2.9 is a_{40}, describing hexadecupole deformation, responsible for the formation of the nascent fission fragments. Possible mass asymmetry between both fragments is accounted for by the octupole deformation paramater a_{30}.

Figure 2.1 shows the deformation energy of a typical actinide nucleus ($x \simeq 0.7$) with respect to the quadrupole and hexadecupole deformation parameters. The energetically most favorable path to fission is indicated by the dashed line.
These energy contours shows a saddle point at higher deformation energies. The potential barrier for fission, denoted by the fission-barrier energy B_f, is defined as the energy difference between this saddle point and the nuclear ground state. Numerical liquid-drop calculations including multipoles up to $\lambda \approx 16$ have shown that one can approximate B_f by [26]

$$B_\mathrm{f} \approx 0.83 E_s(0)(1-x)^3. \tag{2.12}$$

At the saddle point, the fission fragments are in most cases not yet fully separated. The rupture of the neck connecting the nascent fragments, also denoted by scission, takes place on the descending part of the potential-energy curve along the fission path, shown in Figure 2.1 b.

Due to the possible exchange of nucleons between the nascent fragments before the rupture of the neck, a variety of final fission products can be formed. In contrast to the resulting products of α decay, fission fragments (FFs) will thus exhibit a certain statistical spread in mass, neutron and proton number.
The liquid-drop model predicts a most probable split of the nucleus into fragments with nearly identical masses, resulting in a single-humped or symmetric mass distribution (MD). However, for most actinides, one of the fragments is considerably heavier than the other and a double-humped asymmetric MD is observed (see also section 2.3).
This asymmetry can be explained by microscopic effects in both the fissioning system and the resulting fragments. In analogy with electrons in atomic theory, nucleons are believed to move in well-defined orbitals [27]. The existence of these shells are evidenced by sharp discontinuities in gross nuclear properties, such as nucleon separation energies. These jumps occur at specific, so-called 'magic', nucleon numbers. As discussed in sections 2.3 and 2.4, these microscopic shell effects play an important role in the macroscopic fission process.

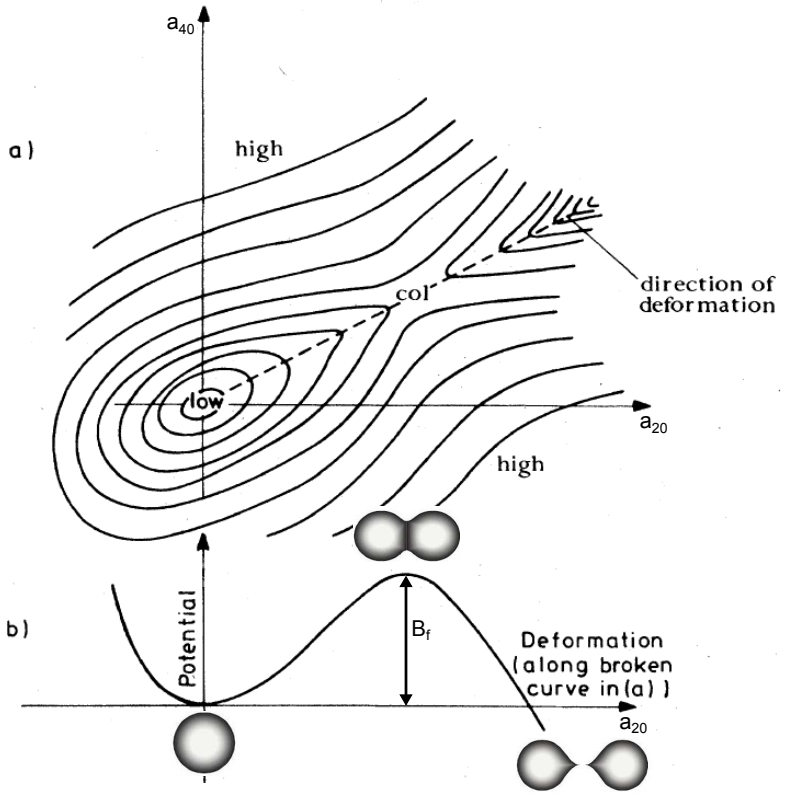

Figure 2.1: a) A sketch of potential-energy contours of a fissionable nucleus as a function of the quadrupole and hexadecapole deformation parameters. The minimum energy trajectory for fission is indicated by the dashed line and the saddle point by 'col'. The potential energy along this trajectory is shown in b), along with a schematic representation of the corresponding nuclear shapes. Figure adapted from [26]

After scission, the FFs are repelled by the Coulomb interaction. The total kinetic energy (TKE) of fragments with masses A_1 and A_2 and corresponding atomic numbers Z_1 and Z_2 can be estimated by the potential energy of two touching spheres

$$\mathrm{TKE} = \frac{Z_1 Z_2 e^2}{r_0(A_1^{1/3} + A_2^{1/3})}, \tag{2.13}$$

with $r_0 \simeq 1.17$ fm [28]. When considering typical fragments in the fission of ^{236}U, namely $^{94}_{38}$Sr and $^{142}_{54}$Xe a TKE of 259 MeV is obtained. This value is significantly higher than the average TKE value of 170 MeV, measured for the neutron-induced fission of ^{236}U [29]. Since in reality the fragments at scission are believed to adopt an elongated form, the distance between the charge centers is increased as compared to a spherical shape, which according to equation 2.13 results in a lower TKE. The TKE value can thus serve as a measure for the deformation of FFs at the neck rupture [30].
Next to the TKE of the fission fragments, the energy released in the fission process can be carried by neutrons or γ rays, emitted promptly after scission. In the case of neutron-induced fission of ^{235}U, on average 2.5 prompt neutrons per fission event are emitted [22]. In literature, often pre-neutron emission quantities are given, corresponding to properties of fission fragments before the evaporation of prompt neutrons.

Similar to the γ-decay width Γ_γ, the partial decay width for fission of a certain state with excitation energy E is represented by Γ_f. When the value of E is around or below B_f, fission can essentially be described as a tunneling process through a potential barrier. The partial half-life for spontaneous fission from the ground state ($E = 0$) thus strongly increases for higher values of B_f. Most of the nuclei for which ground-state spontaneous fission is detectable, have B_f values typically lower than 6 MeV [22]. Therefore, an excitation mechanism of the fissioning nucleus is often required before an appreciable fission rate can be observed. The fission process is broadly classified as high-energy fission, when the excitation energy vastly exceeds B_f, or low-energy fission, when the excitation energy is at most a few MeV above B_f.
An example of the former case are fusion-fission reactions, whereby the fusion of two lighter nuclei is followed by the fission of the compound nucleus. Such reactions allow to probe fission properties of exotic nuclei, including neutron-deficient isotopes in the lead region [31]. For example, recent fusion-fission studies show indications that the asymmetric fission in the region around ^{180}Hg may persist at excitation energies more than 20 MeV above B_f[32, 33]. Nonetheless, microscopic effects are often washed out at higher excitation

energies (see also Figure 2.2).
Low-energy fission on the other hand provides an excellent tool to probe the interplay between microscopic and macroscopic effects. This work focusses on β-delayed fission (βDF), whereby fission occurs at excitation energies below or near the fission barrier. The next section provides a detailed discussion on the experimental investigation of this process, as well as a short summary of some other experimental techniques to study low-energy fission.

2.2 Experimental techniques to study low-energy fission

2.2.1 Spontaneous and particle-induced fission

As mentioned before, fission can occur spontaneously at a detectable rate, provided that B_f is sufficiently low. The first experimental evidence for ground-state spontaneous fission was found for uranium nuclei by Petrzhak and Flerov in 1940 [34]. Since then, this process has been observed in a few tens of nuclei with partial spontaneous fission half-lives ranging from 380 μs to 10^{18} years [22]. In addition, spontaneous fission may also proceed from an isomeric level, denoted by fission isomers. The partial half-lives for this fission decay mode are many orders of magnitude shorter than those of the corresponding ground-state spontaneous fission.

Low-energy fission can be induced by the bombardment of a heavy nucleus with light particles such as neutrons, protons or alpha particles. In fact, fission was first observed after neutron-capture by uranium nuclei. By varying the energy of the incident particles, mass distributions, as well as fission probabilities can be studied as a function of excitation energy of the fissile nucleus [35]. For example, Figure 2.2 shows a gradual transition from asymmetric to symmetric MDs after the proton-induced fission of ^{232}Th, when the beam energy is increased. Such experiments demonstrate a decrease of the influence of shell effects on the fission process at higher excitation energies. In addition, particle-induced fission allowed to probe fission properties in the pre-actinide region (see e.g. [36–38]). However, since these experiments require stable, or long-lived, target nuclei, such studies can only be performed for nuclei close to stability. Recently however, a novel method was developed to measure fission yields after nucleon-transfer reactions in inverse kinematics, which allows to access short-lived fissionable nuclei [39].

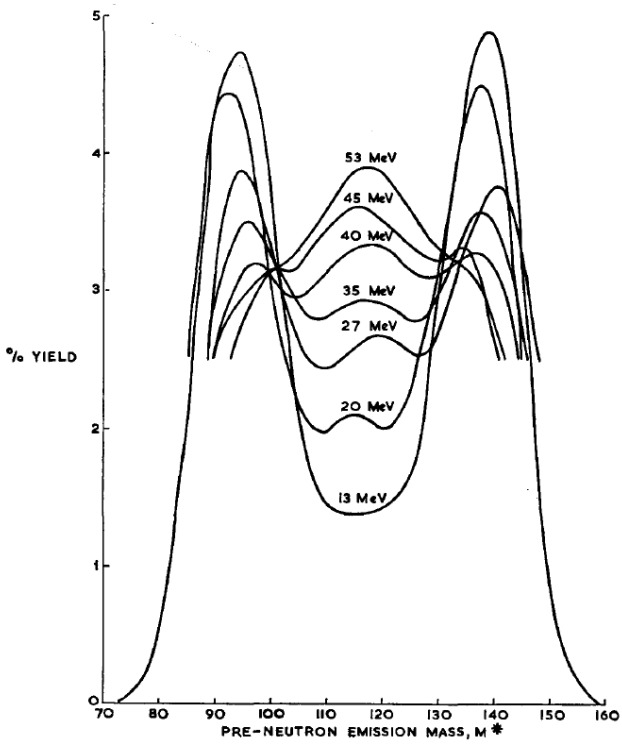

Figure 2.2: Pre-neutron emission FF mass distributions, recorded after the bombardment of a ^{232}Th target with protons. The beam energies are given as labels to the curves. Figure taken from [35].

2.2.2 Electromagnetically induced fission

Due to the limitations of both spontaneous and particle-induced fission experiments, indicated in the previous section, fission could only be studied in a limited amount of isotopes by these techniques. In 1999, the introduction of electromagnetically (EM) induced fission at the GSI fragment separator in Darmstadt, allowed to investigate for the first time fission in a wide variety of (short-lived) nuclei [5, 6]. Secondary beams, created from the spallation of a ^{238}U primary beam, are first mass separated and identified in the GSI fragment separator. After impinging on a secondary target consisting of lead foils, excitation through the giant dipole resonance may induce fission. Since the lead foils also act as electrodes of a subdivided ionization chamber, the place at which fission occurs can be determined. Subsequent detection of FFs

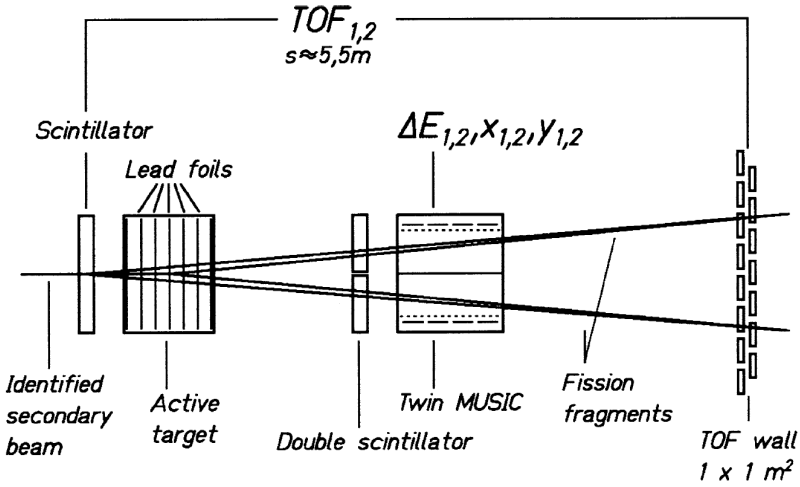

Figure 2.3: Schematic drawing of the setup used for the detection of EM-induced fission fragments from an identified secondary beam from the GSI fragment separator. Figure taken from [5]

by a large ionization chamber and a time-of-flight array allows to assign their kinetic energies and atomic numbers Z. The setup is schematically depicted in Figure 2.3. Inclusion of a large-acceptance dipole magnet in this setup has recently allowed to measure simultaneously Z,A as well as the kinetic energy of both fission fragments [40].

The excitation-energy function of the fissioning nucleus is a relatively broad distribution with a mean around 12 MeV, which is in most investigated cases a few MeV above B_f [41].

2.2.3 β-delayed fission

β-delayed fission provides an alternative and unique way to study low-energy fission in short-lived nuclei. In this two-step process, the fissioning daughter is created by β decay of a precursor nucleus and left in an excited state. If the excitation energy E^* is near or above B_f, decay through fission may be favored over other de-excitation modes, such as γ or particle emission. Note that E^* is limited by the Q value for β decay Q_β. In addition, β decay favors population of excited levels in the daughter with similar spin and parity as the

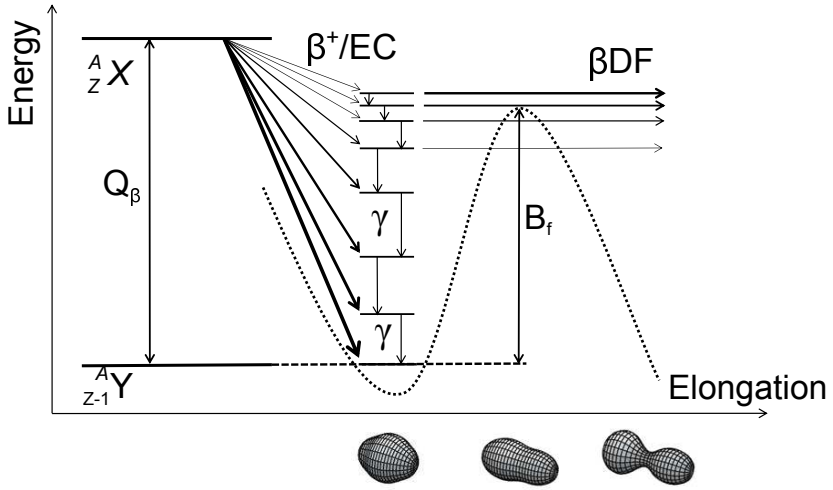

Figure 2.4: Schematic representation of βDF on the neutron-deficient side of the nuclear chart. The curved dotted line indicates the potential energy of the daughter nucleus with respect to nuclear elongation, displaying also the fission barrier.

parent, thereby constraining possible spins and parities of the fissioning states. Due to the form of the Fermi function (see section 2.1.1), the probability for β decay decreases to levels with increasing excitation energy. On the other hand, the probability for fission decay is expected to rise for higher excitation energies of the fissioning nucleus. The combination of the opposing trends of these processes make that βDF is most likely to occur a few MeV below Q_β, see also chapter 6. A schematic representation of this process is shown in figure 2.4. Several reviews have been published on this subject [18, 19], of which the most recent one includes the recent experimental progress on βDF in the neutron-deficient lead region [42].

For a sizeable, and thus detectable, βDF channel to occur, two main conditions must be fulfilled. First, the precursor should have an appreciable β-decay branching ratio b_β, typically higher than 1%. Second, the Q_β value of the parent must be comparable or higher than the fission-barrier energy B_f of the daughter ($Q_\beta - B_\mathrm{f} \gtrsim -3\,\mathrm{MeV}$). Figure 2.5 shows the nuclei fulfilling these conditions, revealing that βDF is only accessible in two regions of the nuclear chart by present-day experimental techniques. In total, 26 βDF cases have been identified, for which the fission-fragment distributions of 11 daughter nuclei were measured. The first experimental evidence for βDF was found in ^{232,234}Am and

^{228}Np [43, 44], situated in the region around uranium. As depicted in Figure 2.6, this region was also studied by spontaneous and neutron-induced fission [22].
Another zone of βDF candidates, far less investigated regarding the fission process, is situated in the neutron-deficient lead region. In addition, these nuclei have an N/Z ratio of $\sim 1.2 - 1.3$, significantly different from the precursors around uranium ($\sim 1.4 - 1.5$). This fact allows to investigate possible isospin dependencies of certain βDF properties, such as branching ratios (see also chapter 6). Evidence for βDF in this region was first observed at the Flerov Laboratory in Dubna, Russia, by studying the β decay of ^{180}Tl, produced by the reaction of a ^{40}Ca beam on an enriched ^{144}Sm target [45]. However, FF mass distributions remained undetermined. The βDF of ^{188}Bi and ^{196}At was recorded in a similar experiment [46]. Later measurements at the ISOLDE facility in CERN (Geneva, Switzerland) [3, 47] showed that the previously estimated βDF branching ratio of ^{180}Tl was underestimated by about two orders of magnitude. Also, FF mass distributions could be determined and showed an unexpected asymmetry [3], see also section 2.3. This observation has led to renewed experimental efforts to measure βDF properties in the neutron-deficient lead region. Experiments at SHIP-GSI (Darmstadt, Germany) allowed to determine the branching ratios and total kinetic energies (TKE) of the FFs for the βDF of the isotopes ^{186,188}Bi [48] and ^{192,194}At [49]. Also, one single βDF event of ^{200}Fr was observed in [50]. This PhD work discusses several experiments at ISOLDE-CERN to measure the βDF properties of ^{194,196}At and ^{200,202}Fr, allowing for the first time to extract reliable TKE and branching ratios, as well as the FF mass distributions of their corresponding β-decay daughters.

As discussed in the previous chapter, it is believed that βDF, together with neutron-induced, spontaneous and photo-fission, plays a significant role in the fission recycling of the r-process nucleosynthesis (see for example [7–9]). Therefore, reliable predictions for βDF branching ratios are needed for the heavy neutron-rich nuclei, which are important for the r-process but experimentally unaccessible at present. Measured βDF probabilities $P_{\beta\mathrm{DF}}$, defined as the relative amount of βDF events $N_{\beta\mathrm{DF}}$ to the number of β decays N_β, can help in benchmarking theoretical fission models. This quantity can thus be written as

$$P_{\beta\mathrm{DF}} = \frac{N_{\beta\mathrm{DF}}}{N_\beta}. \tag{2.14}$$

However, most of the precursors in the neutron-deficient lead region exhibit a high α branching ratio ($b_\alpha > 90\%$), making the determination of N_β difficult

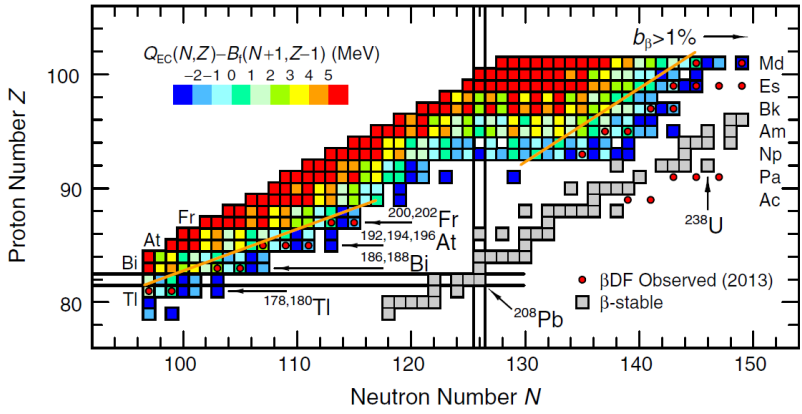

Figure 2.5: (In color) The color code denotes $(Q_\beta - B_\mathrm{f})$ differences for part of the nuclidic chart, calculated within the framework of the FRDM-FRLDM framework. Values below -3 MeV are not plotted, while red color indicates values exceeding 5 MeV. Isotopes to the right-hand side of the orange sloped lines have approximately $b_\beta > 1\%$. Nuclides for which βDF is observed, are marked by the full red circles. The figure was taken from [42].

(see also section 4.3). Therefore the βDF partial half-life $T_{1/2\mathrm{p},\beta\mathrm{DF}}$, by analogy with other decay modes, was introduced in [42] as

$$T_{1/2\mathrm{p},\beta\mathrm{DF}} = T_{1/2}\frac{N_\mathrm{dec,tot}}{N_{\beta\mathrm{DF}}}. \tag{2.15}$$

Here, the total half-life is denoted by $T_{1/2}$ and the total number of nuclear decays by $N_\mathrm{dec,tot}$. When α decay is dominant, $N_\mathrm{dec,tot}$ can be safely approximated by the number of α decays N_α, a quantity which can be accurately determined with the detection set up used in this work. Systematic errors related to detector efficiencies are eliminated, since both FF and α particles are recorded using the same detector. A relation between $T_{1/2\mathrm{p},\beta\mathrm{DF}}$ and $P_{\beta\mathrm{DF}}$ is found by combining 2.14 and 2.15:

$$T_{1/2\mathrm{p},\beta\mathrm{DF}} = \frac{T_{1/2}}{b_\beta P_{\beta\mathrm{DF}}}, \tag{2.16}$$

whereby b_β denotes the β-branching ratio of the precursor. A systematic comparison of $T_{1/2\mathrm{p},\beta\mathrm{DF}}$ values throughout the nuclear chart is presented in chapter 6, where an exponential dependence of $T_{1/2\mathrm{p},\beta\mathrm{DF}}$ with respect to $(Q_\beta -$

B_f) is observed. In addition, this dependence was inferred from simple theoretical considerations.

2.3 Observations in fission-fragment mass distributions

Figure 2.6 provides an overview of low-energy fission studies throughout the nuclear chart, including MD's of a few key isotopes. It is apparent that the region beyond thorium up to about Fermium is well-studied with a variety of methods. Apart from some notable exceptions, asymmetric fission dominates for most cases in this region. The doubly-magic nature of the nucleus ^{132}Sn is believed to strongly influence the formation of the heavier FF in this asymmetric split. Figure 2.7 shows indeed that the mean mass of the heavier FFs is situated around 140 amu, independent of the mass of the fissioning system.
Isotopes such as ^{258}Fm and ^{259,260}Md exhibit complex MD's with both a broad and a narrow symmetric component [51, 52]. The TKE of the FFs was furthermore observed to be higher for the latter component. Hulet and co-workers interpreted these observations as a superposition of two different fission modes, referred to as *bimodal fission*. These modes correspond to different fission paths on a multi-dimensional potential-energy surface, describing the potential energy of the fissioning nucleus with respect to deformation (see also section 2.4.1). The fission path responsible for the narrow part in the MD is ascribed to shell effects around ^{132}Sn. Due to these microscopic effects, the resulting FFs after scission have a rather compact shape, causing a relatively strong Coulomb repulsion and thus high TKE. In contrast, the broader component is believed to arise from liquid-drop like fission with an elongated shape at scission (thus, lower TKE) and broader MD's.
In the region around ^{226}Th, a competition between symmetric and asymmetric fission results in a triple-humped MD [6, 53–55]. In addition, the TKE of the asymmetric component was observed to be higher than that of the symmetric part. These observations again support the assumption that a nucleus can fission through several independent modes, corresponding to different prescission shapes, referred to in literature as multimodal or multichannel fission (see for example [6, 30, 56, 57]).

In the pre-actinide region ($A \lesssim 220$), predominantly symmetric MD's were observed by means of either charge-particle-induced reactions [36–38] or EM fission [5, 6]. However, recent βDF experiments revealed a new region of asymmetry around ^{178,180}Hg with most probable FF-mass numbers situated around 80 and 100, see also figure 1.1 [3, 4, 47]. The mechanism behind this asymmetry is different from that in the uranium region, since strong shell effects

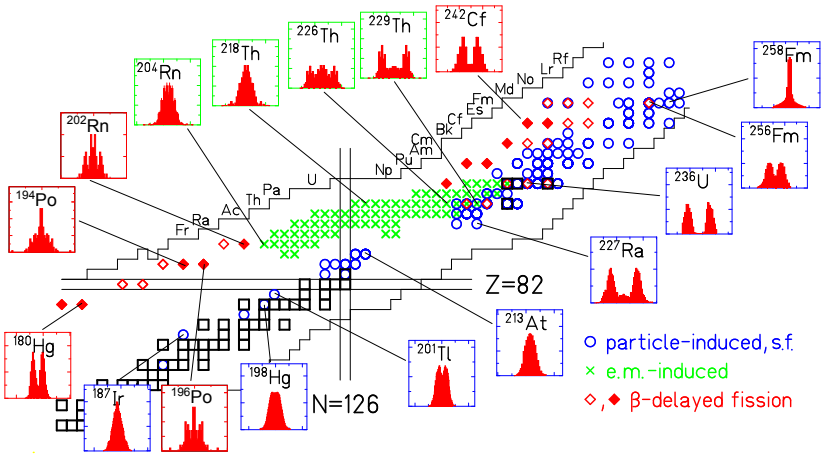

Figure 2.6: (In color) Part of the nuclear chart showing all nuclei studied through low-energy fission. The blue circles indicate mass distributions measured through particle-induced or spontaneous fission experiments. Nuclear-charge distributions resulting from electromagnetically-induced fission [5, 6] are denoted by green crosses. The fissioning daughters of the 26 known βDF cases are indicated by red diamonds, where the 11 filled symbols indicate nuclei for which fission-fragment masses have been measured. Some key distributions are depicted, whereby the X-axis denotes FF masses or nuclear charges (in the case of EM-induced fission) and the Y-axis the corresponding yields. Adapted from [58] and [42].

in the FFs are absent here. Nonetheless, several theoretical models succeeded in reproducing these observations [60–63], as will be discussed further in section 2.4.

This thesis presents a βDF study of ^{194,196}At and ^{200,202}Fr, allowing to map the transition region between symmetric fission around ^{204}Rn and asymmetry in ^{180}Hg. Indications for multi-modal fission were found in the mass and TKE distributions of daughter nuclei ^{194,196}Po and ^{202}Rn, see also Figure 2.6. A detailed discussion on the analysis and interpretation of latter results is presented in Chapter 5.

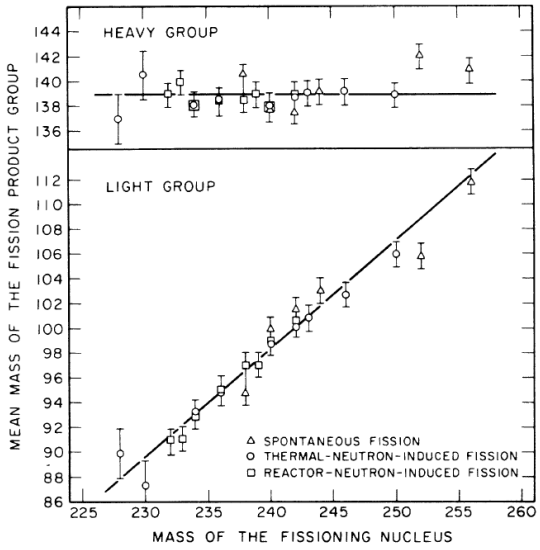

Figure 2.7: Average mass numbers of the light and heavy FFs as a function of the mass numbers of the fissioning isotope. [59]

2.4 Fission models

Over the past decades, multiple models for describing the fission process have emerged. Roughly, these theories can be subdivided into three main categories. The macroscopic-microscopic approach combines a macroscopic description of a nucleus, such as the liquid-drop model, with microscopic shell corrections. A mean-field approach, on the other hand, regards the nucleus as consisting of interacting fermions inside a mean-field potential. Finally, scission-point models consider a thermal equilibrium between the nascent fragments at the scission point. These approaches are discussed in more detail below, although this section is not meant to provide a full review of all fission models. Rather, a special emphasis is given to the models providing theoretical calculations on fission in the neutron-deficient lead region, the main subject of this PhD thesis.

2.4.1 Macroscopic-microscopic models.

Soon after its discovery, Meitner and Frisch emphasized the analogy of the fission process with the division of a fluid sphere into two smaller droplets [14].

This liquid-drop theory of fission was further developed by Bohr and Wheeler, who estimated, for example, FF kinetic energies, masses and fission-barrier energies [23] (see also section 2.1.1). This macroscopic theory provided an adequate description of the fission properties which were observed at that time. However, later experiments soon revealed several discrepancies with the model predictions. For example, a nucleus would become increasingly unstable against nuclear deformation until the fission-barrier energy drops below zero around $Z \simeq 100$, which would imply a half-life for these elements of only $\sim 10^{-19}$ s. Nowadays however, elements up to $Z = 118$, with half-lives of more then a few days have been synthesized [64]. In many of these nuclei, decay via α emission is even favored over fission. Moreover, it is expected that the nuclear chart would extend even further (see e.g. [8]). The liquid-drop based model predicted a strong tendency for symmetric fission, incompatible with the experimental data presented in section 2.3.

These phenomena were interpreted as manifestations of microscopic shell effects in the fissioning nucleus and its respective fragments. In the 1960's, Strutinsky developed a method to calculate microscopic shell corrections for any nucleus with respect to its deformation [65, 66]. These corrections may alter the fission-barrier energy significantly, explaining, for example, the stability of superheavy elements against fission beyond $Z \simeq 100$, as illustrated in Figure 2.8. Furthermore, Figure 2.8 shows how the experimental observation of short-living fission isomers in the actinide region can be understood from the emergence of a local minimum in the potential-energy curve with respect to deformation.

The potential energy of a certain nucleus with a certain shape can be calculated as the sum of a macroscopic part and a microscopic term. In this manner, multi-dimensional potential-energy surfaces can be created to identify fission paths with respect to different deformation parameters. For example, the model described in [57, 67] provides five-dimensional potential-energy surfaces (PES) for probing the deformation space of the fissioning nucleus. The chosen parametrization of these PES is schematically given in Figure 2.9 and includes the elongation in the fission direction Q_2; the neck diameter d; the mass asymmetry of the nascent fragments α_g and their quadrupole deformations ϵ_{f1} and ϵ_{f2}. The macroscopic part of the potential energy is described by the finite-range liquid-drop model (FRLDM), whereby the nuclear energy is calculated by means of a double volume integral of a Yukawa-plus-exponential folding function [68, 69]. The microscopic energy includes both shell and pairing corrections. The former are calculated by employing Strutinsky's method [65, 66] and the latter by using the Lipkin-Nogami method [70].

This model reproduced well several aspects of FF mass and energy distributions.

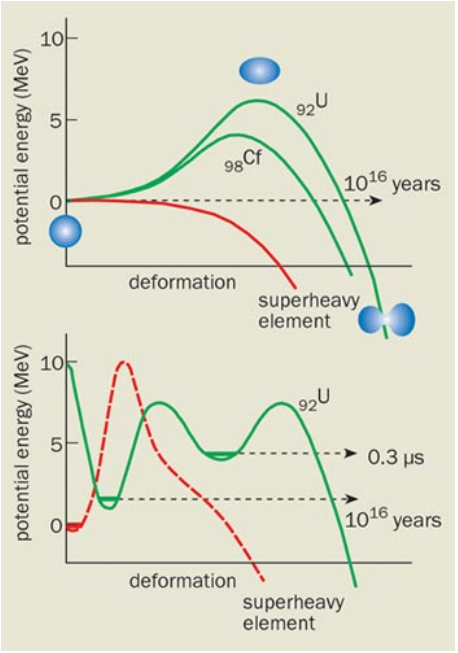

Figure 2.8: (In color) Comparison of the macroscopic liquid-drop (top) and a macroscopic-microscopic approach (bottom). The latter model can explain the stability of the heavy element hassium with $Z = 108$ (red curves) against fission, since microscopic effects significantly increase the fission-barrier height. Furthermore, the existence of experimentally observed short-living fission isomers in uranium nuclei is explained by the emergence of a local minimum at high deformations.

For example, bimodal fission around ^{258}Fm and triple-humped mass distributions around ^{226}Th emerge from multiple, separated fission paths in the PES [57]. This phenomenon is further illustrated in Figure 2.10, where the potential-energy curves for both the symmetric and asymmetric mode in the fission of ^{228}Ra are shown with respect to the nuclear deformation parameter Q_2. In addition, these two modes are well separated by a high ridge.

The asymmetry throughout the actinide region below Fm, with the heavier fragment having a mass number close to 140, is also well reproduced within this model. In addition, the recently found asymmetry in ^{180}Hg can also be explained by structures in the PES, as illustrated in Figure 2.11a. However, its structure is vastly different from typical PES in the actinide region, as is shown for the typical case of ^{236}U in Figure 2.11b. In the case of ^{236}U, the asymmetric

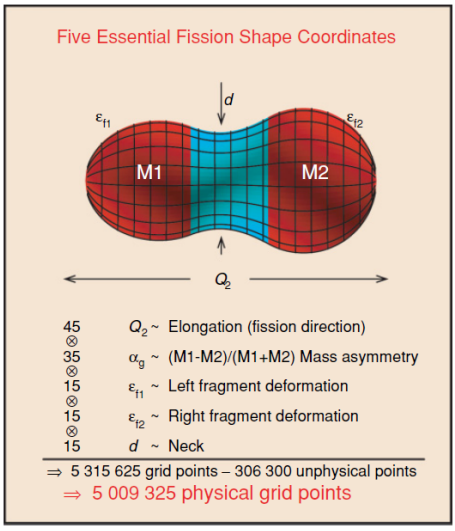

Figure 2.9: (In color) Five-dimensional shape parametrization, used in the FRLDM model to describe a fissioning nucleus. More details are given in the main text. Figure taken from [71].

pathway is shielded from the symmetric valley along its entire path. In contrast, for ^{180}Hg the ridge separating symmetric and asymmetric valleys disappears at moderately large elongations [72]. At that point, however, a descent to the symmetric valley is strongly hindered due to the small-radius neck, prohibiting the flow of matter between the fission fragments [3].

In 2011, a novel method was developed to probe these PES by simulating the shape evolution by a Metropolis random walk over the nuclear-shape surface [73]. The probability to move from a lattice point i to a point i' on the PES is then determined by the difference in potential energies associated with these points and the corresponding temperature of the nuclear system, in analogy with a Brownian motion. This Brownian Metropolis shape-motion treatment allowed to determine precise mass distributions for a wide variety of fissile isotopes and was benchmarked with 70 measured yields from EM-induced fission [5, 6]. In Figure 5.1 of chapter 5 (or Figure 1 in [74]), mass distributions calculated by this method are compared to measured yields in the pre-actinide and neutron-deficient lead region. Observed similarities and discrepancies are also discussed there.

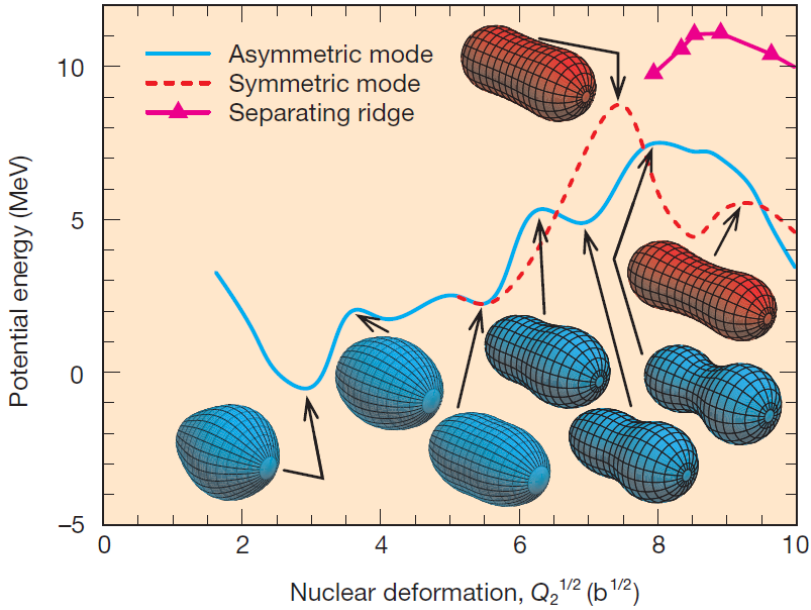

Figure 2.10: (In color) Calculated fission paths for ^{228}Ra by employing FRLDM, shown with respect to the quadrupole-deformation parameter Q_2. Two different fission valleys, corresponding to symmetric or asymmetric fission are well separated by a ridge. Several nuclear shapes are represented at different points on the fission pathways. Figure from [57]

Another macroscopic model of the nucleus is a statistical Thomas-Fermi model, which actually forms the transition between microscopic-macroscopic models and mean-field models, discussed in section 2.4.2. Indeed, the macroscopic potential energy is now regarded as a gas of nucleons interacting through an effective two-body potential, similar to a mean-field description of nuclei, but microscopic corrections are still required [75]. The calculated fission-barrier energies of this model agree well with experimental information [76, 77]. In addition, a simple algebraic expression was proposed to accurately calculate Thomas-Fermi fission barriers for a wide variety of nuclei [10].

2.4.2 Mean-field descriptions

In a Hartree-Fock Bogliubov (HFB) model, the nucleus is approximated by a fermion gas of non-interacting quasi-particles, moving in a mean-field potential.

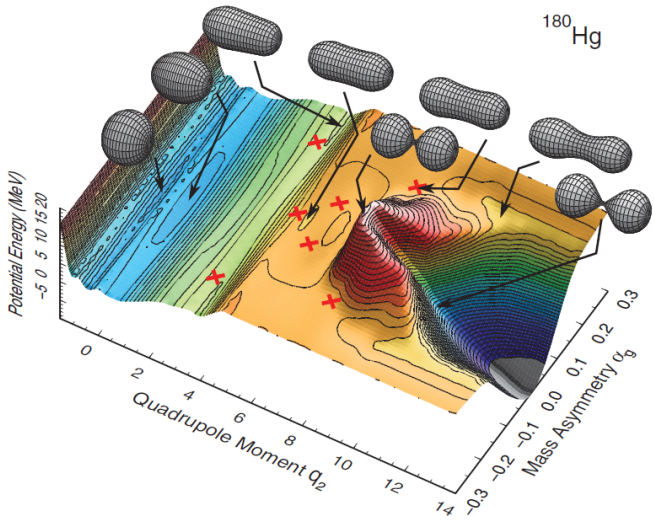

(a)

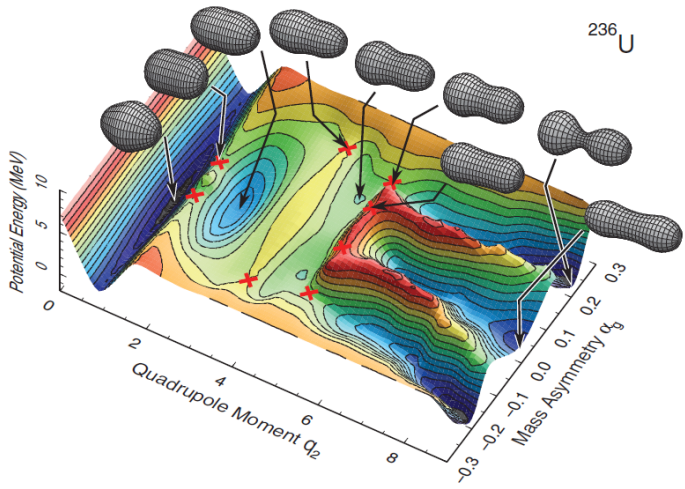

(b)

Figure 2.11: (In color) The two-dimensional PES for ^{180}Hg (a) and ^{236}U (b) with respect to elongation and asymmetry, calculated by the FRLDM in a five-dimensional analysis. A representation of the nuclear shapes is shown at different places on the surfaces. Note that, although both nuclei fission asymmetrically, their PES differ considerably.The figures are taken from [72].

This potential is created by the nucleons themselves and is determined by a self-consistent method. A detailed description of such models is given in e.g. [78], while a review of contemporary (beyond) mean-field models is given in [79].
The basic building block of any mean-field model is a set of single-nucleon wave functions ψ_i,

$$\psi_i(\mathbf{x}), i = 1, ...N_{\mathrm{wf}}, \quad \mathbf{x} = (\mathbf{r}, \sigma, \tau), \tag{2.17}$$

whereby the number of wave functions N_{wf} exceeds the number of nucleons A. The spatial coordinates are denoted by $\mathbf{r}$, spin and isospin are represented by σ and τ respectively. Within the Hartree-Fock model, the exact nuclear state $|\Phi\rangle$ is approximated by a single slater determinant

$$|\Phi\rangle = \det\{\psi_i(\mathbf{x}), i = 1, ..., A\}. \tag{2.18}$$

In terms of the fermion creation operators $\hat{a}_i^+$, corresponding to ψ_i, one can write

$$|\Phi\rangle = \prod_{i=1}^{A} \hat{a}_i^+ |0\rangle \tag{2.19}$$

Pairing correlations are then introduced by the concept of independent quasi-particle states ϕ_n with corresponding creation operators $\hat{b}_i^+$, defined by the Bogoliubov transformation

$$\hat{b}_k^+ = \sum (U_{ik}\hat{a}_i^+ + V_{ik}\hat{a}_i). \tag{2.20}$$

A widely used simplification of the HFB method is the BCS approximation, whereby equation 2.20 reads

$$\hat{b}_k^+ = u_k\hat{a}_k^+ + v_k\hat{a}_k. \tag{2.21}$$

The ground state $|\Phi\rangle$ is then obtained by minimizing the total energy E

$$E = \langle\Psi|\, \hat{H}\, |\Psi\rangle\,, \tag{2.22}$$

with the hamiltonian $\hat{H}$ consisting of a kinetic-energy term $\hat{T}$ and a two-body interaction $\hat{V}$,

$$\hat{H} = \hat{T} + \hat{V}. \tag{2.23}$$

Mean-field models mainly differ in their choice on the effective interaction potential $\hat{V}$, which can be subdivided in three main categories : Skyrme interactions [80]; Gogny forces [81, 82]; and relativistic mean-field models [83, 84].
Since HFB states are not eigenstates of the particle number operators $\hat{N}_p$, the minimization of E should have constraints on the neutron and proton numbers N_q:

$$\langle \Psi | \hat{N}_q | \Psi \rangle = N_q. \tag{2.24}$$

Lagrangian multipliers λ_q are therefore introduced and one should minimize

$$E^{\lambda} = \langle \Psi | \hat{H} | \Psi \rangle - \sum_{q=n,p} \lambda_q \langle \Psi | \hat{N}_q | \Psi \rangle \tag{2.25}$$

in a self-consistent way.
If the nuclear energy variation is probed with respect to nuclear deformation, for example in fission research, spatial constraints are introduced. Therefore, an extra term is added to the total Routhian E^{λ} as

$$E^{\lambda} = \langle \Psi | \hat{H} | \Psi \rangle - \sum_{q=n,p} \lambda_q \langle \Psi | \hat{N}_q | \Psi \rangle + \frac{1}{2} \sum_{\alpha} C_{\alpha} (\langle \Psi | \hat{Q}_{\alpha} | \Psi \rangle - \mu_{\alpha})^2, \tag{2.26}$$

with $\hat{Q_{\alpha}}$ representing multipole operators for the calculation of quadrupole, octupole or higher multipole moments. The desired value of the expectation value $\langle \Psi | \hat{Q}_{\alpha} | \Psi \rangle$ is denoted by μ_{α}. By varying the values of μ_{α}, potential-energy surfaces, similar to the ones shown in 2.11a, can be constructed. Calculations in the neutron-deficient lead region considered, for example, Skyrme energy density functional SkM* or Gogny D1S interactions [61, 85]. A calculated potential-energy surface using the latter interaction for ^{196}Po is presented in Figure 5.4 of chapter 5 (or Figure 4 in [74]).

The static mean-field approaches, as described above, provide to lowest-order nuclear potential energies. However, a higher accuracy can be achieved by going beyond the mean-field approach and considering, for example, the restoration of symmetries which were broken during the minimization procedure. Recently,

considerable progress is made to account for these effects in a beyond mean-field description of fission [86].

2.4.3 Scission-point models

The so-called scission-point models consider a statistical quasiequilibrium between the nascent fission fragments at or near the scission point. Only the microscopic structure of the FFs, and not that of the mother nucleus, is thus taken into account.
Such calculation thus involves an energy calculation of all possible configurations at scission. In the original scission-point model [87], the total potential energy of the system is given by the sum of the liquid-drop and microscopic correction terms of the individual spheroids with the potential-energy terms describing the interaction between both fragments. In addition, a collective temperature of the fissioning system is introduced. This model illustrated the importance of the double spherical shell closure around ^{132}Sn for the stability of the heavy-mass peak in the fission of actinides. In addition, the transition from asymmetry around uranium to symmetry found in the lighter thorium isotopes was reproduced [88]. Furthermore, improved scission point models could successfully explain the observed mass split in the fission of ^{180}Hg [62, 63].

Chapter 3

Experimental setup at ISOLDE-CERN

The detection of βDF in the neutron-deficient lead-region involves short-living radioactive species, with half lives of less than one second. Such experiments are conducted at the ISOLDE facility situated at the European organization for nuclear research (CERN). This facility can deliver pure, low-energy beams of short-living radioactive nuclei, which are essential to conduct the measurements. Section 3.1 gives a description of the ISOLDE facility coupled to the CERN accelerator complex. The setup, used for the detection of fission fragments, α, β and γ particles, is described in section 3.2, while section 3.3 discusses the data acquisition.

3.1 ISOLDE

The CERN accelerator complex is a succession of accelerators boosting a proton beam to increasingly higher energies. After acceleration to 50 MeV by the linear accelerator LINAC 2, the beam is transferred to the Proton Synchrotron Booster (PSB) where protons reach energies of 1.4 GeV. The Proton Synchrotron (PS) and Super Proton Synchrotron (SPS) can then boost the beam energy to 25 and 450 GeV respectively. Finally, the protons are injected in the Large Hadron Collider (LHC), a 27-kilometer ring where particle energies up to 7 TeV can be reached. Moreover, two fully accelerated proton beams can collide in a head-on-head collision making up a total energy of maximum 14 TeV. Protons

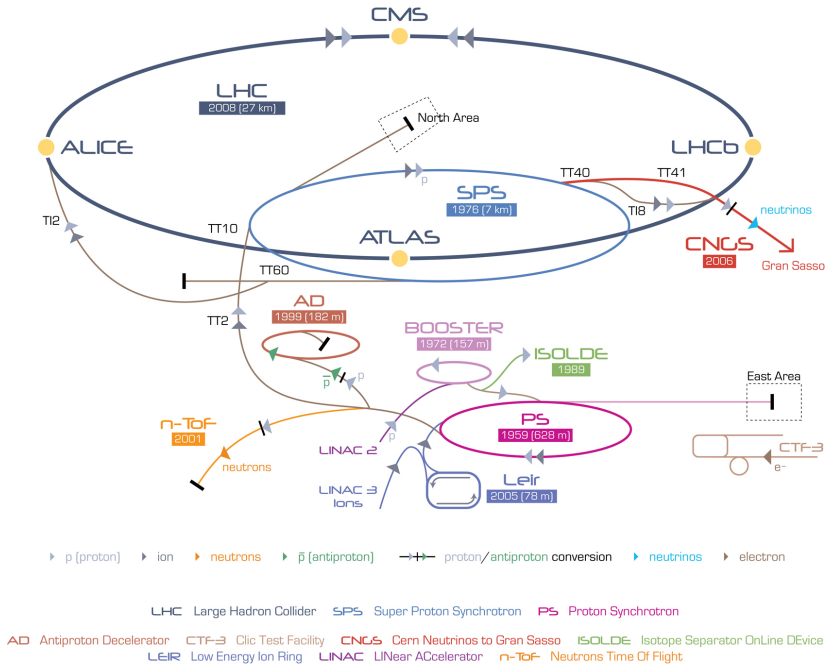

Figure 3.1: (In color) The CERN accelerator complex, including the most prominent experimental installations to which protons are diverted. The ISOLDE facility is placed after the Proton Synchrotron Booster (PSB). The figure is taken from [89].

from the PSB, PS or SPS can also be transferred to a variety of experimental facilities, as illustrated in Figure 3.1.

One of such installations is the Isotope Separator On Line DEvice (ISOLDE) [90], where the 1.4 GeV protons from the PSB serve to produce radioactive nuclei. The PSB delivers pulsed beams, whereby the bunches are separated in time by about 1.2 s and each pulse, with a duration of a few μs, can contain up to 3×10^{13} protons. The proton delivery to the different installations happens in a controlled sequence, a super cycle (SC), consisting of a number of proton pulses varying between 12 and 42. A typical SC sequence is shown in Figure 3.2.

A view of the layout of the ISOLDE facility is shown in Figure 3.3, and the production of pure radioactive ion beams is schematically depicted in Figure 3.4. First, the PSB proton beam impinges on a thick target, thereby creating a

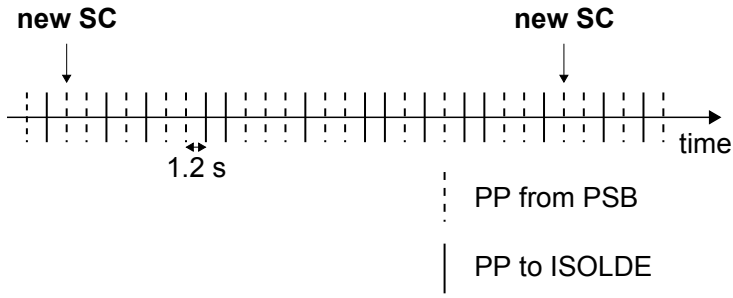

Figure 3.2: An example for the distribution of proton pulses (PP) from the PSB, grouped in regular super cylces (SC). Here, a SC of 25 PP is depicted, of which 11 are transported to the ISOLDE separator.

cocktail of isotopes through a variety of nuclear reactions. At and Fr isotopes are produced via spallation reactions on a $50\,\mathrm{g/cm^2}$ thick UC_x target, which is kept at a temperature of about 2500 K to enhance effusion and diffusion of produced nuclei to the transfer line. Selective ionization mechanisms are then applied to extract isotopes from the element of interest. Atoms with a relatively low ionization potential, such as Fr and Tl, can be ionized by collisions with the hot surface of the transfer tube. This surface-ionization effect always occurs and may thus cause unwanted isobaric contamination in certain radioactive beams. In this work for example, a high Tl contamination was observed when investigating neutron-deficient At and Fr isotopes (see also chapter 4).
Another, highly-selective, technique is resonant laser ionization, performed by the resonance ionization laser ion source (RILIS). First, a neutral atom is stepwise excited by one or two tunable dye or Ti:Sa lasers. Then, ionization occurs by further excitation to a Rydberg state, auto-ionizing level or the continuum [91]. For the production of At beams, a recently developed ionization scheme is employed, see Figure 3.5 [92]. In this experimental campaign, the fundamental frequencies of the first and second-step dye lasers were kept at 15411.2 and 10923.5 $\mathrm{cm^{-1}}$ respectively (measured in air). The frequency of the first-step dye laser was tripled.

The target-ion source was kept, during current measurements, at an electric potential of +30 kV relative to the ground potential. Newly formed ions are extracted and accelerated to a kinetic energy of 30 keV by means of an extraction electrode. Before transportation to the detection setup, the beam is mass separated by a dipole magnet, either the general purpose separator (GPS) or the high resolution separator (HRS). In a first-order approximation, the curvature radius ρ of a single-charged ion of mass M and energy E in a magnetic

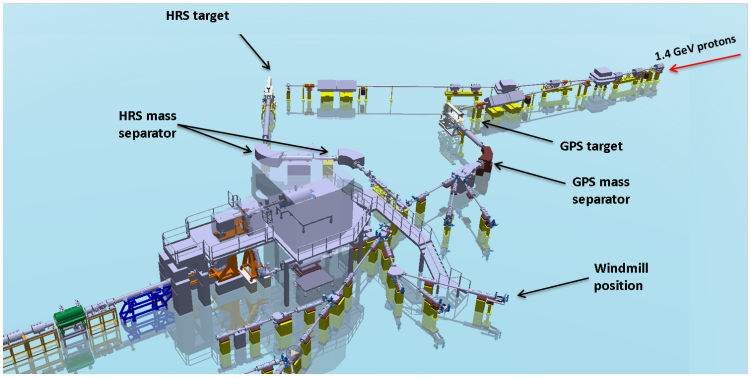

Figure 3.3: (In color) Layout of the ISOLDE facility. The protons from the PSB can either be directed to the GPS or HRS target modules. The position of the employed detection setup, the so-called 'Windmill' system is also indicated.

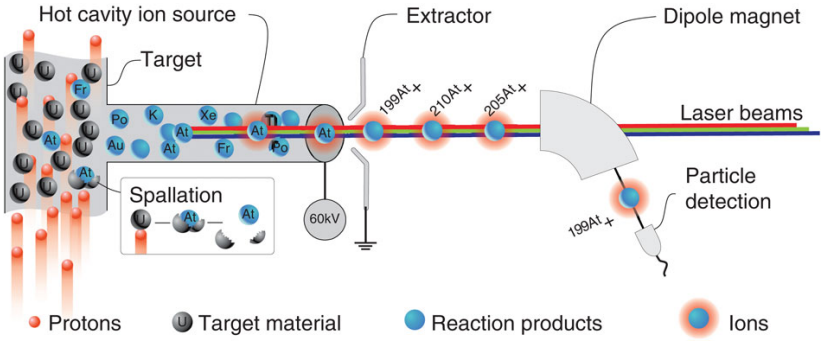

Figure 3.4: (In color) A schematic representation of radioactive-beam production at the ISOLDE facility. A variety of nuclei is created by energetic protons impinging on a thick target, such as UC_x. After selective ionization, extraction and mass separation, pure isotopic beams are transported towards the detection setup. Figure from [92].

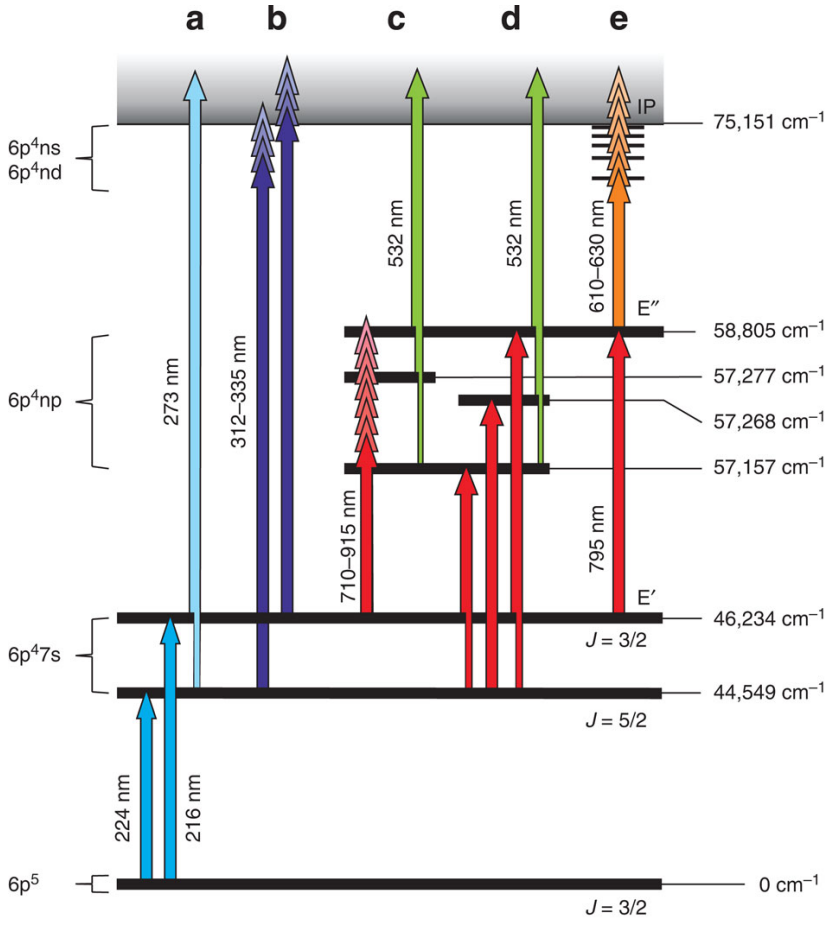

Figure 3.5: (In color) Overview of different excitation paths for the resonant laser ionization of At. Figure from [92].

field B equals

$$\rho = \frac{\sqrt{2ME}}{Be}. \tag{3.1}$$

However, imperfections in the homogeneity of the magnetic field; optical properties of the beam; elastic and inelastic collisions with the rest gas; and incomplete acceleration of the extracted ions may cause a spread in ρ for ions with a specific mass M. Therefore, mass-analyzing magnets have a non-zero resolving power R, defined as $R = M/\Delta M$, whereby ΔM is the full width at half maximum of an ion beam with mass M. The GPS has a theoretical mass resolving power of more than 1000, while the R of HRS should exceed 5000 [93]. Due to its high resolving power, HRS can in some cases (partially) separate isobars. For example, the relative mass difference between ^{200}Fr and ^{200}Tl is 5.6×10^3 [94], which is close to R of HRS.
As illustrated in Figure 3.6, the mass peaks from a dipole magnet exhibit long asymmetric tails, mainly due to collisions with the rest gas and incomplete ion acceleration [95]. Hence, an ion beam with desired mass number A may be contaminated by isotopes with different mass numbers A'. This contamination will be more severe when the production yields of the contaminating nuclei are higher in comparison to the isotope of interest. Since the mass resolving power of HRS is considerably higher then the one of GPS, this contamination should be more prominent for the latter separator. Indeed, this work shows clear evidence for mass contamination in beams from GPS, in contrast to the relatively pure HRS beams. On the other hand, the transmission of the ion beam through the GPS separator is significantly higher than for HRS. The purity and intensity of observed ion beams are discussed in more detail in chapter 4.

3.2 The 'Windmill' detection setup

The isotopically purified beam from the ISOLDE separator is finally transported to the so-called 'Windmill' (WM) detection system, depicted in Figure 3.7. The beam is implanted on one of ten identical carbon foils, with a thickness of about 20 μg/cm^2, mounted on a rotatable wheel. The thickness of the carbon foils is chosen to fully stop the 30 keV ion beam, but thin enough to let escape emitted decay radiation such as α particles and fission fragments. The wheel contains also two ^{241}Am sources (one on the front and one on the back side) for calibration purposes. Silicon detectors, placed on either side of the implantation foil, are employed for the detection of α, β and fission particles. One of these detectors has a hole of 8 mm, allowing the ion beam to pass. Both detectors at

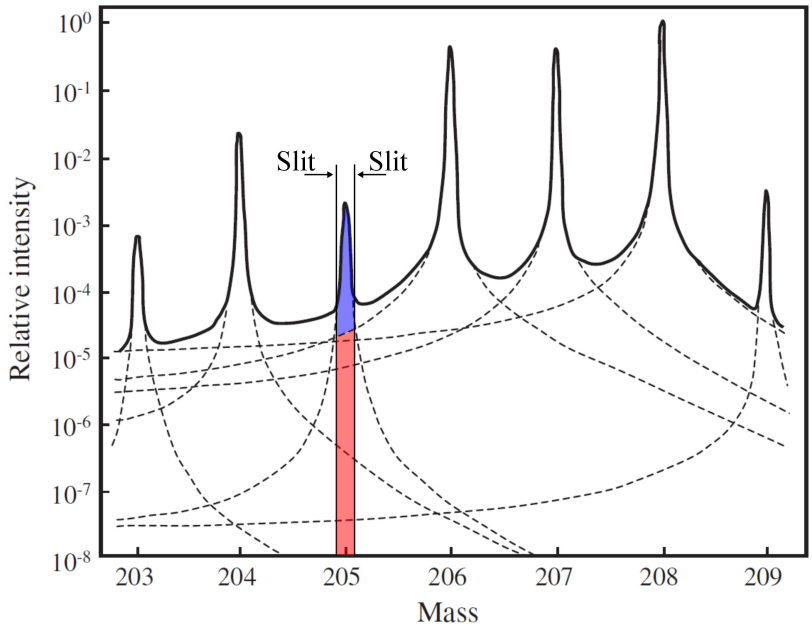

Figure 3.6: (In color) Spectrum of an ion beam after mass separation. The mass peaks have long and asymmetric tails due to collision with the rest gas in the separator, or an incomplete acceleration of the ions. These tails can cause a significant mass contamination, even when introducing narrow slits. For example, when selecting a beam with desired mass 205 (blue color), the contamination of higher masses (red) can be up to 1% of the total beam content. Figure adapted from [91].

the implantation side are of the surface-barrier type, manufactured by ORTEC, and have a depletion depth of about 300 μm. The annular detector has an active surface of 450 mm^2, including the hole, compared to 300 mm^2 for the circular detector. The total solid angle covered by these detectors is about 51 % [47] of 4π. Figure 3.8 shows a full-range energy spectrum as recorded by the full circular silicon detector at the implantation side after nearly 44 hours of data-taking at the HRS separator on the βDF of ^{202}Fr. The low-energy events, below 1 MeV, correspond to β^+ particles and conversion electrons. At higher energies, roughly between 5 and 10 MeV, alpha particles can be distinguished. The events situated between 10 and 20 MeV are explained as random summing of α particles in the detector. Fission fragments have energies above $\sim$50 MeV, clearly separated in energy from the α particles. Furthermore, no high-energy signals ($\gtrsim$ 20 MeV) were recorded in dedicated background measurements before

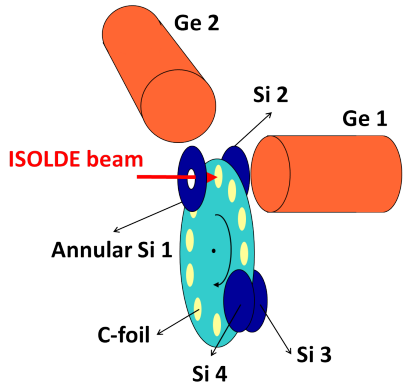

(a)

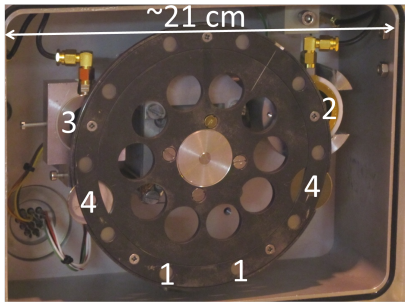

(b) Different parts of the WM system are indicated by numbers : 1) carbon foils; 2) annular silicon (surface-barrier) detector Si 1; 3) silicon (PIPS) detector Si 4; 4) ^{241}Am source for calibration purposes.

Figure 3.7: (In Color) A schematic view (a) and photograph (b) of the Windmill (WM) system. A radioactive beam from ISOLDE is implanted in one of ten ultra-thin carbon foils ($\sim 20\,\mu$g/cm^2), mounted on a rotatable wheel. Four silicon detectors are employed for the detection of electrons, α and fission particles. Two germanium detectors are placed outside the vacuum chamber for γ-ray detection.

and after the actual data-taking, indicating a very low background rate. Figure 3.8 demonstrates that the α-decay rate exceeds the βDF rate by many orders of magnitude, which is further quantified in Table 5.1 (or Table I in [74]). The α-decay, obtained here as by-product, contains for a number of isotopes new information and has also been analyzed (see also section 4.2).

After a certain implantation time, the irradiated foil can be moved to the decay position, where a pair of silicon detectors is mounted (Si 3 and 4 in Figure 3.7). These Passivated Implanted Planar Silicon (PIPS) detectors are manufactured by Canberra, have a depletion depth of 300 μm and an active surface of 300 mm^2.

Emitted γ rays are detected by single-crystal High-Purity Germanium (HPGe) detectors from Canberra. The detector closest to the carbon foil is denoted by Ge 1 and the other by Ge 2 (see also Figures 3.7 and 3.9). The energy and efficiency calibration was determined for the IS466-III run in May 2011 at HRS (an overview of the experimental campaigns is found in section 4.1), using ^{60}Co, ^{133}Ba,^{137}Cs and ^{152}Eu calibration sources (see also Table 3.1).

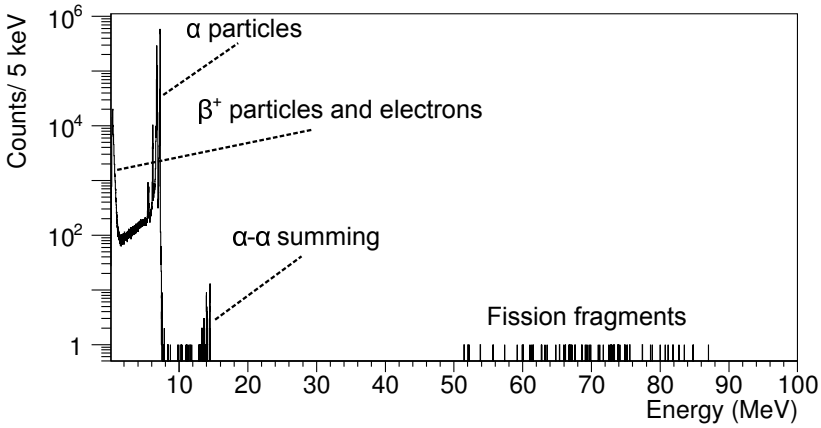

Figure 3.8: A full-range energy spectrum as recorded by the silicon detector (Si 2) at the implantation side of the WM system, depicted in Figure 3.7. The spectrum shows β^+ particles and electrons, α particles and fission-fragments recorded after nearly 44 hours of measurements on ^{202}Fr at the ISOLDE-HRS separator.

Table 3.1: The properties of the calibration sources, used for energy and efficiency calibration of the Germanium detectors. The isotope, serial number, the source strength in May 2011 and the corresponding uncertainty are listed. Since the uncertainty on the source strength is unknown in the case of ^{133}Ba, a relative error of 5% was assumed.

Source	serial no.	strength on 05/2011 (kBq)	uncertainty
^{60}Co	2669RP	1.21	3.9 %
^{133}Ba	2966.2RP	8.82	$\sim$ 5 %
^{137}Cs	2668RP	20.37	6.0 %
^{152}Eu	2670RP	9.53	8.7 %

The solid angle covered by Ge 1 is 37% of 4π, while Ge 2 covers 8% of 4π. Apart from this geometrical factor, also the the chance to detect the full energy of a photon, the photo-peak efficiency, should be considered in the calibration. The photo-peak efficiency depends on the energy of the photon E_γ, the attenuation of photons by material of the vacuum chamber and the detector window and on the average number of γ rays emitted in coincidence with this γ ray, denoted by the multiplicity (no coincident γ's corresponds to a multiplicity of 1). Multiple γ rays emitted promptly from a source have a significant chance to hit the same detector crystal, resulting in a summing of the signal and a reduction of the efficiency. This effect is more severe for higher γ-ray multiplicities. Due to the larger solid-angle coverage, this effect is more prominent for Ge 1 as compared to Ge 2.

In what follows, the absolute photo-peak efficiency ϵ_γ to detect a single photon with energy E_γ was deduced for Ge 1 and Ge 2 using a combination of different methods. One method involves the absolute source strength A_0 given in Bq and the number of observed gamma rays N_γ from a certain transition. The efficiency ϵ_γ is then given by

$$\epsilon_\gamma = \frac{N_\gamma}{A_0 t b_\gamma}, \tag{3.2}$$

where t is the total measurement time in seconds and b_γ the absolute γ branching ratio. In the case of ^{60}Co, ^{133}Ba and ^{152}Eu, γ rays are often emitted in cascade (multiplicity higher than one), and the summing effect is significant. GEANT4 simulations have shown that this effect can influence the deduced efficiencies of Ge 1 by $10 \sim 15\,\%$ in the case of ^{152}Eu. This effect is much smaller for Ge 2, because of the smaller solid-angle coverage, and this method was therefore considered to give a reliable curve for the single-photon efficiency of Ge 2. For ^{137}Cs, the main γ line at 662 keV directly feeds the ground level and summing effects are absent.

In the case of Ge 1, the coincidence method described in [96] is applied. This method can be used when having two or more detectors available and a particular γ ray γ_1 is followed by another photon γ_2. This situation is illustrated in Figure 3.9 for an excited level of energy E_2 with the only de-excitation path involving the γ-ray cascade γ_1-γ_2. The efficiency for detecting the photon γ_1 in Ge 1, denoted by ϵ_{γ_1}(Ge 1), is then given by

$$\epsilon_{\gamma_1}(\text{Ge 1}) = \frac{N_{\gamma_2\gamma_1}(1+\alpha_1)}{N_{\gamma_2}(\text{Ge 2})}, \tag{3.3}$$

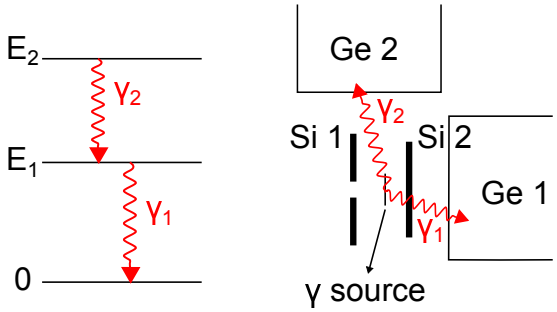

Figure 3.9: (In color) Schematic illustration of the coincidence method to determine the efficiencies of the HPGe detectors Ge 1 and Ge 2 in the WM setup (see Figure 3.7). A cascade of two γ rays, denoted by γ_1 and γ_2 are emitted from a γ source placed at the foil position.

where α_1 is the total conversion coefficient corresponding to the transition $E_1 \rightarrow 0$ and $N_{\gamma_2}(\text{Ge 2})$ the amount of γ_2 rays detected in Ge 2. The amount of events whereby γ_1 and γ_2 are detected simultaneously in detectors Ge 1 and Ge 2 respectively, is denoted by $N_{\gamma_2\gamma_1}$. The efficiency for detecting a photon γ_2 can be calculated in a similar way. When applicable, other de-excitation paths of the level E_2 should be taken into account, as described in [96].
Because equation 3.3 involves the detection of coincident photons γ_2 in Ge 2 to determine $\epsilon_{\gamma_1}(\text{Ge 1})$, the effect of summing in Ge 1 is less important when using this method. Therefore, the coincidence method was considered to give a better estimate for the single-photon efficiency of Ge 1 when cascades are involved.

A third method involves the ^{241}Am α-calibration source ($\sim 50\,$Bq) mounted on the wheel (see Figure 3.7). The main α peak at 5486 keV of ^{241}Am is in coincidence with a 60 keV γ transition to the ground state. In this case, the number of observed α particles N_α and the amount of α-γ coincidences $N_{\alpha\gamma}$ can be used to determine the γ efficiency ϵ_γ as

$$\epsilon_\gamma = \frac{N_{\alpha\gamma}(1+\alpha)}{N_\alpha}, \tag{3.4}$$

with α the total internal conversion coefficient of the transition.

The data points for the efficiency determination, using the above three methods, are summarized in Tables 3.2 and 3.3 for Ge 1 and Ge 2 respectively. The

Table 3.2: Data points used in the efficiency calibration of the HPGe detector Ge 1, used in the IS466-III ISOLDE run in May 2011 (see also Figure 3.7). The γ efficiencies ϵ_γ with corresponding energies E_γ from specific sources are listed. The methods employed for efficiency determination listed in the last column, namely 'source strength','γ-γ' and 'α-γ', correspond to equations (3.2), (3.3) and (3.4) respectively. For the two latter methods, the corresponding energy of the coincident γ or α line is given between brackets.

Source	E_γ (keV)	ϵ_γ (%)	method
^{241}Am	59.5	2.8(3)	α-γ (5486 keV)
^{152}Eu	121.8	9.7(8)	γ-γ (245 keV)
	244.7	8.4(7)	γ-γ (122 keV)
	344.3	7.9(4)	γ-γ (779 keV)
	344.3	7.6(10)	γ-γ (411 keV)
	411.1	5.7(8)	γ-γ (344 keV)
	778.9	4.5(5)	γ-γ (344 keV)
^{133}Ba	81.0	6.3(7)	γ-γ (303 keV)
	81.0	6.4(4)	γ-γ (356 keV)
	302.9	9.4(12)	γ-γ (81 keV)
	356.0	8.0(6)	γ-γ (81 keV)
^{137}Cs	661.7	4.9(3)	source strength
^{60}Co	1173.2	3.1(2)	γ-γ (1332 keV)
	1332.5	2.8(2)	γ-γ (1173 keV)

efficiency to detect a γ ray with energy E_γ,$\epsilon_\gamma(E_\gamma)$, is determined by a fit with the function

$$\epsilon_\gamma(E_\gamma) = \exp\left(\sum_{i=0}^{4} a_i \left[\ln\left(\frac{E_\gamma}{E_0}\right)\right]^i\right), \tag{3.5}$$

having five fit parameters a_i. Figures 3.10 and 3.11 show that such a function provides a good description of these data points.

3.3 Data acquisition

The detector signals from the WM system are acquired digitally, using DGF-4C modules from XIA [97]. For each recorded event, both time and energy information is stored. In addition a 10 Hz pulser indicates the effective measurement time and assesses possible deadtime effects. Finally, several

Table 3.3: Similar to Table 3.2, but for the efficiency calibration of HPGe detector Ge 2

Source	E_γ (keV)	ϵ_γ (%)	method
^{241}Am	59.5	0.08(3)	α-γ (5486 keV)
^{152}Eu	121.8	1.08(9)	source strength
	244.7	1.17(10)	source strength
	344.3	1.01(9)	source strength
	367.8	0.94(13)	source strength
	411.1	0.89(9)	source strength
	444.0	0.94(9)	source strength
	688.7	0.81(10)	source strength
	778.9	0.71(6)	source strength
	867.4	0.67(6)	source strength
	964.1	0.65(6)	source strength
	1085.0	0.64(6)	source strength
	1089.7	0.61(6)	source strength
	1112.1	0.62(6)	source strength
	1212.9	0.60(6)	source strength
	1299.1	0.53(5)	source strength
	1408.0	0.54(5)	source strength
^{133}Ba	81.0	0.53(3)	source strength
	276.4	1.07(6)	source strength
	302.9	1.04(5)	source strength
	356.0	0.97(5)	source strength
	383.9	0.95(5)	source strength
^{137}Cs	661.7	0.81(5)	source strength
^{60}Co	1173.2	0.62(3)	source strength
	1332.5	0.56(2)	source strength

timestamps, related to the measurement duty cycle, are registered by the acquisition system.

A typical cycle used during the data taking is shown in Figure 3.12 and is based on the arrival of proton pulses on the target (governed by the supercycle (SC) of the PS Booster). A measurement is triggered by the start of a new SC. However, data acquisition is only started after a fixed delay time in order to coincide with the arrival of a PP to the ISOLDE target. Data acquisition then proceeds for a fixed amount of time, usually less than the length of one SC. After such a measurement cycle, the wheel of the WM is rotated, whereby the irradiated foil is moved towards the pair of PIPS detectors, denoted by the 'decay position'. A

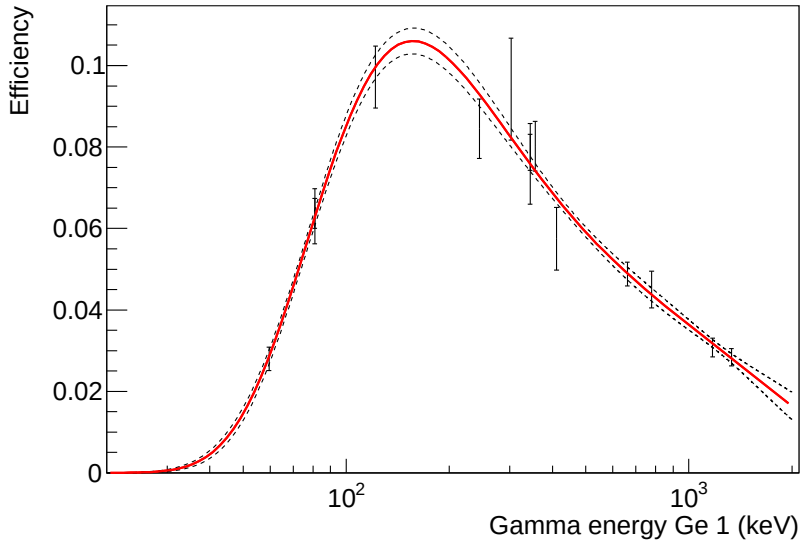

Figure 3.10: (In color) Efficiency curve of Ge 1. The data points, listed in Table 3.2, are fitted with the red curve, the function of which is given in equation 3.5. The parameters E_0 and a_2 in equation 3.5 were kept fixed at 500 keV and 0 respectively. The fitted parameters are $a_0 = -2.83(2)$, $a_1 = -0.67(7)$, $a_3 = 0.010(7)$, $a_4 = -0.10(3)$. The error on this fitted curve is given by the black dashed line.

fresh foil is simultaneously presented for beam implantation, which is governed by a so-called macro and micro cycle of the beam gate. The macro cycle prohibits beam implantation before and after one measurement cycle, in order to have no beam implantation while turning the wheel. The micro cycle allows beam implantation only for a fixed amount of time after the arrival of a PP to the ISOLDE target. For example, when dealing with short-lived species, one can choose to implant only for a limited amount of time after a PP. In this way, the unwanted implantation of longer-living radioactive contaminants, which could be present in the ISOLDE beam, is reduced. The beginning of a new SC; the start of the acquisition system; closing of the macro-cycle beam gate; and the arrival of a PP to the ISOLDE target are time stamped and recorded by the digital data-acquisition system, see also Figure 3.12.
When the buffers of the DGF modules, which can each store about 1000 events, are emptied, the acquisition of incoming signals is blocked, which may result in a significant deadtime. A readout is performed when one of the modules has a full buffer or at the end of a measurement cycle and takes about 80 ms to

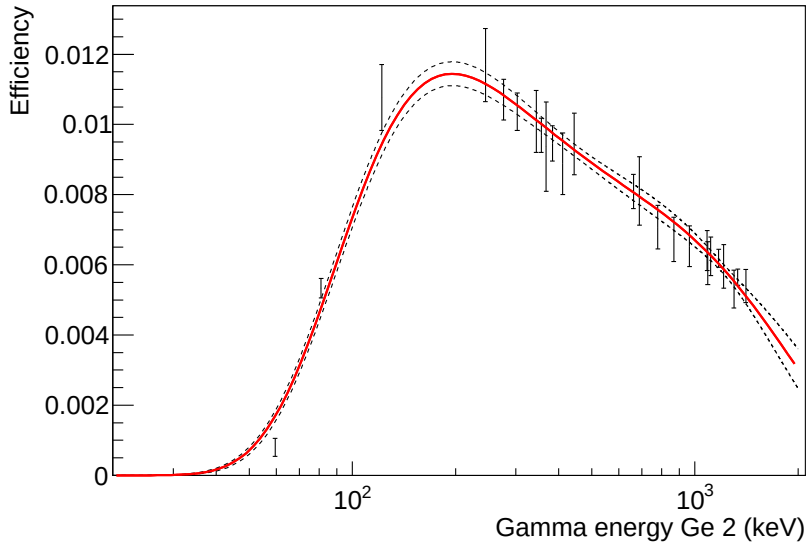

Figure 3.11: (In color) Similar as Figure 3.5, but then for Ge 2. The parameters E_0 and a_2 in equation 3.5 were kept fixed at 500 keV and 0 respectively. The fitted parameters are $a_0 = -4.72(2)$, $a_1 = -0.35(6)$, $a_3 = -0.04(6)$, $a_4 = -0.13(3)$.

complete. Because of the cyclic nature of the measurements, the first readouts may always happen at roughly the same time after the start of a new cycle. The average deadtime with respect to the start of a measurement cycle may therefore exhibit large jumps, even if the total signal loss is limited. These deadtime variations are especially important when determining lifetimes from these data. This phenomenon is further illustrated in Figure 3.13 for data taken on mass 202 during the IS466-III run.

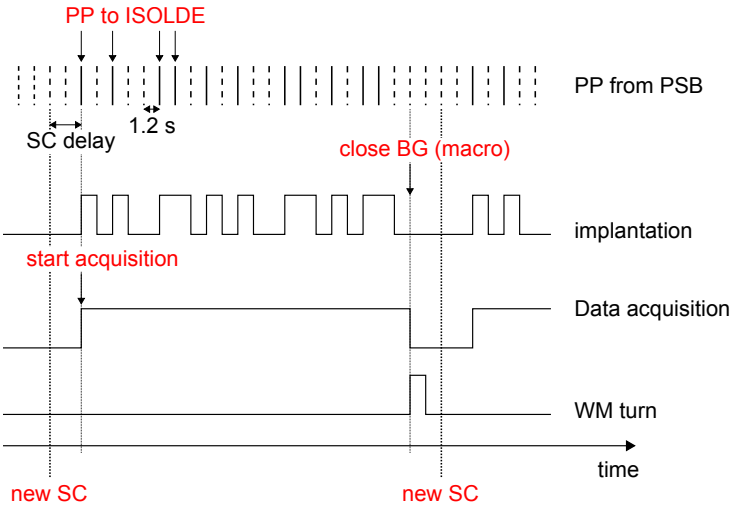

Figure 3.12: (In color) An example of a typical measurement cycle in the βDF experiments using the WM setup. Data acquisition is triggered by the start of a new SC, but is delayed by a fixed amount of time to coincide with the arrival of a PP to the ISOLDE target. Implantation proceeds, in this example, with a beam gate (BG) micro cycle of 1.2 s and with the macro cycle coinciding with the data acquisition. After one measurement cycle, the wheel of the WM system is turned. The recorded, time-stamped signals to monitor this duty cycle are marked in red. A more detailed description is provided in the main text.

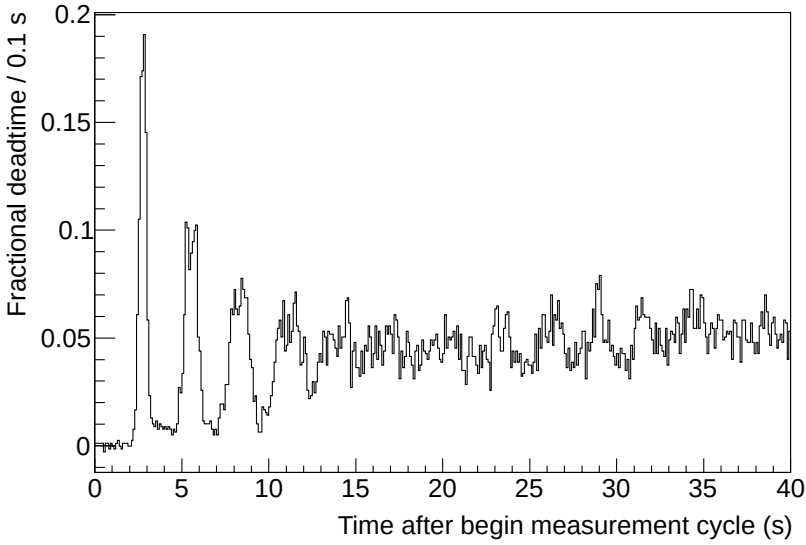

Figure 3.13: The average fractional deadtime as a function of the time after the start of a measurement cycle (see Figure 3.12) as determined from a 10 Hz pulser. The data encompass 763 identical measurement cycles acquired on mass 202 during the IS466-III run. The peaks in this spectrum correspond to readouts of the DGF buffers, happening at roughly the same moment in one cycle.

Chapter 4

Analysis

In this work, the βDF of ^{194,196}At and ^{200,202}Fr was investigated. This chapter provides an overview of the employed analysis techniques to extract various βDF properties of these isotopes. Section 4.1 provides a brief summary of the different ISOLDE βDF campaigns. In section 4.2, the purity of the implanted βDF precursors is verified by the investigation of recorded α and γ spectra. βDF probabilities and partial half-lives are derived in section 4.3. Finally, section 4.4 demonstrates how FF masses and kinetic energies can be extracted from the recorded data.

4.1 Overview of experimental campaigns

The experimental campaign at ISOLDE to measure the βDF of ^{200,202}Fr and ^{194,196}At, was divided into two main parts. The first part in May 2011 (with reference number IS466-III), employing the HRS setup, mainly involved βDF measurements of ^{202}Fr. However, a significant amount of data was also acquired on the βDF of ^{194,196}At and ^{200}Fr. An experiment dedicated to the latter isotopes was performed during the experiment in May 2012 (IS534), using the GPS setup. Tables 4.1 and 4.2 show the observed rate of both α particles and fission fragments (FF) in detector Si 2 and the total amount of observed fission fragments in that detector during the runs IS466-III and IS534 respectively. Also the total effective measurement time, as recorded by a 10 Hz pulser, is given. Due to a better beam transmission through GPS, the α and FF rates are 4 to 6 times higher in run IS534 as compared to IS466-III. However, as discussed in section 3.1, the beam purity for HRS should be superior, as is indeed verified

Table 4.1: Event rate of FFs and α particles for the isotope of interest in the detector Si 2 (see Figure 3.7) for the ISOLDE experiment IS466-III, which took place in May 2011 at the HRS. The total number of detected FFs in this detector as well as the total effective measurement time, as recorded by a 10 Hz pulser, are also given. The last column indicates during which measurements the germanium detectors (Ge det) were connected ('yes'), disconnected ('no'), or only unplugged during part of the measurement ('part').

nucleus	α rate (s^{-1})	FF rate (h^{-1})	# FF	measured time	Ge det
^{194}At	1.2	4.1	5	1 hr 13 min	no
^{196}At	90	1.7	9	5 hr 25 min	part
^{200}Fr	0.016	~ 0.05	1	21 hr 34 min	yes
^{202}Fr	30	1.6	71	43 hr 59 min	yes

Table 4.2: Idem as Table 4.1, but for the run IS534, which took place in May 2012 at the GPS.

nucleus	α rate (s^{-1})	FF rate (h^{-1})	# FF	measured time	Ge det
^{194}At	6.5	28	253	9 hr 11 min	no
^{196}At	3.1×10^2	5.2	181	35 hr 7 min	no
^{200}Fr	0.051	0.3	5	20 hr 18 min	no

in section 4.2.
Both experimental campaigns suffered from a severe contamination of isobaric Tl ions in the radioactive beam, created by the surface-ionization process. The γ rays emitted after β decay of these isotopes could therefore over-saturate the Ge detectors. As a result, γ rays were only recorded during part of the IS466-III run and the Ge detectors were completely disconnected during run IS534. The last column in tables 4.1 and 4.2, corresponding to runs IS466-III and IS534 respectively, indicates during which measurements the detectors were (partially) disconnected.

4.2 Beam composition

Figures 4.2, 4.3, 4.4 and 4.5 show the alpha spectra, as recorded by the implantation detector Si 2, during both the IS466-III experiment at HRS and the IS534 experiment at GPS. The most prominent peaks are identified and simplified decay schemes of the isotopes of interest, as found in literature, are given. In the case of ^{202}Fr, a partial fit of the recorded spectrum in run

IS466-III is shown in Figure 4.5. The fitting function was taken from [98], where an alpha peak is described as a convolution of a Gaussian with one or more exponential tails. The peak shape is assumed constant for all alpha lines in the same spectrum. Because of underlying fine structure in the ^{202}Fr alpha decay, the structure around 7.2 MeV in the α-decay spectrum could not be fitted properly with the rest of the spectrum. Such fits are employed to reliably determine peak positions and contents. The energy of the spectra are calibrated using literature energies of observed α lines.

Since the mass resolution of GPS is worse as compared to HRS, a clear difference of contamination can be observed in the α spectra. Indeed, a large amount of isotopic contamination is found in the spectra measured at GPS, while completely absent in HRS spectra. Nonetheless, α lines of the relevant isotopes can be clearly identified in all spectra. Furthermore, the FWHM of α peaks in Si 2 are measured as 33 keV and 48 keV for IS466-III and IS534 respectively, although the same detector is used in both runs. This resolution deterioration during run IS534 might be caused by temporary radiation damage, induced by the observed high electron flux. These electrons are primarily emitted in the decay of unwanted implantation of Tl ions, created by surface ionization. Because of the lower mass resolving power and the higher transmission yields of GPS, the amount of implanted Tl and thus the rate of emitted electrons is severely higher in this run as compared to the IS466-III experiment at HRS.

Evidence for the overwhelming contamination of isobaric Tl isotopes is found in the available γ spectra from run IS466-III, shown in Figure 4.1. However, the Q_β value for Tl isotopes with mass numbers $194 \leq A \leq 202$ is always at least 12 MeV smaller than the calculated B_f of the corresponding beta-decay daughter [41, 94]. The βDF branching ratio of these nuclei is therefore considered to be negligible and will thus not contribute to the FF spectra.
Below, the experimental data are further discussed for each isotope separately.

4.2.1 ^{194}At

The presence of ^{194}At in the HRS α spectra at mass 194, shown in Figure 4.2, is verified by the observation of α-decay lines from the daughter products ^{190}Bi and ^{194}Po. At least three alpha peaks, observed in both GPS and HRS spectra, are ascribed to the α decay of ^{194}At. The peak positions were established, by fitting the α data from the IS466-III run, at 7045(5), 7099(5) and 7153(5) keV. The assignment of these α lines is supported by the absence of α signals with energies between 7000 and 7500 keV in the HRS spectra of Si 3 and 4,

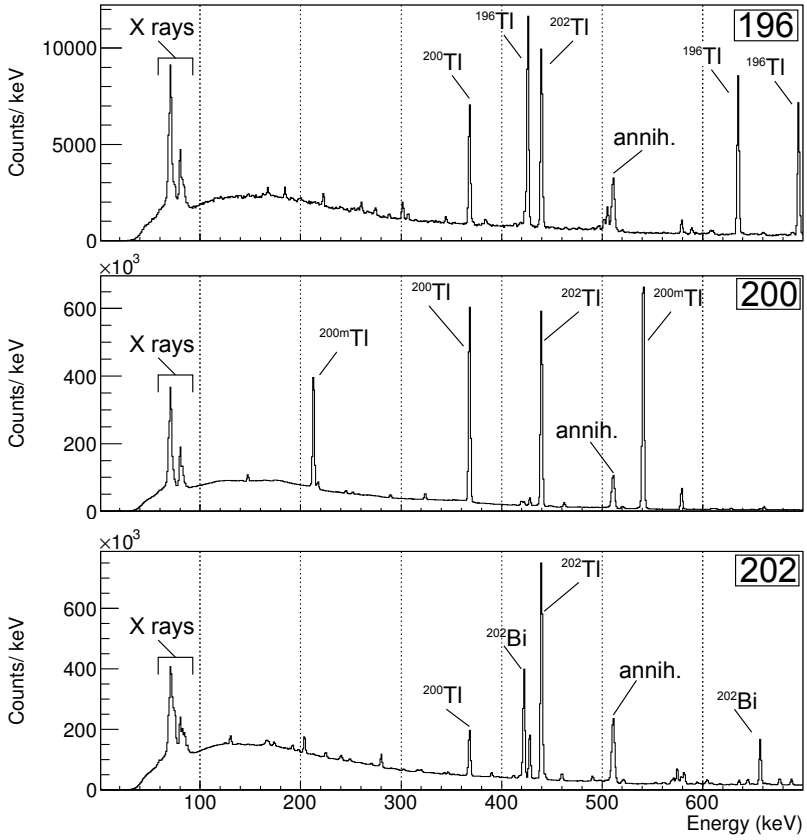

Figure 4.1: Gamma spectra recorded by detector Ge 1 during the IS466-III run when measuring at masses 196,200 and 202. The most prominent lines were identified as originating from Tl contaminants. The presence of non-isobaric Tl in the spectra is due to earlier measurements on other masses. In the case of ^{200}Tl, also a short-living (34 ms) isomeric state was implanted in the carbon foil. Therefore, γ rays emitted in the internal decay of this state are also observed in the spectra at mass 200. Also γ photons followed by the β^+/EC decay of ^{202}Bi were detected. As indicated in Table 4.1, no γ spectra at mass 194 were recorded.

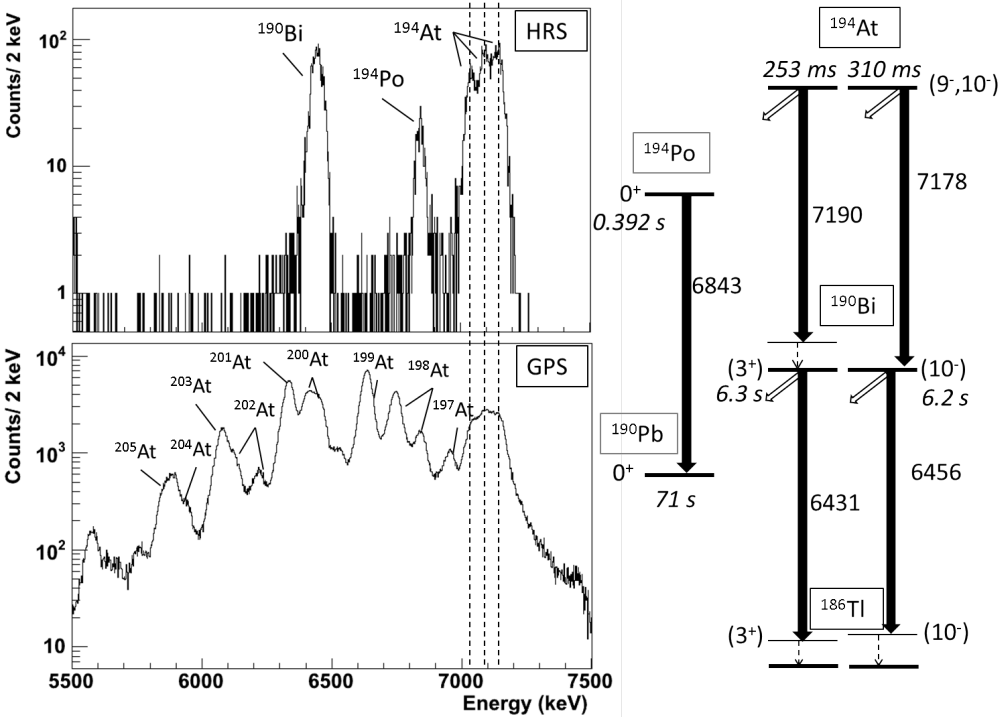

Figure 4.2: Alpha spectra recorded by detector Si 2, corresponding to measurements on ^{194}At. The one on the top shows data taken during the IS466-III experiment at HRS and includes mainly α decay lines of ^{194}At and its daughter products. The lower spectrum, recorded in the IS534 run at GPS, shows significant contamination of other At isotopes. The main α lines of ^{195}At at 6.95 and 7.07 MeV and of ^{196}At at 7.05 MeV are however not observed, but could be obscured by the α peaks corresponding to ^{194,197}At. A simplified decay scheme of ^{194}At with the main α decay lines and their energies (in keV), as found in literature [99, 100], is also given. Solid black arrows represent α decay, while hollow arrows indicate β decay. More details are provided in the main text.

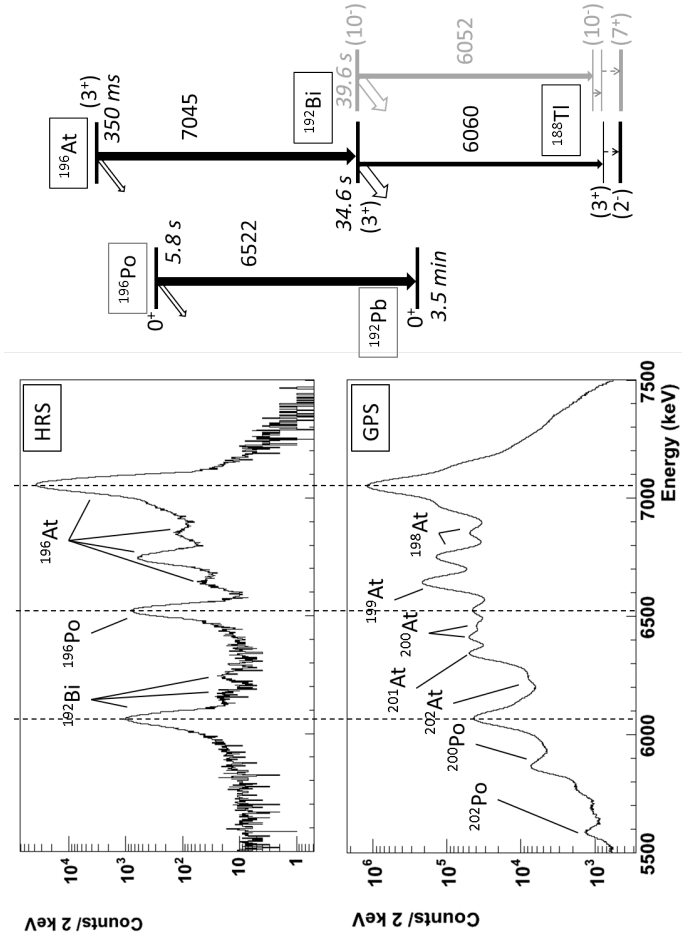

Figure 4.3: Similar to Figure 4.2, but corresponding to ^{196}At. α-decay data were extracted from [50] and [100]. The part in grey is used to indicate that the α decay of the high-spin isomeric level in ^{192}Bi was not observed (see main text).

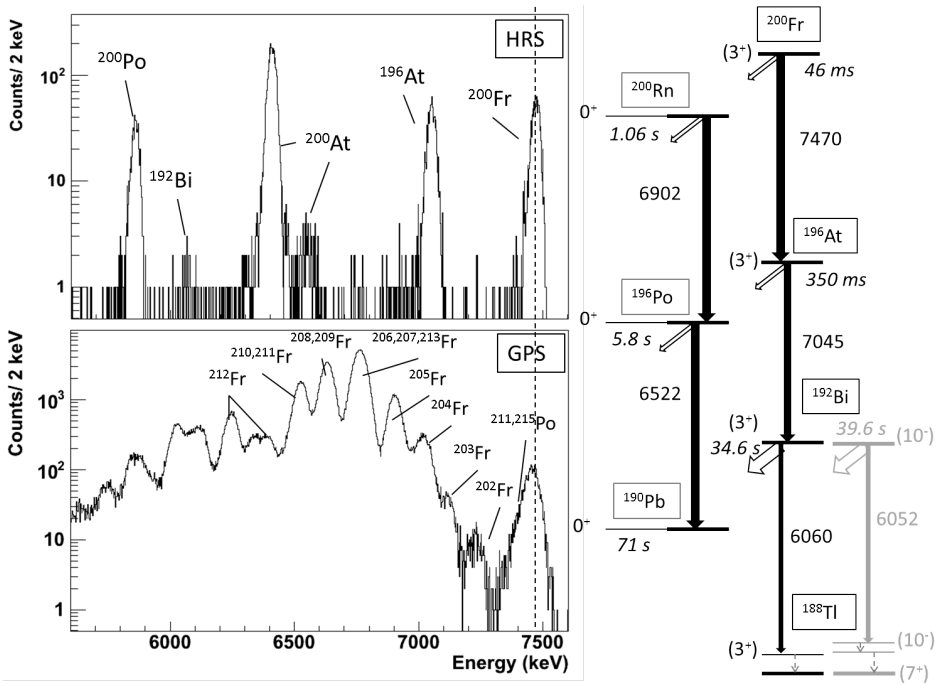

Figure 4.4: Similar to Figure 4.2, but corresponding to ^{200}Fr. α-decay data were extracted from [50] and [100]. The part in grey is used to indicate that the α decay of the high-spin isomeric level in ^{192}Bi was not observed (see main text).

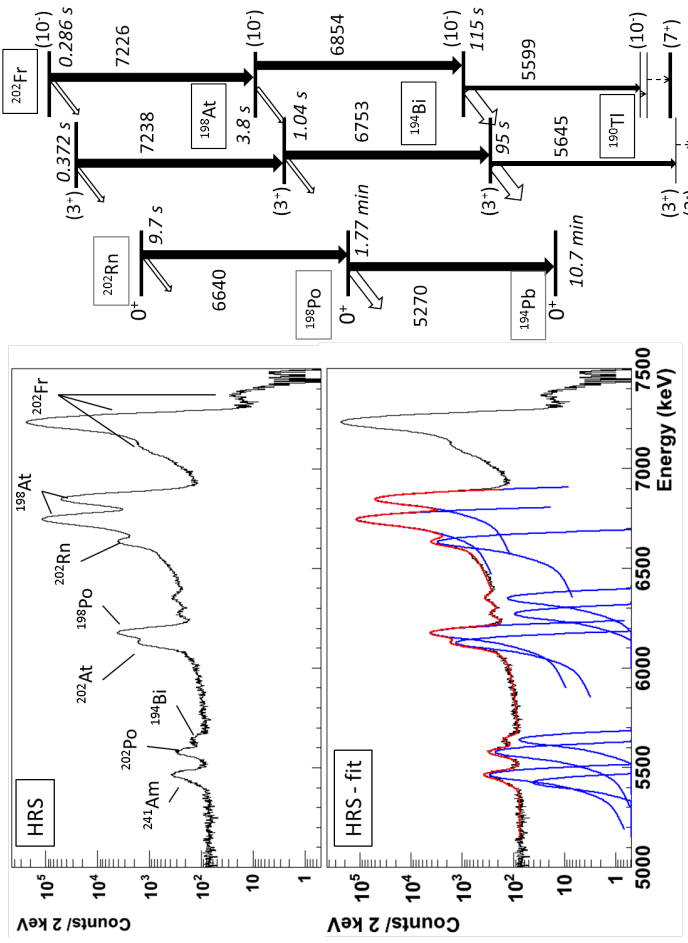

Figure 4.5: (In color) Similar to Figure 4.2, but corresponding to ^{202}Fr. Since data on ^{202}Fr were absent during the IS534 run, only the alpha spectrum recorded during IS466-III is shown. The lower panel shows a partial fit of this spectrum, used for a reliable determination of the centroid and peak content of the different α lines.

implying that their source has a half-life below ~ 1 s. These observations show inconsistenties with literature data from [99], where two main α lines at 7178 keV and 7190 keV were observed in the decay of ^{194}At.

The data in [99] also indicate the presence of two isomeric levels in ^{194}At (see also Figure 4.2), with comparable half-lives of 310(8) and 253(10) ms for the high- and low-spin isomer respectively. These values for the half-lives are consistent with the overall timing behavior of the α particles between 7000 and 7500 keV and the FFs in the current data set with respect to the arrival of a proton pulse to ISOLDE.
Evidence for the presence of at least two α-decaying states in ^{194}At is given in Figure 4.6, where energy spectra of Si 2 from the HRS run are shown for different detection times of the α particles with respect to the arrival of a proton pulse. The changes in relative intensities of the 7045, 7099 and 7153 keV suggests that these α particles originate from at least two different isomeric levels in ^{194}At.
This isomeric structure is also reflected in the alpha decay of ^{190}Bi, having a low- and high-spin isomer with main alpha lines at 6429 and 6455 keV (see also Figure 4.2). The presence of both lines in the HRS-based spectrum can be inferred from the ^{190}Bi α peak with a FWHM of 43(2) keV, significantly broader as compared to the ^{194}Po alpha line with a FWHM of 31(3) keV.
A preliminary analysis of the data from the IS534-II ISOLDE run in September 2012, dedicated to laser-spectroscopy measurements of At isotopes, also shows evidence of isomeric states in ^{194}At. In particular, the hyperfine spectrum associated with the 7153 keV α differs significantly from those corresponding to the 7045 or 7099 keV α line from ^{194}At [101]. This observation is in agreement with the difference in timing behavior of the 7153 keV α particles, illustrated in Figure 4.6.

Since the GPS α spectra show evidence for At contamination of other masses, also the presence of ^{196}At is plausible. However, the 7045 keV α particles of this isotope would be obscured by the ^{194}At alpha structure. An upper limit for the total number of detected ^{196}At alphas in Si 2 is determined at 5.6×10^4, thereby assuming that all α particles detected in the 7045 keV line correspond to ^{196}At. Considering the ratio $N_\alpha/N_{\beta DF}$ for ^{196}At in Table 5.1, at most one βDF event of ^{196}At is expected in the FF spectrum corresponding to mass 194. Observed FFs in both experimental campaigns can thus be ascribed uniquely to the βDF of ^{194}At.

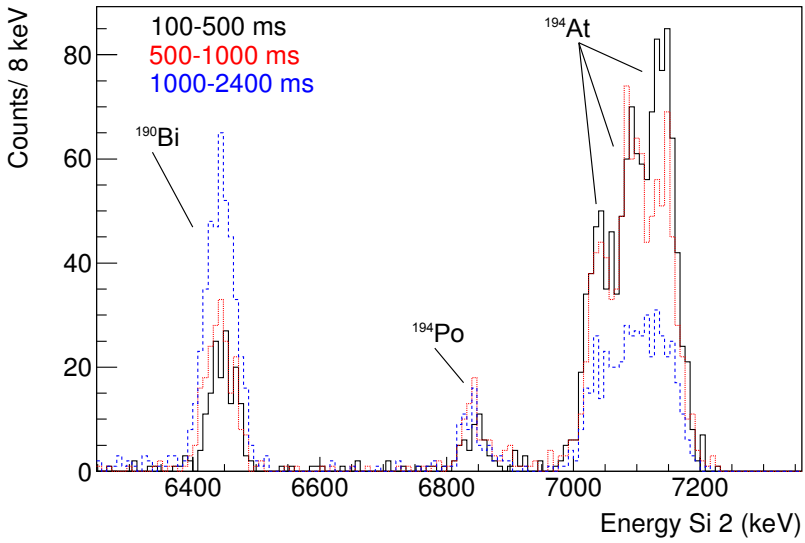

Figure 4.6: (In color) Energy spectra of Si 2 from run IS466-III at HRS, corresponding to different intervals of the detection time of α particles with respect to the arrival of a proton pulse to the ISOLDE target. The black solid, red dotted and blue dashed lines show α particles recorded between respectively 100 and 500, 500 and 1000, 1000 and 2400 ms after the arrival of a proton pulse.

4.2.2 ^{196}At

The HRS-based α spectrum in Figure 4.3 shows clear indications of fine structure in the α decay of ^{196}At. A detailed α-decay study of this isotope is presented in [102, 103]. Reference [102] demonstrates that not more than 1.6 % of the α particles emitted in the decay of ^{192}Bi originate from the high-spin isomer. Therefore, taking into account the simplified decay scheme in Figure 4.3, one can conclude that the radioactive ion beam implanted in the detector setup mainly consists of ^{196}At nuclei in the low-spin state.
The experimental data from IS534, using GPS, again suffer from contamination from other masses, as illustrated in Figure 4.3. One should consider the presence of ^{194}At nuclei, of which the corresponding alpha lines are buried in the spectrum of Figure 4.3. Since the βDF branching of ^{194}At is about two orders of magnitude higher as compared to ^{196}At, even a relatively small amount of ^{194}At nuclei could contaminate the FF spectra. Therefore, a quantitative estimate of this cross-contamination is needed. The discussion in subsection 4.2.1 shows that at most 5.6×10^3 α's, or on average 1.7 α/s, originating from ^{196}At are observed

in the GPS-based α-decay spectrum of mass 194. A comparison to the listed α rates in Table 4.2 thus shows that the implantation rate of ^{196}At reduces by at least a factor of 180 when changing the mass settings of the GPS from 196 to 194 amu. By considering the asymmetry in the tails of the mass peaks, illustrated in Figure 3.6, the transmittance of ^{194}At ions is diminished with at least the same factor when changing the mass from 194 to 196 amu. The data in Table 4.2 show that the corresponding FF rate in Si 2 from the βDF of ^{194}At should thus be less than 0.15 FF/h, or 2.8 % of the total number of observed FFs in Si 2. In conclusion, the FF spectra taken at mass 196 are considered reasonably pure, although a limited admixture of FFs from the βDF of ^{194}At cannot be excluded ($< 2.8\,\%$).

4.2.3 ^{200}Fr

The HRS-based α spectrum at $A = 200$ consists of ^{200}Fr and its daughter products (^{196}At and ^{192}Bi), see Figure 4.4. Furthermore, isobaric contamination of ^{200}At, possibly produced via electron impact ionization close to the extraction electrodes, is identified. In addition, no evidence for the presence of another α-decaying state in ^{200}Fr is found. It is thus assumed that only the low-spin state is produced. Note that ^{196}At, having a significant βDF branch as well, is produced as a daughter product of ^{200}Fr. However, tables 4.1 and 4.2 show that the observed ratio of the α to fission rate in ^{200}Fr is more than two orders of magnitude smaller than for ^{196}At (see also Table 5.1). All observed FFs in the HRS run are thus ascribed to the βDF of ^{200}Fr.

In contrast to the relatively pure HRS-based spectrum, an overwhelming contamination of other Fr isotopes is found in the GPS-based spectrum (Figure 4.4). Due to the fairly high energy of its emitted α particles though, ^{200}Fr remains discernible in the spectrum. Nonetheless, a significant amount of contamination from ^{211,215}Po, originating as daughter products from ^{211,223}Fr, with α energies close to the main α line at 7.47 MeV, was identified. This contamination was revealed by a comparison of detected α spectra recorded in Si 2 (implantation) and Si 4 (decay), as shown in Figure 4.7. The fraction of ^{211,215}Po α particles in the main ^{200}Fr was estimated by comparing the integrals in decay and implantation Si detectors at 20 %.

In addition, the amount of contamination from ^{202}Fr in Figure 4.4 is too small to observe any corresponding βDF events. Therefore, although only a limited amount of FFs were observed, they are all originating from the βDF of ^{200}Fr.

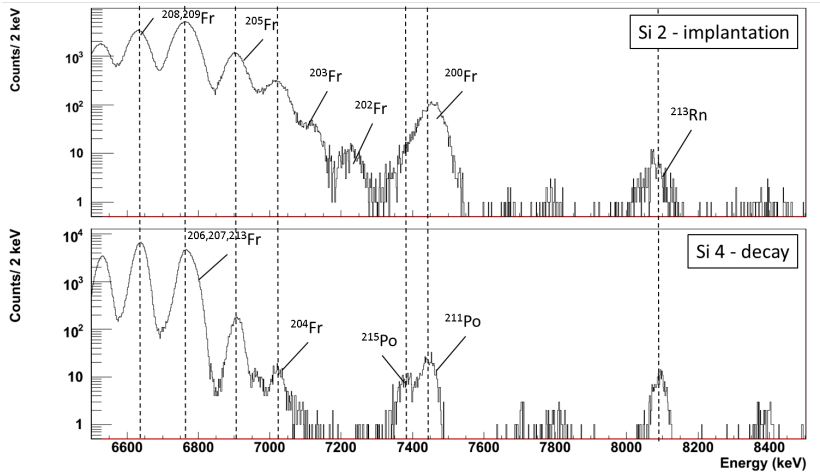

Figure 4.7: A comparison of measured α spectra of Si 2 and Si 4 at mass 200 during the IS534 run. Observed α lines in the decay detector reveal the presence of ^{211,215}Po α-decay lines at energies close to 7.4 MeV, which is close to the energy of the main ^{200}Fr α peak.

4.2.4 ^{202}Fr

All available data on mass 202 are taken using HRS, providing relatively pure α spectra, mainly consisting of α lines from ^{202}Fr and its daughter products. The observed FFs can thus only originate from the βDF of ^{202}Fr. Similar to the case of ^{194}At, two long living isomers are reported in the case of ^{202}Fr. The main α lines of both isomers in ^{202}Fr have similar energies, as depicted in Figure 4.5. This isomeric structure thus only becomes apparent in the decay of ^{198}At. By comparing the contents of the 6753 and 6854 keV α lines, the ratio of low-spin over high- spin isomer in ^{202}Fr is estimated to be 2.4. This estimation is based on the assumption that the α-branching ratios of both isomers in ^{202}Fr are equal. The same assumption was made concerning the α-branching ratios of the isomeric and ground state of ^{198}At.
The observed α peaks at 5.48 MeV arise from a weak ^{241}Am α-calibration source inside the vacuum chamber. In addition, previously unknown fine structure in the α decay of ^{202}Fr is observed. An extensive analysis of the ^{202}Fr-^{198}At-^{194}Bi α-decay chain is presented in a forthcoming publication [104].

4.3 Experimental determination of $P_{\beta\mathrm{DF}}$ and $T_{1/2\mathrm{p},\beta\mathrm{DF}}$

The probability for βDF, $P_{\beta\mathrm{DF}}$, is defined in equation 2.14 as the ratio between the number of fission events $N_{\beta\mathrm{DF}}$ and the number of β decays N_β of the parent nucleus:

$$P_{\beta\mathrm{DF}} = \frac{N_{\beta\mathrm{DF}}}{N_\beta}. \tag{4.1}$$

Since both FF are emitted back-to-back, almost all fission events observed in Si 1 were also simultaneously recorded in Si 2. Therefore, only the βDF events in Si 2 were considered. The number of β-decays N_β is determined by

$$N_\beta = \frac{N^{\mathrm{obs}}_{\alpha,\mathrm{D}}}{b_{\alpha,\mathrm{D}}\epsilon_{\mathrm{Si2}}}, \tag{4.2}$$

where $N^{\mathrm{obs}}_{\alpha,\mathrm{D}}$ is the number of observed α decays of the daughter, created after β decay of the precursor, in Si 2. $b_{\alpha,\mathrm{D}}$ denotes the α-branching ratio of the daughter nucleus and ϵ_{Si2} the absolute detection efficiency of silicon detector Si 2. If the half-life of the daughter is comparable to the length of a measurement cycle (see also Figure 3.12), $N^{\mathrm{obs}}_{\alpha,\mathrm{D}}$ should be corrected for α decays after turning the wheel of the windmill system (see further). In summary, $P_{\beta\mathrm{DF}}$ is found by using the relation

$$P_{\beta\mathrm{DF}} = \frac{\epsilon_{\mathrm{Si2}} N^{\mathrm{obs}}_{\mathrm{FF}} b_{\alpha,\mathrm{D}}}{2\epsilon_{\mathrm{Si2}} N^{\mathrm{obs}}_{\alpha,\mathrm{D}}} = \frac{N^{\mathrm{obs}}_{\mathrm{FF}} b_{\alpha,\mathrm{D}}}{2N^{\mathrm{obs}}_{\alpha,\mathrm{D}}}, \tag{4.3}$$

whereby $N^{\mathrm{obs}}_{\mathrm{FF}}$ is the number of observed FFs in Si 2. Since two FFs are emitted in each βDF event, the detection efficiency for fission events is twice as large as compared to α decays. An extra factor of 2 is thus inserted in the denominator of equation 4.3.
Because of the large amount of impurities in the GPS data (run IS534), a direct extraction of $N^{\mathrm{obs}}_{\alpha,\mathrm{D}}$ is impossible. Therefore, the β-branching ratio of the parent nucleus, $b_{\beta,\mathrm{P}}$, was first extracted from the HRS data (run IS466-III) via the relation

$$b_{\beta,\mathrm{P}} = \frac{(N^{\mathrm{obs}}_{\alpha,\mathrm{D}}/b_{\alpha,\mathrm{D}})}{(N^{\mathrm{obs}}_{\alpha,\mathrm{D}}/b_{\alpha,\mathrm{D}}) + N^{\mathrm{obs}}_{\alpha,\mathrm{P}}}, \tag{4.4}$$

where $N^{\mathrm{obs}}_{\alpha,\mathrm{P}}$ denotes the amount of observed α decays from the parent nucleus. The value for $P_{\beta\mathrm{DF}}$ can then be determined from the GPS data using

$$P_{\beta\mathrm{DF}} = \frac{N^{\mathrm{obs}}_{\mathrm{FF}}(1 - b_{\beta,\mathrm{P}})}{2N^{\mathrm{obs}}_{\alpha,\mathrm{P}} b_{\beta,\mathrm{P}}}. \tag{4.5}$$

Since both ground and isomeric states of ^{194}At and ^{202}Fr are produced, only an overall $P_{\beta\mathrm{DF}}$ value could be extracted at this stage.
In the determination of $b_{\beta,\mathrm{P}}$ or N_β, several systematic effects need consideration. For example, the quantity $N^{\mathrm{obs}}_{\alpha,\mathrm{D}}$ should be corrected for possible direct implantation of daughter nuclei. In the case of ^{196}At, this contribution was determined by comparing laser ON and OFF measurements. It was found that 0.1 % of the observed ^{196}Po α counts originates from direct production (see also [102]). Similar measurements in the case of ^{194}At are unfortunately absent. Since ^{200,202}Fr ions are created by surface ionization (see section 3.1), the direct implantation of ^{200,202}Rn ions remains undetermined.
In the case of ^{200}Fr, only an upper limit for b_β could be determined, because the ^{200}Rn α decay line at 6.902(3) keV [1] was not observed in the α spectra (see Figure 4.4). As a result, a lower limit for $P_{\beta\mathrm{DF}}$ is given.
The longer half-life of the daughters, as compared to the parents, implies that some of these nuclei only decay after or during the movement of the WM. Therefore, also the α signals from Si 3, having approximately the same detection efficiency as Si 2, were considered. In addition, corrections were applied for decay losses during the rotation of the wheel and for a possible difference in detection efficiencies between Si 2 and Si 3, see also [47, 102].

The majority of the above mentioned systematic effects are absent if the partial half-life for βDF $T_{1/2\mathrm{p},\beta\mathrm{DF}}$ (see equation 2.15), instead of $P_{\beta\mathrm{DF}}$, is considered. The total number of decayed precursor nuclei $N_{\mathrm{dec,tot}}$ can be determined by

$$N_{\mathrm{dec,tot}} = \frac{N^{\mathrm{obs}}_{\alpha,\mathrm{P}}}{\epsilon_{\mathrm{Si2}}(1 - b_{\beta,\mathrm{P}})}. \tag{4.6}$$

Equation 2.15 can now be re-written into

$$T_{1/2\mathrm{p},\beta\mathrm{DF}} = T_{1/2}\frac{2\epsilon_{\mathrm{Si2}}N^{\mathrm{obs}}_{\alpha,P}}{\epsilon_{\mathrm{Si2}}N^{\mathrm{obs}}_{\mathrm{FF}}(1 - b_{\beta,\mathrm{P}})} = T_{1/2}\frac{2N^{\mathrm{obs}}_{\alpha,P}}{N^{\mathrm{obs}}_{\mathrm{FF}}(1 - b_{\beta,\mathrm{P}})}. \tag{4.7}$$

In the βDF precursors considered here, the α-decay channel is dominant ($b_{\beta,P}$<10%), and $T_{1/2\mathrm{p},\beta\mathrm{DF}}$ is approximated by

$$T_{1/2\mathrm{p},\beta\mathrm{DF}} = T_{1/2}\frac{2N^{\mathrm{obs}}_{\alpha,P}}{N^{\mathrm{obs}}_{\mathrm{FF}}}, \tag{4.8}$$

whereby both $N^{\mathrm{obs}}_{\alpha,\mathrm{P}}$ and $N^{\mathrm{obs}}_{\mathrm{FF}}$ are determined from the α spectrum of Si 2. The factor of 2 in the numerator was introduced to account for the difference in detection efficiency for α particles and double-folded fission events.
From equation 4.7, it follows that $b_\beta = x\%$ induces a relative shift on $T_{1/2\mathrm{p},\beta\mathrm{DF}}$ values, extracted by equation 4.8, of $1/(1-x) \simeq x\,\%$. The systematic error caused by taking $b_{\beta,\mathrm{P}} \simeq 0$ is thus significantly smaller than the error induced by statistics or the uncertainty on the employed (average) half-life, listed in Table 4.3. Also the systematic effect caused by contaminating α particles of ^{211,215}Po in the ^{200}Fr case was found considerably smaller than the error bar given in Table 4.3 (see also section 4.2.3).
When both ground and isomeric states are present, as in the case of ^{194}At and ^{202}Fr, only an overall value can be extracted. The half-life $T'_{1/2}$ is therefore approximated by the unweighted average

$$T'_{1/2} = \frac{T_{1/2,\mathrm{g}} + T_{1/2,\mathrm{m}}}{2}, \tag{4.9}$$

with $T_{1/2,\mathrm{g}}$ and $T_{1/2,\mathrm{m}}$ denoting respectively the half-life of ground and isomeric state reported in literature [50, 99]. The corresponding uncertainty $\Delta T'_{1/2}$ is conservatively taken as

$$\Delta T'_{1/2} = \frac{|T_{1/2,\mathrm{g}} - T_{1/2,\mathrm{m}}|}{2}. \tag{4.10}$$

The extracted $b_{\beta,\mathrm{P}}$, $P_{\beta\mathrm{DF}}$ and $T_{1/2\mathrm{p},\beta\mathrm{DF}}$ values for ^{194,196}At and ^{200,202}Fr using data from both the IS466 - III and IS534 run are given in Table 4.3. An extensive systematic investigation of $T_{1/2\mathrm{p},\beta\mathrm{DF}}$ values across the nuclear chart is discussed in chapter 6.

4.4 Calibration of silicon detectors for fission fragments

4.4.1 Pulse height defect

Silicon detectors exhibit several advantages for the detection of FFs. They have an excellent energy resolution (below $\sim 1\,\%$), an intrinsic efficiency of nearly

Table 4.3: Summary of $P_{\beta\mathrm{DF}}$ and $T_{1/2\mathrm{p},\beta\mathrm{DF}}$ of ^{200,202}Fr and ^{194,196}At as measured in runs IS466-III (HRS) and IS534 (GPS). $T_{1/2\mathrm{p},\beta\mathrm{DF}}$ are determined by using equation 4.8. Furthermore, β- branching ratios $b_{\beta,P}$ of these βDF precursors were also extracted from data in run IS466-III. The half-life $T_{1/2}$ and the α - branching ratio of the β - decay daughter nucleus $b_{\alpha,\mathrm{D}}$ are also listed. Since two longer-living isomers of both ^{194}At and ^{202}Fr were produced, only overall values for $b_{\alpha,\mathrm{D}}$, $P_{\beta\mathrm{DF}}$ and $T_{1/2\mathrm{p},\beta\mathrm{DF}}$ could be extracted. In addition, in these cases the average half-life $T'_{1/2}$, given by equation 4.9, is listed.

			IS466 - III			IS534	
nucleus	$T_{1/2}$ or $T_{1/2}$ (s)	$b_{\alpha,\mathrm{D}}$ (lit)	$b_{\beta,\mathrm{P}}$	$P_{\beta\mathrm{DF}}$	$T_{1/2\mathrm{p},\beta\mathrm{DF}}$	$P_{\beta\mathrm{DF}}$	$T_{1/2\mathrm{p},\beta\mathrm{DF}}$
^{194}At	$0.28(3)^{a}$	$0.93(7)^{b}$	0.081(6)	$6^{+5}_{-3} \times 10^{-3}$	$6^{+6}_{-3} \times 10^{2}$	$6.7(7) \times 10^{-3}$	$4.8(6) \times 10^{2}$
^{196}At	$0.358(5)^{c}$	$0.94(5)^{b}$	0.026(1)	$10^{+6}_{-4} \times 10^{-5}$	$1.4^{+0.7}_{-0.5} \times 10^{5}$	$9(1) \times 10^{-5}$	$1.5(2) \times 10^{5}$
^{200}Fr	$0.049(4)^{b}$	$0.86^{+14}_{-4}{}^{d}$	$< 0.021(4)$	$< 19(16) \times 10^{-2}$	$12^{+70}_{-9} \times 10^{2}$	$> 3.1(17) \times 10^{-2}$	$7^{+6}_{-3} \times 10$
^{202}Fr	$0.33(4)^{e}$	$0.78(8)^{b}$	0.024(2)	$3.0(5) \times 10^{-5}$	$4.5(8) \times 10^{4}$	-	-

[a] Value extracted according to equation 4.9 by using evaluated experimental data from [99].
[b] Evaluated experimental data from [1].
[c] value from [103]
[d] Branching ratio from [105].
[e] Value extracted according to equation 4.9 by using experimental data from [50].

100% and a compact size. However, it is observed that a heavy particle induces a smaller signal as compared to a light particle, such as a proton or α particle, of the same energy. This effect is generally known as the pulse height defect [106], and can result in a $5 - 10\,\%$ decrease of the signal of typical FFs [107] (see also appendix A). Since the Si detector energy was calibrated during the ISOLDE campaigns on βDF by using α sources, an appropriate treatment of this phenomenon is needed.
Analysis has shown that three separate phenomena contribute to this defect [108, 109]. The first contributor is the energy loss of the ion in the dead layer, or entrance window, of the detector, including the metallic electrode and a possibly non-depleted layer of Si. Due to the relatively high stopping power of heavy ions, their fractional energy loss in this layer is higher as compared to α particles. Secondly, nuclear collisions, which increase with decreasing ion velocity, diminish the amount of electron-hole pairs created per unit of deposited energy. Finally, a high electron-hole recombination rate is expected in the dense plasma created around a heavy-ion track.
A variety of semi-empirical descriptions were proposed to express the pulse height defect as a function of incoming ion mass, proton number Z, and energy E (see e.g. [107, 109–113]). Schmitt and co-workers proposed a simple calibration method for FFs, whereby a linear dependence between the observed pulse height X and energy is assumed for each FF mass number M [110]. Furthermore, the slope and offset of the calibration line are assumed to vary linearly with increasing mass. For the detector calibration the formula

$$E = (A + A'M)X + B + B'M \tag{4.11}$$

is employed.
This calibration method was later verified for a specific type of surface barrier detectors at the Lohengrin spectrometer in ILL, where fission fragments from the $^{235}\mathrm{U}(n, f)$ reaction are both energy and mass separated [29]. It was found that this procedure is accurate to within 250 keV for typical FF masses and energies.
A similar experiment was conducted for detectors used in the βDF studies at ISOLDE, including one annular and two circular surface barrier and two PIPS detectors. These results confirmed the validity of equation 4.11 for FFs, with typical energies of $20 - 100\,\mathrm{MeV}$ and masses of $80 - 136$, to within an accuracy level of $\sim 200\,\mathrm{keV}$. Since the α particles from ternary fission and a $^{241}\mathrm{Am}$ source were recorded as well, also the calibration equation for α particles

$$E_\alpha = aX + b \tag{4.12}$$

Table 4.4: Calibration constants A/a, A'/a, B and B' extracted from the ILL campaign for both Si1 and Si2, which are used in experiments IS466-III and IS534.

	Si 1 (43-051F)	Si 2 (47-038D)
A/a	0.923(9)	0.917(9)
A'/a	$9.6(9) \times 10^{-4}$	$1.00(9) \times 10^{-3}$
B (MeV)	-0.57(43)	-0.29(49)
B'(MeV)	$0.036(4) \times 10^{-2}$	$0.032(5) \times 10^{-2}$

was deduced. The constants A and A' in equation 4.11 can therefore be normalized for the electronic gain by considering A/a and A'/a. It was assumed that the offset $B + B'M$ solely depends on detector characteristics, such as the dead-layer thickness. Equation 4.11 can thus be fully determined for the detectors calibrated in ILL if the α calibration equation 4.12 is known. In Table 4.4, the values for A/a, A'/a, B and B' are quoted for detectors Si 1 and Si 2, with serial numbers 43-051F and 47-038D respectively, employed in both runs IS466-III and IS534. A more detailed description of this calibration procedure and the observed pulse height defect is provided in appendix A.

4.4.2 Extraction of fragment energies and masses

A precise determination of both FF energies and masses with a silicon detector is possible by using mass and linear momentum conservation laws, which requires a simultaneous detection of both fragments in two separate detectors. Further details on the calibration procedure described below can be found in [47, 114]. A set of four equations is created by combining the mass and momentum conservation laws and the calibration equation 4.11 for both detectors:

$$\begin{cases} E_i & = (A_i + A'_i M_i) X_i + B_i + B'_i M_i, \qquad (i = 1, 2) \\ M_1^* E_1^* & = M_2^* E_2^*, \\ M_1^* + M_2^* & = A_f. \end{cases} \tag{4.13}$$

The subscripts 1 or 2 correspond to Si 1 or Si 2 respectively. The values E_i, M_i denote energies and masses *after*, while the starred variables M_i^*, E_i^* indicate corresponding quantities *before* prompt neutrons are emitted. Note that neutron emission is thus implicitly assumed to happen post-scission, after the fragments are fully accelerated, since the conservation of linear momentum in equation

4.13 would otherwise be invalid. The mass number of the fissioning nucleus is denoted by A_f. The conversion between pre- and post-neutron emission quantities is given by

$$\begin{cases} E_i^* & = E_i + \Delta E_{i,\nu} + \Delta E_{i,\mathrm{int}} \\ \Delta E_{i,\mathrm{int}} & = \Delta E_{i,\mathrm{cf}} + \Delta E_{i,\mathrm{angle}} + \Delta E_{i,\mathrm{cal}}, \\ M_i^* & = M_i + \nu_i, \end{cases} \tag{4.14}$$

where ν_i denotes the number of emitted neutrons per fragment and $\Delta E_{i,\nu}$ the corresponding energy correction to the FF energy. In addition, the value $\Delta E_{i,\mathrm{int}}$ is related to several systematic effects in the detection system. All of these corrections are further discussed below.

The quantity $\Delta E_{i,\mathrm{cf}}$ in equation 4.14 denotes the energy loss of ions in the carbon foil, with a total thickness of 88 nm. As an example, an estimate of $\Delta E_{i,\mathrm{cf}}$ for the βDF fragments of ^{202}Fr is provided here by performing different simulations with the program SRIM [115]. A similar analysis on the βDF fragments of ^{194,196}At [102] or ^{180}Tl yielded nearly identical results [116]. First, the implantation of precursor nuclei in the foil was simulated by assuming a mono- energetic beam of 30 keV impinging on a pure carbon layer. In addition, a beam spot size of 6 mm with uniform density was assumed. As illustrated in figure 4.8, the mean penetration depth equals 18 nm for ^{202}Fr, which is about $1/5^{th}$ of the total foil thickness. Straggling induces a position spread of 2 nm.

In a second step, these simulated implantation points were used as starting point for mono-energetic fission fragments with a certain mass M and atomic number Z, which are emitted in a random direction. The energy loss due to the carbon foil was then estimated for each emitted fragment. Finally, by taking the geometry of the detection setup into account, the FFs which would impinge on either Si 1 or 2 were selected. Note that the set of equations 4.13 only considers FFs detected in coincidence. Therefore, a simulated FF, which would hit one of the detectors, but for which the corresponding fragment will miss the other detector, is rejected in the analysis.
Typical FF masses and energies emitted in the βDF of ^{202}Fr were determined from a preliminary analysis. Atomic numbers were estimated by considering similar N/Z ratios in fragments and fissioning nuclei. As an example, Figures 4.9 and 4.10 show the energy loss of mono-energetic 84 MeV ^{88}Rb and 65 MeV ^{113}In nuclei impinging on detectors Si 1 and 2 respectively. The value of $\Delta E_{i,\mathrm{cf}}$ thus seems to depend only marginally on the FF properties. The values of $\Delta E_{i,cf}$ and their respective error bars were taken as the weighted average and spread of the distributions shown in Figures 4.9 and 4.10. In summary, the energy corrections $\Delta E_{1,cf} = 0.3(1)\,\mathrm{MeV}$ and $\Delta E_{2,cf} = 1.1(2)\,\mathrm{MeV}$ were chosen

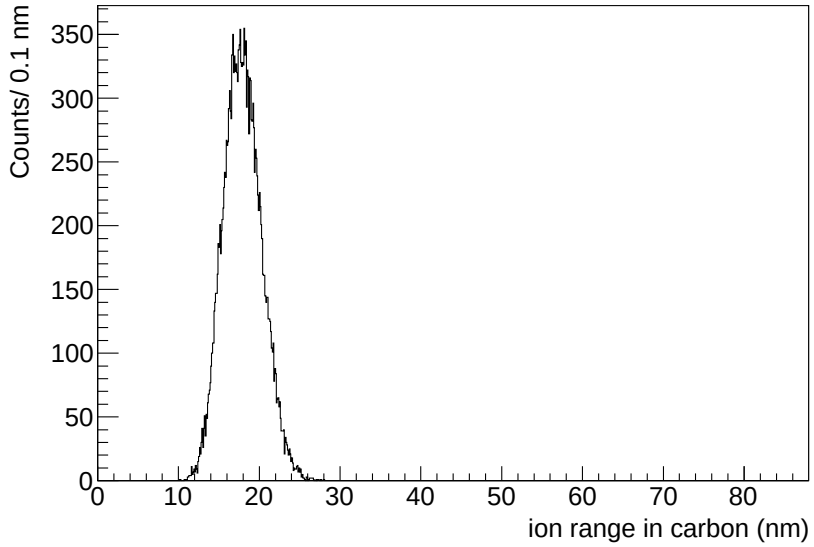

Figure 4.8: Implantation depth profile simulated with SRIM [115], using a sample of more than 20 000 30 keV ^{202}Fr ions impinging perpendicular on a carbon layer. The range of the X axis of 88 nm was chosen to match the total thickness of the carbon foils mounted on the WM detection system.

for equation 4.14, irrespective of the FF properties. The correction related to Si 2, $\Delta E_{2,cf}$, is higher due to the fact that FFs have to travel a longer distance through the C foil as compared to the FFs impinging on Si 1 (see also Figure 4.8).

The energy loss in the dead layer of the detector is incorporated in equation 4.11 for ions with perpendicular incidence on the detector surface. However, most of the detected fission fragments hit the detector under a grazing angle. Therefore, the correction term $\Delta E_{i,\mathrm{angle}}$ was introduced in equation 4.14 to incorporate this effect. Figure 4.11 shows the distribution of incident angles corresponding to simulated FF emitted from a uniformly distributed source with a diameter of 6 mm, such as the ones used to determine $\Delta E_{i,\mathrm{cf}}$. In principle, if the thickness of the dead layer is known, a dedicated analysis using SRIM would thus allow to determine $\Delta E_{i,\mathrm{angle}}$. However, the orientation of incoming ions with respect to the detector electric field lines is expected to alter the electron-hole recombination rate inside the silicon crystal as well [106], which would thus influence the pulse height magnitude. Therefore, dedicated measurements were performed at ILL during which the detector was tilted at an angle of

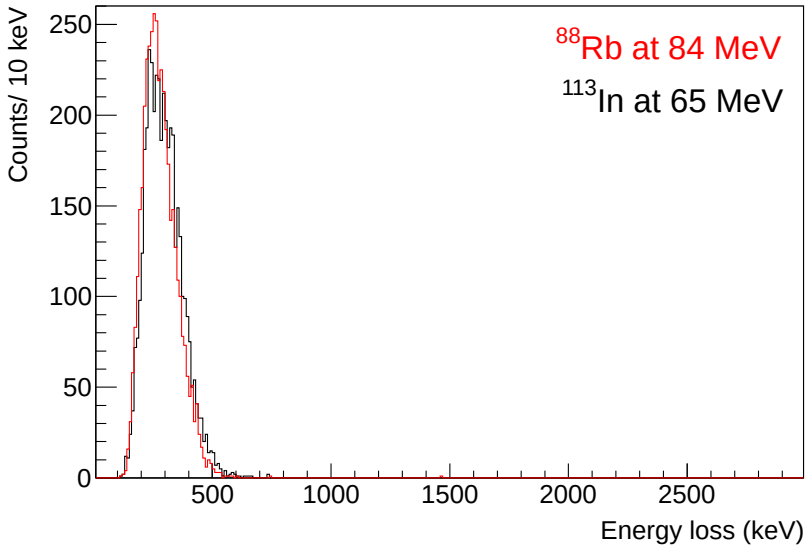

Figure 4.9: (In color) Simulated energy loss of typical FFs from the βDF of ^{202}Fr impinging on the front annular detector Si 1, assuming the implantation profile from Figure 4.8. The red curve corresponds to the energy loss of ^{88}Rb isotopes emitted with an energy of 84 MeV, while the black curve shows the energy loss for ^{133}In nuclei having an initial energy of 65 MeV.

approximately 45°, which is very close to the mean incident angle of 44° in the distribution shown in Figure 4.11. These data showed that changing the grazing incidence angle induces a mean shift of 0.3 MeV for surface-barrier type detectors (see also Appendix A). Therefore, the mean energy loss associated with the grazing angle of incident ions was estimated $\Delta E_{i,\mathrm{angle}} = 0.3$ MeV. Since the FFs may reach the detector at various angles, see Figure 4.11, the uncertainty on this value was taken as large as the shift.

Since the FFs detected in the ISOLDE campaigns have a different N/Z ratio as compared to the FFs from the ^{235}U(n, f) used for the detector calibration, a systematic error on the calibration constants $\Delta E_{i,\mathrm{cal}}$ might be present. For example the electron-hole recombination effect is strongly dependent on the electronic stopping power of the incoming particle, because this quantity is proportional to the plasma density around a particle track [107, 109, 113]. According to the Bethe-Bloch equation, the energy loss in a material primarily depends on the velocity and effective charge of the ions, in addition to the mass and energy which are considered in equation 4.11. Therefore, a rising

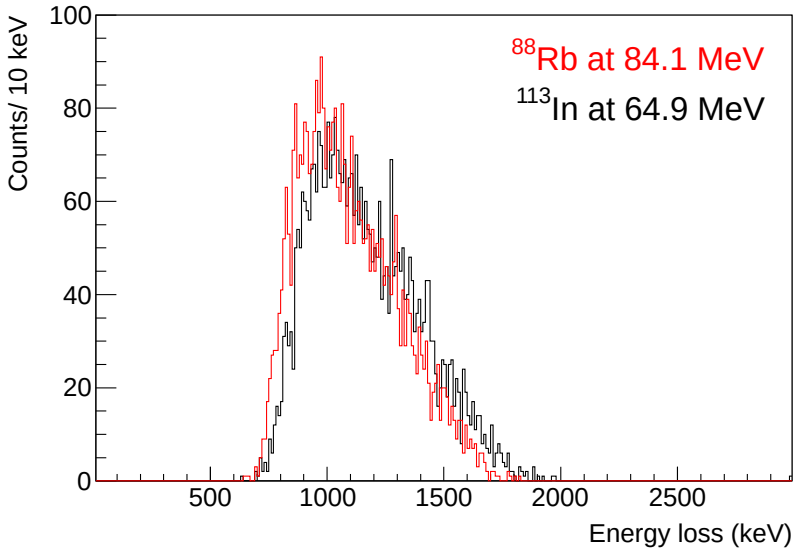

Figure 4.10: (In color) Similar to Figure 4.9, but now for the backside detector Si 2.

dependence of the pulse height defect with increasing Z can be expected (see e.g. [109, 113]).
$\Delta E_{i,\mathrm{cal}}$ can be estimated by looking at variations in the pulse height defect for rising mass and Z. Typical β-delayed FFs from neutron deficient At and Fr isotopes are, for example, $^{90}_{39}$Y, $^{100}_{43}$Tc or $^{105}_{46}$Pd, thereby assuming a conservation of the N/Z ratio of the fissioning parent nucleus. The most probable FFs from ^{235}U(n, f) with the same mass are $^{90}_{36}$Kr, $^{100}_{40}$Zr and $^{105}_{42}$Mo [107]. FFs detected during the ISOLDE campaigns thus have 3-4 protons more as compared to FFs from the ^{235}U(n, f) calibration source. Data from the ILL calibration measurements showed that the pulse height defect rises by $\sim$ 1 MeV when increasing simultaneously the FF mass by 10 amu and the most probable Z by 4 units. The correction on the calibration $\Delta E_{i,\mathrm{cal}}$ is therefore assumed to be smaller than 1 MeV. A shift of 0.5 MeV with ditto error bar is thus applied: $\Delta E_{i,\mathrm{cal}} = 0.5(5)$ MeV.
The obtained systematic shifts $\Delta E_{i,\mathrm{cf}}$, $\Delta E_{i,\mathrm{angle}}$ and $\Delta E_{i,\mathrm{cal}}$ were then added linearly, according to equation 4.14, to obtain the total energy correction, $\Delta E_{i,\mathrm{int}}$, listed in table 4.5.

In the estimation of the energy correction $\Delta E_{i,\nu}$ for prompt-neutron emission, two generally accepted assumptions were made. First, as indicated before,

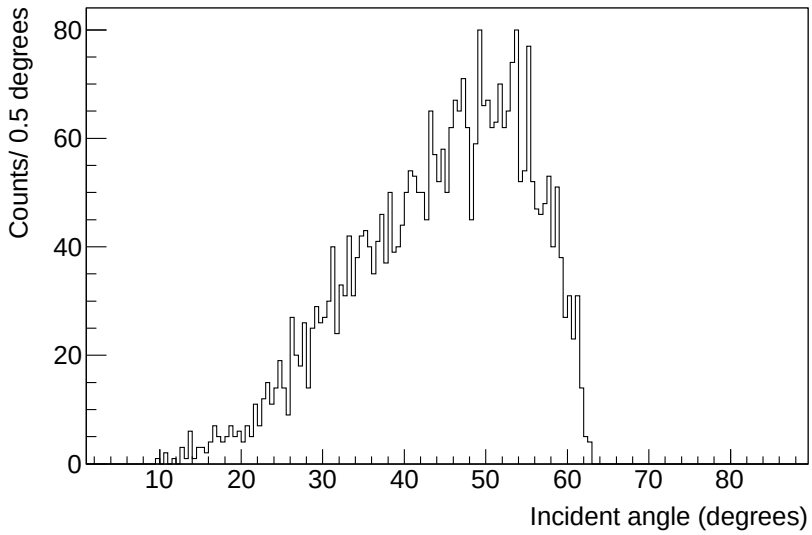

Figure 4.11: Simulated angular distribution of FFs emitted from a uniformly distributed source with a diameter of 6 mm. This distribution corresponds to the incident angles of fission events for which both fragments impinge on Si 1 or 2 of the WM system.

Table 4.5: The different components, with their respective error bars, contributing to the systematic shift of FF energy $\Delta E_{i,\mathrm{int}}$ in equation 4.14.

	Si 1 (43-051F)	Si 2 (47-038D)
$\Delta E_{i,\mathrm{cf}}$ (MeV)	0.3(1)	1.1(2)
$\Delta E_{i,\mathrm{angle}}$ (MeV)	0.3(3)	0.3(3)
$\Delta E_{i,\mathrm{cal}}$ (MeV)	0.5(5)	0.5(5)
$\Delta E_{i,\mathrm{int}}$ (MeV)	1.1(6)	1.9(6)

neutrons are assumed to happen post-scission when fragments are fully accelerated. In addition, it is assumed that neutrons will be emitted isotropically in the center of mass, meaning that the average velocity of the FFs is unaffected. $\Delta E_{i,\nu}$ can then be estimated as

$$\Delta E_{i,\nu} \simeq \frac{\nu_i}{M_i^*} E_i^*. \tag{4.15}$$

The system 4.13 can now be rewritten, by introducing the variable $F_i = 1 - \frac{\nu_i}{M_i^*}$, as

$$\begin{cases} E_i^* & = (\frac{a_i}{F_i} + a_i' M_i^*) X_i + \frac{b_i}{F_i} + b_i' M_i^* + \frac{\Delta E_{i,sys}}{F_i}, \\ M_1^* E_1^* & = M_2^* E_2^*, \\ M_1^* + M_2^* & = A_f. \end{cases} \tag{4.16}$$

It follows that M_1^* is the solution of the quadratic equation

$$\alpha {M_1^*}^2 + \beta M_1^* + \gamma = 0, \tag{4.17}$$

with

$$\begin{aligned} \alpha &= A_1' + B_1' - A_2' X_2 - B_2', \\ \beta &= \tfrac{A_1}{F_1} X_1 + \tfrac{B_1}{F_1} + \tfrac{A_2}{F_2} X_2 + B_2 + 2 A_f A_2' X_2 + 2 A_f B_2' + \tfrac{\Delta E_{1,sys}}{F_1} + \tfrac{\Delta E_{2,sys}}{F_2}, \\ \gamma &= -A_f (\tfrac{A_2}{F_2} X_2 + A_2' A_f X_2 + \tfrac{B_2}{F_2} + A_f B_2' + \tfrac{\Delta E_{2,sys}}{F_2}). \end{aligned} \tag{4.18}$$

In the first iteration step, F_i is set to unity, thus assuming no neutron emission. When $\nu_i > 0$, F_i can be estimated from M_i^* calculated in step one. Then, equation 4.17 is solved iteratively, until a stable solution is found.

Chapter 5

Fission-fragment mass and energy distributions

This chapter presents the β-delayed fission properties of ^{200,202}Fr and ^{194,196}At, extracted by using the analysis methods presented in chapter 4. In addition, these results have been interpreted in the framework of two contemporary fission models, namely the macroscopic-microscopic finite-range liquid-drop model (FRLDM) and the self-consistent approach employing the Gogny D1S energy density functional. This research has been presented in a peer-reviewed article [74]:

Paper I : L. Ghys, A.N. Andreyev, M. Huyse, P. Van Duppen et al., "Evolution of fission-fragment mass distributions in the neutron-deficient lead region", *Physical Review C*, vol. 90, p. 041301(R), 2014.

This publication is also given in section 5.1 with slight modifications to its lay-out in order to match the style of this thesis. Also, some subtitles were introduced to improve the readability. My main contribution to this paper is the analysis and interpretation of the experimental results, based on fruitful discussions with several co-authors. I was also the corresponding author, responsible for drafting and submitting the article. The theoretical mass distributions presented in Figure 5.1 were provided by P. Möller and J. Randrup from the Lawrence Berkeley national laboratory (Berkeley, USA). The calculated potential-energy surface in Figure 5.4 was provided by M. Warda from the Marie Curie-Sklodowska university.

Section 5.2 elaborates further on the possibility for prompt-neutron emission based on energy considerations.

5.1 β-delayed fission properties of neutron-deficient At and Fr isotopes (Paper I)

PHYSICAL REVIEW C **90**, 041301(R) (2014)

Evolution of fission-fragment mass distributions in the neutron-deficient lead region

L. Ghys[1,2], A. N. Andreyev[3,4,5], M. Huyse[1], P. Van Duppen[1], S. Sels[1], B. Andel[6], S. Antalic[6], A. Barzakh[7], L. Capponi[5], T. E. Cocolios[8,9], X. Derkx[5,10], H. De Witte[1], J. Elseviers[1], D.V. Fedorov[7], V.N. Fedosseev[11], F.P. Hessberger[12,13], Z. Kalaninová[6], U. Köster[14], J.F.W. Lane[5], V. Liberati[5], K.M. Lynch[8,9], B.A. Marsh[11], S. Mitsuoka[4], P. Möller[15], Y. Nagame[4], K. Nishio[4], S. Ota[4], D. Pauwels[2], R.D. Page[16], L. Popescu[2], D. Radulov[1], M.M. Rajabali[1], J. Randrup[17], E. Rapisarda[8], S. Rothe[11,18], K. Sandhu[5], M.D. Seliverstov[1,3,5,7], A.M. Sjödin[11], V.L. Truesdale[3], C. Van Beveren[1], P. Van den Bergh[1], Y. Wakabayashi[4,19] and M. Warda[20]

[1] *KU Leuven, Instituut voor Kern- en Stralingsfysica, 3001 Leuven, Belgium*
[2] *Belgian Nuclear Research Center SCK•CEN, Boeretang 200, B-2400 Mol, Belgium*
[3] *Department of Physics, University of York, York, YO10 5DD, United Kingdom*
[4] *Advanced Science Research Center, Japan Atomic Energy Agency, Tokai-Mura, Naka-gun, Ibaraki, 319-1195, Japan*
[5] *School of Engineering, University of the West of Scotland, Paisley, PA1 2BE, United Kingdom*
[6] *Departement of Nuclear Physics and Biophysics, Comenius University, 84248 Bratislava, Slovakia*
[7] *Petersburg Nuclear Physics Institute, NRC Kurchatov Institute, Gatchina 188300, Russia*
[8] *PH Departement, CERN, CH-1211 Geneve 23, Switzerland*
[9] *School of Physics and Astronomy, The University of Manchester, M13 9PL, United Kingdom*
[10] *LPC, ENSICAEN, Université de Caen Basse Normandie, CNRS/IN2P3-ENSI, F-14050, France*
[11] *EN Departement, CERN, CH-1211 Geneve 23, Switzerland*
[12] *Gesellschaft für Schwerionenforschung, Planckstrasse 1, D-64291 Darmstadt, Germany*
[13] *Helmholtz Institut Mainz, 55099 Mainz, Germany*

[14] *Institut Laue Langevin, 71 avenue des Martyrs, F-38042 Grenoble Cedex 9, France*
[15] *Theoretical Division, Los Alamos National Laboratory, Los Alamos, New Mexico 87545, USA*
[16] *Departement of Physics, Oliver Lodge Laboratory, University of Liverpool, Liverpool L69 7ZE, United Kingdom*
[17] *Nuclear Science Division, Lawrence Berkeley National Laboratory, Berkeley, California 94720, USA*
[18] *Institut für Physik, Johannes Gutenberg-Universität Mainz, D-55128 Mainz, Germany*
[19] *RIKEN Nishina Center for Accelerator Based Science, Wako, Saitama 351 0198, Japan*
[20] *Institute of Physics, Marie Curie-Sklodowska University, pl. M. Curie-Sklodowskiej 1, 20-031 Lublin, Poland*
(Received 27 June 2014; revised manuscript 29 August 2014, published 15 October 2014)

DOI: 10.1103/PhysRevC.90.041301
PACS numbers: 21.10.Re,23.20.Lv,27.70.+q,29.38.-c

Abstract

Low-energy β-delayed fission of ^{194,196}At and ^{200,202}Fr was studied in detail at the mass separator ISOLDE at CERN. The fission-fragment mass distributions of daughter nuclei ^{194,196}Po and ^{202}Rn indicate a triple-humped structure, marking the transition between asymmetric fission of ^{178,180}Hg and symmetric fission in the light Ra-Rn nuclei. Comparison with the macroscopic-microscopic finite-range liquid-drop model and the self-consistent approach employing the Gogny D1S energy density functional yields discrepancies. This demonstrates once more the need of dynamical fission calculations, as for both models the potential-energy surfaces lack pronounced structures, in contrast to the actinide region.

Introduction

Nuclear fission, the division of a heavy atomic nucleus into predominantly two parts, continues to provide new and unexpected features in spite of a long history of intensive theoretical and experimental studies [2, 14, 22, 30, 42, 79, 117]. The fission process is not only important for several applications, such as energy production and radiopharmacology, but also has a direct impact on the

understanding of the fission recycling process in r-process nucleosynthesis [7, 8]. Therefore, a description of the fission process with reliable predictive power is needed, in particular for low-energy fission where the fission-fragment (FF) mass distributions are strongly sensitive to microscopic effects [22]. Mass distributions (MDs) are usually predominantly symmetric or asymmetric with the yields exhibiting a single peak or two distinct peaks, respectively. However, in several cases a mixture of two modes was observed [30]. Experimental observables characterizing various fission modes are the width of the MD peak(s), the position of these peaks in asymmetric mass division and total kinetic energy (TKE) of the FFs.

The dominance of asymmetric fission in most of the actinide region beyond A = 226 up to about ^{256}Fm was attributed to strong microscopic effects of the heavier FF, near the doubly-magic ^{132}Sn [22, 57, 118]. However, nuclei such as ^{258}Fm and ^{259,260}Md exhibit complex MDs, each with a narrow and a broad symmetric component with a higher and lower TKE, respectively. This phenomenon is called bimodal fission [51, 52, 119, 120]. Competition between symmetric and asymmetric fission, corresponding to respectively lower and higher TKE and resulting in a triple-humped MD has been reported around ^{226}Th [53–55]. These observations strongly support the hypothesis that nuclei may fission through several independent fission modes corresponding to different pre-scission shapes and fission paths in a multidimensional potential-energy landscape, referred to in literature as multimodal or multichannel fission [22, 30, 53–57].

In the pre-actinide region, predominantly symmetric FF mass distributions were measured. A few relevant cases for the present discussion (see also Fig. 5.1) are ^{195}Au, ^{198}Hg and ^{208,210}Po, studied by means of charged-particle induced reactions [36–38] and ^{204,206,208}Rn studied via electromagnetically (EM)-induced fission [5, 6].

In contrast to this, recent β-delayed fission experiments have established a new region of asymmetry around nuclei ^{178,180}Hg [3, 4, 47], which in fission divide into neutron-deficient fragments with most probable mass numbers around $A_{\mathrm{L}} \sim 80$ and $A_{\mathrm{H}} \sim 100$. The mechanism behind the asymmetric MD is different from that in the uranium region, since strong shell effects in the respective FFs are absent in the neutron-deficient lead region. Several theoretical models reproduced this observation [60–62, 121].

Extensive calculations of the FF mass yields by use of the recently developed

Brownian Metropolis shape-motion treatment [122] are shown in Fig. 5.1. These calculations reproduced well the observed mass asymmetry of ^{178,180}Hg and symmetry of ^{204,206,208}Rn and predict a smooth transition in between.

We report in this paper on the fission properties of neutron-deficient isotopes ^{194,196}Po and ^{202}Rn situated between these two regions, which were measured through the βDF process.
In this two-step process a precursor nuclide undergoes β decay to excited states near the top of the fission barrier in the daughter nucleus, which then may fission. The excitation energy of the fissionning daughter is limited by the Q_β value, thus typically in the region between 3 to 11 MeV. Presently, 26 βDF cases are known in the region between thallium and mendelevium [42]. Prior to this work, βDF of ^{196}At was experimentally observed in Dubna [45, 46]. In addition, recent experiments at SHIP have identified βDF of ^{192,194}At [49]. However, due to the detection methods employed, FF mass distributions remained undetermined in all three cases.

In this letter, we report on the first identification of βDF in ^{200,202}Fr and on dedicated measurements of ^{194,196}At, situated in a region where fission has scarcely been studied before. Calculations in Fig. 5.1 show predominantly asymmetric fission with a gradually decreasing mass split when moving from ^{178,180}Hg towards ^{204,206}Rn nuclei. In contrast to these theoretical predictions, the new results indicate complex multimodal fission of ^{194,196}Po.

Experimental details

The measurements were carried out in ISOLDE (CERN) [90], where astatine and francium isotopes are formed in spallation reactions via the bombardment of a 50 g/cm^2 thick UC_x target by 1.4 GeV protons. Surface ionization of francium or laser-ionization of astatine [92] in the ion source of ISOLDE are employed for the respective element selection. After extraction, acceleration to 30 keV and mass separation the isotopically-purified beam is transported to the 'Windmill' detection setup, described in detail in [3, 47, 123]. There, the ion beam is implanted into one of ten 20 μg/cm^2 thick carbon foils, which are mounted on a rotatable wheel. FFs, as well as α particles, are recorded by two silicon detectors of 300 μm thickness, further denoted by Si1 and Si2, placed on either side of the foil. The detection efficiency for single FFs is $\sim$ 51 %, while double-fold FFs are recorded with $\sim$ 21 % efficiency [47]. After $\sim$ 40 s, the irradiated foil is turned between another pair of silicon detectors, where longer-living daughter activity can be detected. Meanwhile, implantation and

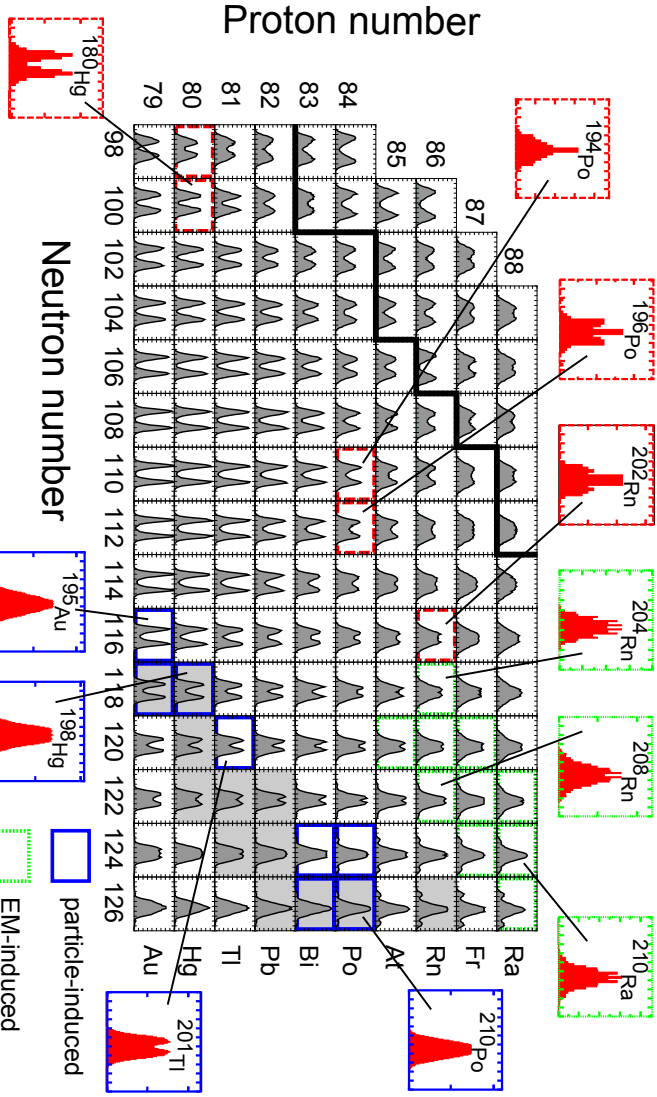

Figure 5.1: (In color) Calculated MDs (gray), with fission-fragment masses on the horizontal and their relative yields on the vertical axis, for even-N neutron-deficient isotopes between gold and radium at excitation energies slightly above the theoretical fission-barrier heights $B_{\mathrm{f,th}}$ [71]. The calculated yields are compared with selected experimental MDs (red) from particle-induced [36, 37], β-delayed ([3, 4], this work) and EM-induced fission [5, 6]. The border of the lightest known isotopes is shown by the thick solid line, β-stable nuclei are shown on a gray background.

measurements continue on a fresh foil. A high-purity germanium detector was installed in close vicinity to the implantation point for γ detection (see Fig. 1 from [3]).

The experimental campaign consisted of two parts, a summary of acquired statistics is given in Table 5.1. The first part, carried out at the High-Resolution Separator (HRS) in 2011, was mainly dedicated to βDF of ^{202}Fr. Daughter activities and the thallium isobaric beam contaminant, produced by surface ionization, were observed in the α or γ spectra respectively. Because of a low Q_{EC} value (Tl) [94] and high fission barrier (Hg) [71], βDF is severely hindered for ^{202}Tl [42]. The observed FFs are thus uniquely ascribed to the βDF of ^{202}Fr. A similar reasoning applies for the βDF measurements of ^{194,196}At and ^{200}Fr.

The data for ^{194,196}At and ^{200}Fr were mainly acquired at the General Purpose Separator (GPS) in 2012, although a limited number of βDF events for these nuclei was observed at the HRS, see Table 5.1. The full energy spectrum after 35 hours of data collection on ^{196}At at the GPS is shown in Fig. 5.2. Electrons/positrons, α particles and fission fragments ($30 - 90$ MeV energy) are marked in the spectrum.

The technique described in [47] allowed to deduce a βDF probability of $P_{\beta\mathrm{DF}} = 9(1) \times 10^{-5}$ for ^{196}At and a lower limit at $P_{\beta\mathrm{DF}} > 3.1(17) \times 10^{-2}$ for ^{200}Fr (in agreement with [50], where only a single event was observed). A detailed discussion on the α decay of ^{196}At is given in a forthcoming paper [103]. In the cases of ^{194}At and ^{202}Fr, $P_{\beta\mathrm{DF}}$ remains undetermined at this stage since two states (the ground state and an isomer) with unknown β branching ratios and similar half-lives are known [49, 99, 124]. Although the excitation energy of the isomeric states are most likely less then a few hundreds keV, their difference in spin and parity with respect to the ground state may result in dissimilar βDF properties. These intriguing cases will be further studied at the RILIS [125] or CRIS [126, 127] setup at ISOLDE, where the production of each state might be selectively enhanced by exploiting differences in the atomic hyperfine structure.

Results

The Si detectors were individually calibrated with mass- and energy-separated beams at the FF separator LOHENGRIN at ILL, enabling a precise conversion of the measured energy distributions in MDs [47]. A possible emission of prompt neutrons would cause a shift in TKE of about 0.7 MeV per emitted neutron [47]. However, total energy-balance considerations limit the number of

Table 5.1: Summary of βDF runs giving the total number of detected single ('S') and double-fold ('D') FFs, the ratio of α to βDF decays recorded in the same detector, corrected for the detection-efficiency difference between α particles and double-fold fission events, and the total measurement time.

data set	S FFs	D FFs	$N_\alpha/N_{\beta\mathrm{df}}$	time
^{194}At - HRS	8	3	$2.0^{+17}_{-8} \times 10^3$	1h 13m
^{194}At - GPS	385	106	$1.7(1) \times 10^3$	9h 11m
^{196}At - HRS	14	5	$3.9^{+19}_{-12} \times 10^5$	5h 25m
^{196}At - GPS	273	68	$4.3(5) \times 10^5$	35h 7m
^{200}Fr - HRS	1	0	$2.5^{+123}_{-17} \times 10^3$	21h 34m
^{200}Fr - GPS	7	2	$1.5^{+12}_{-6} \times 10^3$	20h 18m
^{202}Fr - HRS	115	43	$1.4(2) \times 10^4$	43h 59m

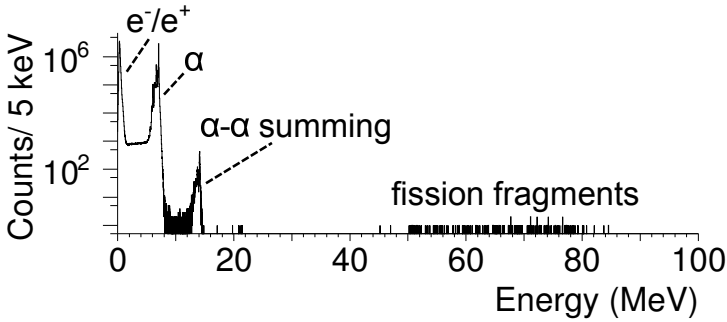

Figure 5.2: The full-range energy spectrum for ^{196}At taken in the measurements at the GPS.

prompt neutrons to a maximum of two per fission event in studied nuclei. Since this emission can only marginally influence MDs, the corresponding energy correction was neglected.

The resulting mass and energy distributions of coincident FFs after βDF of ^{194,196}At and ^{202}Fr are shown in Fig. 5.3 including, as a reference, the data from ^{180}Tl [47]. Because of low statistics, ^{200}Fr is excluded. For ^{180}Tl, asymmetric fission was clearly observed as a double-humped structure in the two-dimensional Si1-Si2 energy plot at the top, showing the energies of two coincident fission fragments. The single Gaussian-like TKE distribution, depicted in the middle row, indicates that for the βDF of ^{180}Tl one fission mode dominates. Finally, the deduced clearly asymmetric MD is depicted in black at the bottom.
In contrast to ^{180}Tl, a single broad hump is seen in the 2D energy distribution for

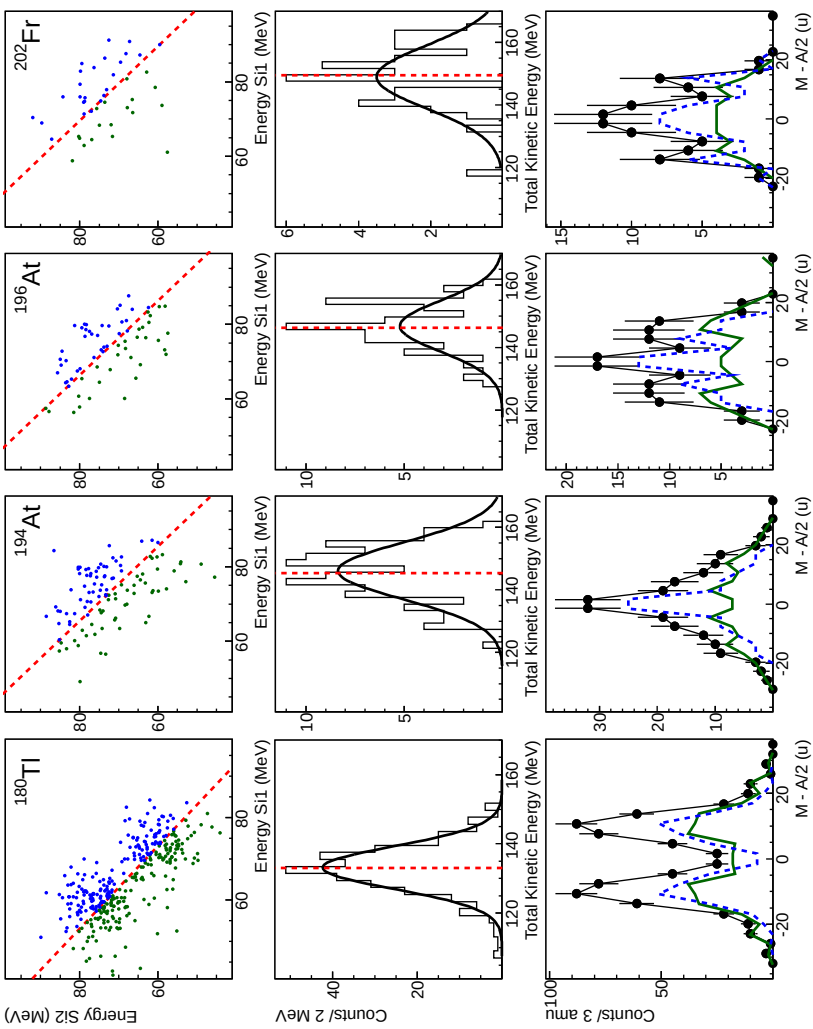

Figure 5.3: (In color) Summary plot of the 2D energy distribution of coincident FFs in 2 silicon detectors (top), total kinetic energy (middle) and mass distributions (bottom) of investigated nuclei. The green and blue curves represent data below and above the average TKE given in Table 5.2. Details are given in the main text.

Table 5.2: Characteristic parameters of TKE and mass distributions shown in Fig. 5.3, when assuming no prompt neutrons are emitted. The mean value $\overline{\mathrm{TKE}}$, standard deviation σ of the respective Gaussian fits are given, as well as corresponding statistical errors. In addition, the lower mass number A_{L} and the relative mass split $\Delta A/A_{\mathrm{tot}}$ of asymmetric fission are listed.

	$\overline{\mathrm{TKE}}$ (MeV)	σ (MeV)	A_{L}	$\Delta A/A_{\mathrm{tot}}$
$^{180}\mathrm{Tl} \xrightarrow{\beta} {}^{180}\mathrm{Hg}$ (ff)[a]	133.1(3)	6.1(3)	80(1)	0.11(1)
$^{194}\mathrm{At} \xrightarrow{\beta} {}^{194}\mathrm{Po}$ (ff)	146(1)	9.0(13)	-	-
$^{196}\mathrm{At} \xrightarrow{\beta} {}^{196}\mathrm{Po}$ (ff)	147(1)	8.1(15)	88(2)	0.10(2)
$^{202}\mathrm{Fr} \xrightarrow{\beta} {}^{202}\mathrm{Rn}$ (ff)	149(2)	10(3)	89(2)	0.12(2)

[a] data taken from [47]

the βDF of ^{194,196}At and ^{202}Fr. In addition, TKE distributions are significantly broader compared to the ^{180}Tl reference as can be concluded from the standard deviation values, extracted from single Gaussian fits, see Table 5.2. Mass spectra, drawn in black, exhibit a mixture of symmetry with asymmetry.

The indication of triple-humped MDs and width of the extracted TKE suggest the presence of at least two distinct fission modes each having different mass and TKE distributions. This feature was therefore further investigated by discriminating between fission events with high or low TKE, similar to the method described in [51, 52] used to illustrate bimodal fission in the transfermium region.
In Fig. 5.3, MDs of fission events with respectively higher or lower TKE in comparison to a certain threshold energy E_{thres} are shown by respectively the dashed blue and full green line. The value E_{thres} was arbitrarily taken as the mean TKE value listed in Table 5.2 and is indicated by a dashed red line on the TKE distributions and the 2-D energy plots. Remarkably, the ^{194,196}At cases exhibit a narrow symmetric distribution for fragments with higher TKE, while a broader, possibly asymmetric structure is observed for lower TKE. In contrast, this feature is absent in the βDF of ^{180}Tl, in which only one asymmetric fission mode was identified. In the case of ^{202}Fr, statistics prohibit drawing definitive conclusions.
The asymmetry was quantified in Table 5.2 as $\Delta A/A_{\mathrm{tot}}$, where A_{tot} represents the compound-nucleus mass and ΔA the difference between the most probable mass numbers of the observed heavy and light asymmetric FFs, obtained from Gaussian fits to the total mass spectra.

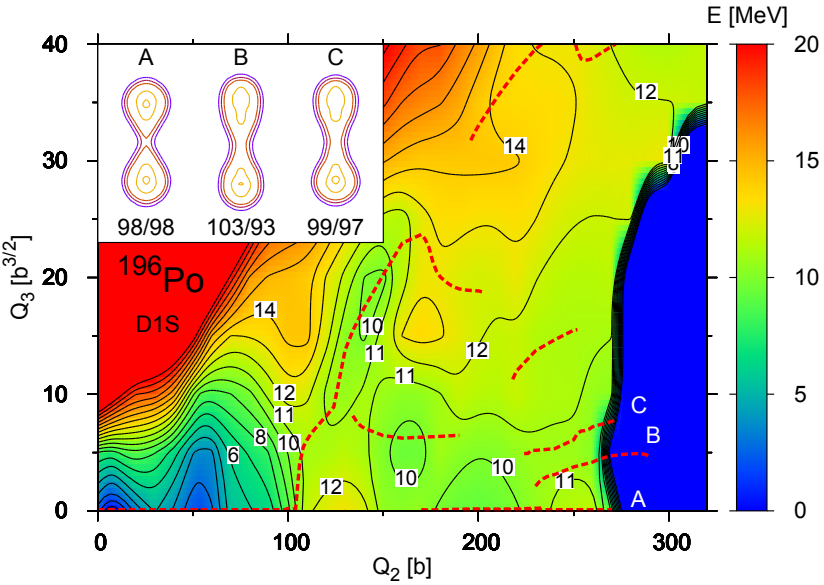

Figure 5.4: (In color) Calculated PES for ^{196}Po from a microscopic HFB theory [61, 128, 129]. Lines of constant energy are plotted every 1 MeV. Dashed lines represent fission paths. Scission-point shapes and corresponding mass ratios for three fission paths A-C are shown in the inset.

Discussion

The data have been compared with two theoretical descriptions. The microscopic HFB theory with Gogny D1S nuclear force [61, 128, 129], see Fig. 5.4, shows a broad and flat plateau in the potential-energy surface (PES) with numerous weakly-pronounced valleys and ridges, not exceeding 2 MeV energy difference, for a wide range of quadrupole (beyond $Q_2 = 100$ b) and octupole deformations. Such a pattern in the PES for ^{196}Po, without well-defined fission valleys, leads to a variety of fission paths possibly giving rise to a mixture of symmetric and asymmetric MD. Ignoring thermal fluctuations, three fission paths with different scission-point shapes can be identified (see inset in Fig. 5.4): one symmetric (A), one with almost symmetric FF masses (C) and one asymmetric (B). Within the current model, the full FF mass distribution as well as the balance between various modes remains however undetermined. Furthermore, in contrast to the actinides where clear valleys in the PES that lead to fission are present, the rather flat PES plateau in this region necessitates the inclusion of dynamic effects in describing the fission process.

The finite-range liquid-drop model (FRLDM) calculations, which show similar PES patterns as compared to the HFB calculations for nuclei in this region [60], were combined with the Brownian shape-motion model in order to calculate FF mass distributions [73, 130]. As shown in Fig. 5.1 and further discussed in [131], there is reasonable agreement between the calculations and most of the experimental data earlier obtained. Also the experimental triple-humped MDs in the transition region between symmetry and asymmetry around ^{226}Th, resulting from a competition between symmetric and asymmetric fission channels, were reproduced with fair accuracy [73, 122]. However, the FRLDM calculations show only one asymmetric fission channel, with a gradual decrease of the mass split, during the transition from distinctly asymmetric in ^{178,180}Hg towards symmetry in the Ra-Rn nuclei. This is in contrast to the experimental findings that show a different mass distribution (see Fig. 5.3) and a constant relative mass split of the asymmetric component between ^{180}Hg and ^{202}Rn (see Table 5.2).

Conclusion

In conclusion, our experimental data for ^{194,196}Po and ^{202}Rn suggest a new region of multimodal fission in the neutron-deficient lead region. Calculations based on modern approaches (FRLDM and HFB) show broad and flat potential-energy surfaces in this region, making it difficult to identify unique fission paths but providing a much better testing ground for the dynamical description of fission, as compared to the actinide region where strong structures in the PES determine the MDs. In addition, the ground and isomeric states in ^{194}At and ^{202}Fr may exhibit different βDF behaviors, both in terms of FF mass distributions and β-delayed fission probabilities. These cases provide a unique experimental way to study the spin and parity dependence of fission and will therefore be further investigated at ISOLDE-CERN using selective laser-ionization techniques [125, 126].

Acknowledgements

We thank the ISOLDE collaboration for providing excellent beams and the GSI Target Group for manufacturing the carbon foils. Also, we express our gratitude to K.-H. Schmidt for providing the files containing measured fission-fragment element distributions in EM-induced fission, shown in Fig. 5.1. A part of this work was done during the Program INT-13-3 'Quantitative Large Amplitude Shape Dynamics: Fission and heavy ion fusion' at the National

Institute for Nuclear Theory in Seattle. This work has been funded by FWO-Vlaanderen (Belgium), by GOA/2010/010 (BOF KU Leuven), by the Interuniversity Attraction Poles Programme initiated by the Belgian Science Policy Office (BriX network P7/12), by the European Commission within the Seventh Framework Programme through I3-ENSAR (contract no. RII3-CT-2010-262010), by a grant from the European Research Council (ERC-2011-AdG-291561-HELIOS), by the Slovak Research and Development Agency (Contract No. APVV-0105-10), by the Office of Nuclear Physics in the U.S. Department of Energy's Office of Science under Contract No. DE-AC02-05CH11231, by the National Nuclear Security Administration of the U.S. Department of Energy at Los Alamos National Laboratory under Contract No. DE-AC52-06NA25396, by the UK Science and Technology Facilities Council (STFC) and by the Reimei Foundation of JAEA.

5.2 Possibility for prompt-neutron emission

As can be inferred from the description of the WM system in chapter 3, neutrons emitted during or after fission cannot be recorded. Nonetheless, as mentioned in section 5.1, an upper limit for the number of prompt neutrons can be estimated from energy considerations. As indicated in section 4.4, prompt-neutron emission is assumed to happen after the formation of both FFs. This decay mode is governed by the strong interaction and can thus be $\sim 3-4$ orders of magnitude faster than γ decay, which is caused by the electromagnetic interaction [22]. The main source of prompt neutrons is supposed to originate from FF with an excitation energy exceeding the neutron-separation energy S_n. In addition, the excitation energy of both fragments is considered equal. The maximum excitation energy E^*_{max} of one FF is thus estimated by

$$E^*_{\mathrm{max}} \simeq \frac{Q_{\mathrm{f}} + Q_\beta - \overline{\mathrm{TKE}}}{2}, \tag{5.1}$$

whereby the Q value associated with the fission decay is given by Q_{f} and is inferred from evaluated atomic masses in [94]. The value Q_β, also taken from [94], concerns the precursor nucleus and is considered an upper limit for the excitation energy of the fissioning β-decay daughter nucleus. In Figure 5.5, the estimated E^*_{max} of FFs after the βDF of ^{194,196}At and ^{202}Fr is compared to the corresponding S_n. The value of $\overline{\mathrm{TKE}}$ is taken from Table 5.2 and the FFs are considered to have a similar N/Z ratio as the nucleus undergoing fission. From Figure 5.6, where E^*_{max} is compared with the two-neutron separation energy S_{2n}, it is apparent that the emission of two prompt neutrons per fragment is highly unlikely. One can therefore conclude that at most one prompt neutron

Table 5.3: Mean TKE values $\overline{\text{TKE}}$ and corresponding width σ for the βDF of ^{194,196}At and ^{202}Fr. $\overline{\text{TKE}}$ and σ have been determined by a single-Gaussian fit on the TKE distribution, such as the ones shown in Figure 5.3 for zero neutrons emitted. All values are given in MeV.

	0 neutrons		1 neutrons		2 neutrons	
precursor	$\overline{\text{TKE}}$	σ	$\overline{\text{TKE}}$	σ	$\overline{\text{TKE}}$	σ
^{194}At	146(1)	9.0(13)	147(1)	8.9(10)	148(1)	10.4(13)
^{196}At	147(1)	8.1(15)	148(2)	9.3(21)	148(1)	9.0(15)
^{202}Fr	149(2)	10(3)	152(2)	9.3(17)	152(3)	13(4)

per fragment can be emitted in the βDF of ^{194,196}At and ^{202}Fr.

The FF mass and energies presented in Figure 5.3 and Table 5.2 can be corrected for prompt-neutron emission by applying the procedure described in section 4.4.2. As indicated before, these corrections have a negligible influence on the MDs shown in Figure 5.3. However, mean TKE values shift by about 0.7 MeV per emitted neutron, see also [47]. Table 5.3 lists the mean and width of the investigated TKE distributions, determined from a single-Gaussian fit, when assuming 0, 1 or 2 neutrons are emitted per βDF fission *event* (thus corresponding to two FFs). Within error bars, the possible emission of prompt neutrons thus has a negligible influence on the extracted TKE distributions.

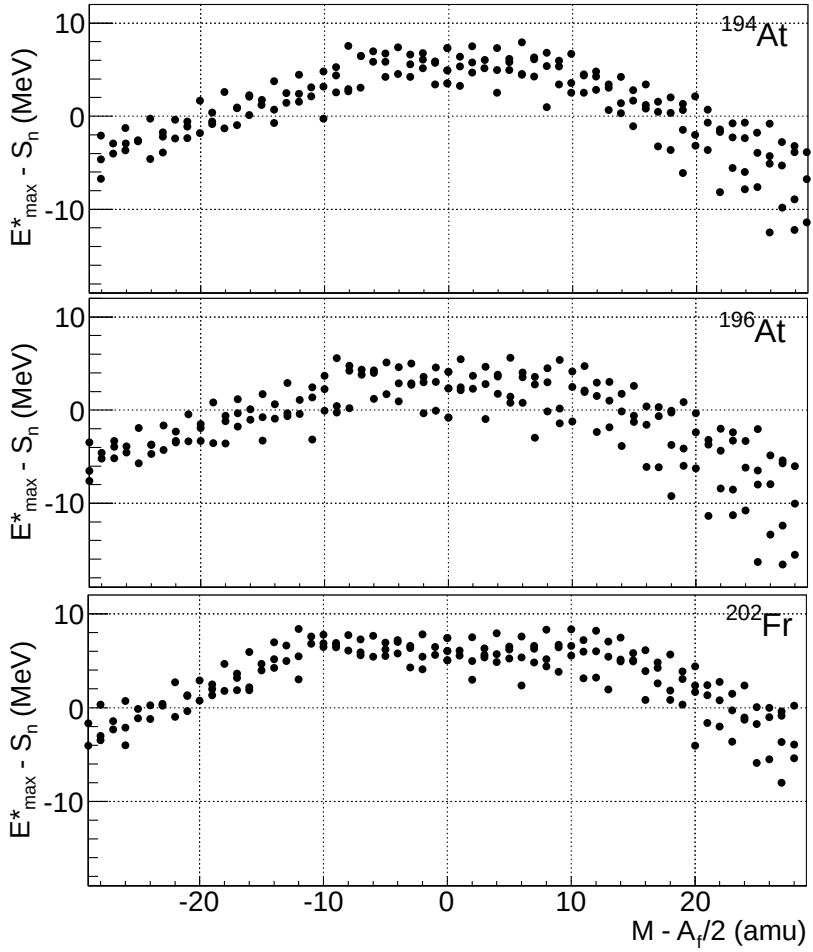

Figure 5.5: Difference of the maximum excitation energy $E^*_{\max}$, estimated from equation 5.1 with the neutron-separation energy S_n of the FFs resulting from the βDF of ^{194,196}At and ^{202}Fr. The X axis gives the mass number M of the resulting FF, subtracted with $A_f/2$, whereby A_f denotes the mass number of the fissioning nucleus. Q_{f}, Q_β and S_n were inferred from the evaluated atomic mass data in [94]. The relative amount of neutrons and protons in the fragments was considered similar to that of the fissioning nucleus. In particular, for the βDF fragments of ^{202}Fr, N/Z values between 1.30 and 1.40 were considered. In the case of ^{194,196}At, N/Z ratios were taken between 1.25 and 1.35.

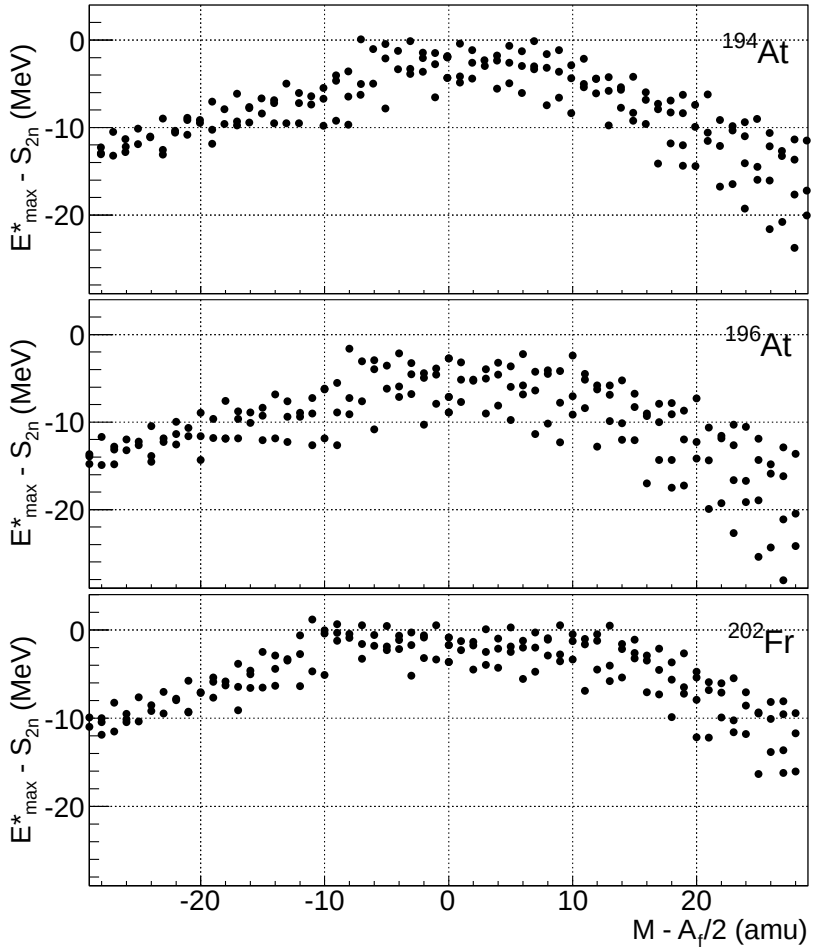

Figure 5.6: Similar to Figure 5.5, but now considering the two-neutron separation energies S_{2n} of the fission fragments.

Chapter 6

Systematic investigation of βDF branching ratios

This chapter presents a phenomenological framework for the description of βDF-branching ratios throughout the nuclear chart. In particular, an exponential dependence of βDF partial half-lives on $(Q_\beta - B_\mathrm{f})$ was derived by making some simple theoretical approximations. Furthermore, a study of data, from both literature as well as this work, demonstrated this simple relation for βDF partial half-lives spanning over 7 orders of magnitude. These findings were presented in a peer-reviewed article [132]:

Paper II : L. Ghys, A.N. Andreyev, S.Antalic, M. Huyse and P. Van Duppen, "Empirical description of β-delayed fission partial half-lives", *Physical Review C*, vol. 91, p. 044314, 2015.

I was in charge of the theoretical analysis and systematic investigation presented in this paper, in close collaboration with the co-authors. As corresponding author for this paper, I was also responsible for drafting and submitting the article. This article is given in section 6.1, although slight modifications were applied in order to match the lay-out, style and page size of this thesis. In particular, Table I in [132] was considered too large to fit the page size of this work. Therefore, the information in this table has been divided over Tables 6.1, 6.2 and 6.3.
In section 6.2, a similar semi-empirical description was derived for βDF probabilities. Again, this dependence was verified using literature data.
Since most of the experimental data was acquired in the neutron-deficient region

of the nuclear chart, the analysis presented in section 6.1 is focussed to fission preceded by β^+/EC decay. However, most nuclei important for the r-process nucleosynthesis are neutron-rich with respect to the valley of β stability (see also chapter 1). In section 6.3, the analysis was therefore extended to such nuclei. In particular, the possible competition of β-delayed fission and neutron emission was investigated.

6.1 β-delayed fission partial half-lives (Paper II)

PHYSICAL REVIEW C **91**, 044314 (2015)

Empirical description of β-delayed fission partial half-lives

L. Ghys[1,2], A. N. Andreyev[3,4],S. Antalic[5], M. Huyse[1], P. Van Duppen[1]

[1]*KU Leuven, Instituut voor Kern- en Stralingsfysica, 3001 Leuven, Belgium*
[2]*Belgian Nuclear Research Center SCK•CEN, Boeretang 200, B-2400 Mol, Belgium*
[3]*Department of Physics, University of York, York, YO10 5DD, United Kingdom*
[4]*Advanced Science Research Center, Japan Atomic Energy Agency, Tokai-Mura, Naka-gun, Ibaraki, 319-1195, Japan*
[5]*Departement of Nuclear Physics and Biophysics, Comenius University, 84248 Bratislava, Slovakia*
(Received 30 January 2015; published 16 April 2015)

DOI: 10.1103/PhysRevC.91.044314
PACS numbers: 24.75.+i, 23.40.-s, 21.10.Tg, 25.85.-w

Abstract

Background The process of β-delayed fission (βDF) provides a versatile tool to study low-energy fission in nuclei far away from the β-stability line, especially for nuclei which do not fission spontaneously.

Purpose The aim of this paper is to investigate systematic trends in βDF partial half-lives.

Method A semi-phenomenological framework was developed to systematically account for the behavior of βDF partial half-lives.

Results The βDF partial half-life appears to exponentially depend on the difference between the Q value for β decay of the parent nucleus and the fission-barrier energy of the daughter (after β decay) product. Such dependence was found to arise naturally from some simple theoretical considerations.

Conclusions This systematic trend was confirmed for experimental βDF partial half-lives spanning over 7 orders of magnitudes when using fission barriers calculated from either the Thomas-Fermi or the liquid-drop fission model. The same dependence was also observed, although less pronounced, when comparing to fission barriers from the finite-range liquid-drop model or the Thomas-Fermi plus Strutinsky Integral method.

6.1.1 Introduction

β-delayed fission (βDF) is a two-step process whereby the fissioning nucleus could be created in an excited state after β decay of a precursor. Since the excitation energy of the fissioning daughter product is limited by the Q_β value for β decay of the parent, βDF provides a unique tool to study low-energy fission of nuclei far from stability, especially for those not fissioning spontaneously. Figure 6.1 provides a schematic representation of this process, for nuclides on the neutron-deficient side of the nuclear chart. Recent experiments at ISOLDE-CERN [3, 4, 47, 74] and SHIP-GSI [48, 49] have studied this exotic decay mode in several short-lived neutron-deficient isotopes in the lead region. The fission-fragment mass and energy distributions resulting from βDF have established a new region of asymmetric fission around ^{178,180}Hg [3, 4] and indicated multimodal fission in ^{194,196}Po and ^{202}Rn [74]. A recent review of the βDF process is given in [42], in which a total of 27 βDF cases, both on the neutron-rich and neutron-deficient sides, were summarized.

It is furthermore believed that βDF could, together with neutron-induced and spontaneous fission, influence the fission-recycling in r-process nucleosynthesis [7, 8]. Therefore, a reliable prediction of the relative importance of βDF in nuclear decay, often expressed by the βDF probability $P_{\beta\mathrm{DF}}$, is needed. $P_{\beta\mathrm{DF}}$ is defined as

$$P_{\beta\mathrm{DF}} = \frac{N_{\beta\mathrm{DF}}}{N_\beta}, \tag{6.1}$$

where $N_{\beta DF}$ and N_β are respectively the number of βDF and β decays of the precursor nucleus. An earlier comparison of $P_{\beta\mathrm{DF}}$ data in a relatively narrow region of nuclei in the vicinity of uranium showed a simple exponential dependence with respect to Q_β [133, 134]. It was assumed that fission-barrier heights B_f of the daughter nuclei do not vary greatly in this region [135] ($B_\mathrm{f} \sim 4$–$6\,\mathrm{MeV}$) and thus have a smaller influence on $P_{\beta\mathrm{DF}}$ as compared to Q_β values ($Q_\beta \sim 3$–$6\,\mathrm{MeV}$). In addition, these nuclei have a typical N/Z ratio around ~ 1.4–1.5, which is close to that of traditional spontaneous fission of heavy actinides.

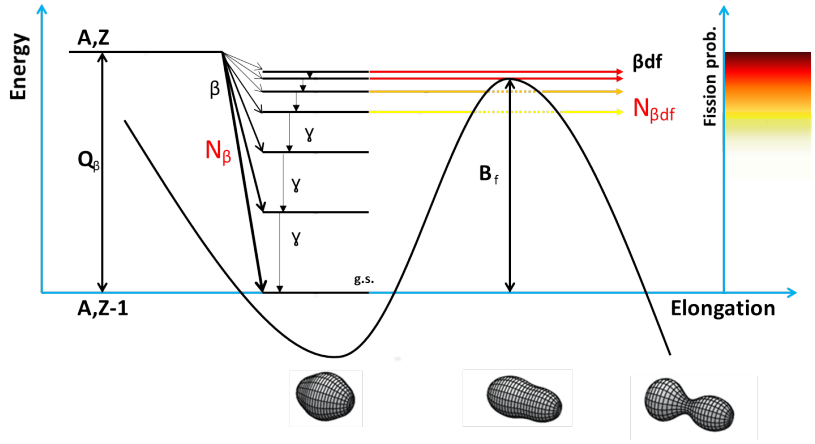

Figure 6.1: (In color) Schematic representation of the βDF process on the neutron-deficient side of the nuclear chart. The Q_{EC} value of the parent (A,Z) nucleus is indicated, while the curved line shows the potential energy of the daughter (A,Z-1) nucleus with respect to nuclear elongation, displaying also the fission barrier B_f. The color code on the right-hand side represents the probability for excited states, with excitation energies close to B_f, to undergo fission; the darker colors correspond to higher probabilities.

The aim of this paper is to further explore such systematic features by including the newly obtained data in the neutron-deficient lead region whose βDF nuclides have significantly different N/Z ratios ($\sim 1.2-1.3$), B_f ($\sim 7-10$ MeV) and Q_β values ($\sim 9-11$ MeV) as compared to those in the uranium region.
However, from an experimental point of view, the dominant α-branching ratio ($\gtrsim 90\,\%$) in most βDF precursors in the neutron-deficient lead region [1] makes precise determination of N_β in equation 6.1 difficult. Therefore, the partial βDF half-life $T_{1/2\mathrm{p},\beta\mathrm{DF}}$, as proposed in [42], is discussed in the present study. By analogy with other decay modes, $T_{1/2\mathrm{p},\beta\mathrm{DF}}$ is defined by

$$T_{1/2\mathrm{p},\beta\mathrm{DF}} = T_{1/2}\frac{N_\mathrm{dec,tot}}{N_{\beta\mathrm{DF}}}, \tag{6.2}$$

where $T_{1/2}$ represents the total half-life and $N_\mathrm{dec,tot}$ the number of decayed precursor nuclei. The relation between $T_{1/2\mathrm{p},\beta\mathrm{DF}}$ and $P_{\beta\mathrm{DF}}$ can be derived from equations 6.1 and 6.2 as

$$T_{1/2\mathrm{p},\beta\mathrm{DF}} = \frac{T_{1/2}}{b_\beta P_{\beta\mathrm{DF}}}, \tag{6.3}$$

with b_β denoting the β-branching ratio. If the α-decay channel dominates, as is often the case in the neutron-deficient lead region, one can safely approximate $N_{\mathrm{dec,tot}}$ in equation 6.2 by the amount of α decays N_α.
This work shows an apparent exponential dependence of $T_{1/2\mathrm{p},\beta\mathrm{DF}}$ on $(Q_\beta - B_\mathrm{f})$ for certain sets of calculated fission-barrier energies. Such relation may arise naturally by simple phenomenological approximations of the β-strength function of the precursor and the fission-decay width of excited states in the daughter nucleus. These assumptions may be justified considering the scale of the systematic trend discussed here, spanning $T_{1/2\mathrm{p},\beta\mathrm{DF}}$ values over several orders of magnitude. Deviations lower than one order of magnitude are thus acceptable.

6.1.2 Theoretical considerations

Following [16, 18, 136], the expression for $P_{\beta\mathrm{DF}}$ is given by

$$P_{\beta\mathrm{DF}} = \frac{\int_0^{Q_\beta} S_\beta(E) F(Q_\beta - E) \frac{\Gamma_\mathrm{f}(E)}{\Gamma_{\mathrm{tot}}(E)} dE}{\int_0^{Q_\beta} S_\beta(E) F(Q_\beta - E) dE}, \tag{6.4}$$

whereby the β-strength function of the parent nucleus is denoted by S_β and the Fermi function by F. The excitation energy is here, and further, given by E. The fission and total decay widths of the daughter, after β decay, are respectively given by Γ_f and Γ_{tot}. Equation 6.3 can be combined with equation 6.4 to deduce the decay constant of βDF, defined as $\lambda_{\beta\mathrm{DF}} = \ln(2)/T_{1/2\mathrm{p},\beta\mathrm{DF}}$, as

$$\lambda_{\beta\mathrm{DF}} = \int_0^{Q_\beta} S_\beta(E) F(Q_\beta - E) \frac{\Gamma_\mathrm{f}(E)}{\Gamma_{\mathrm{tot}}(E)} dE. \tag{6.5}$$

This section will be devoted to the derivation of an analytical expression for $\lambda_{\beta\mathrm{DF}}$ by approximating S_β, F and $\Gamma_\mathrm{f}/\Gamma_{\mathrm{tot}}$. Since most of the reliable experimental data on βDF are recorded on the neutron-deficient side of the nuclear chart (see Tables 6.2 and 6.3 and [42]), only EC/β^+-delayed fission will be considered here.

Approximations

A first simplification in equation 6.5 is to approximate S_β by a constant C_1, as proposed in previous studies (see for example [137, 138]). Possible resonant structures in S_β, considered in e.g. [16, 20], are thus ignored, thereby assuming a limited sensitivity of $T_{1/2\mathrm{p},\beta\mathrm{DF}}$ on S_β with respect to the scale of the systematic trend discussed here. This approximation is further supported by the study in [21], which shows a limited influence of S_β in the calculation of $P_{\beta\mathrm{DF}}$. Furthermore, C_1 was taken equal for all isotopes listed in Table 6.1, thereby neglecting possible variations of C_1 with respect to the nuclear properties of the βDF precursors - such as mass, proton number, isospin, spin and parity.
The Fermi function F can be fairly well described by the function $C_2(Q_{EC}-E)^2$ [19, 139, 140] for EC decay. The prefactor C_2 was again considered element independent, thereby ignoring its slight dependence on the atomic number Z [140].
According to [17, 140], EC decay is dominant for transition energies below 5 MeV if Z exceeds 80. Since Q_β values of βDF precursors in the uranium region are typically smaller than 5 MeV (see Table 6.1), β^+ decay can be disregarded here. Q_β values in the neutron-deficient lead region can however reach 10 – 11 MeV, implying a relatively high β^+ over EC decay ratio to the ground or a low-lying excited state in the daughter. However, since βDF should primarily happen at excitation energies which are only a few MeV below Q_β [60], EC-delayed fission should dominate over β^+ delayed fission in the full region of the nuclear chart (see further).
The prompt decay of an excited state in a nucleus can, in the most general case, happen through fission, emission of a γ ray, proton, α particle or neutron. The total decay width is thus given by $\Gamma_{\mathrm{tot}} = \Gamma_{\mathrm{f}} + \Gamma_\gamma + \Gamma_{\mathrm{p}} + \Gamma_\alpha + \Gamma_{\mathrm{n}}$.
For the βDF precursors considered in Table 6.1, the neutron separation energies exceed the Q_β value by at least several MeV [94] and charge particle-emission is strongly hindered due to the large Coulomb barrier. Therefore, the de-excitation of states below Q_β is mostly dominated by γ decay, which makes that $\Gamma_{\mathrm{tot}} \simeq \Gamma_\gamma$ [21, 141].
In addition, Γ_γ can be approximated by a constant (see for example [21]). Reference [141] provides a calculation of Γ_f with respect to the excitation energy E by including the fission-barrier penetrability and the influence of level densities at the ground state and saddle point. This calculation shows that Γ_{f} seems well approximated by a single exponential behavior $\Gamma_{\mathrm{f}} \sim e^{-X(B_{\mathrm{f}}-E)}$ at excitation energies around B_{f}. For the fissile nuclei listed Table 6.1, a value of X around 4 MeV^{-1} was found to provide a good description of the calculated behavior of Γ_{f} with respect to E in the vicinity of B_f [141]. The ratio $\Gamma_{\mathrm{f}}/\Gamma_{\mathrm{tot}}$ is thus approximated by

$$\frac{\Gamma_{\mathrm{f}}}{\Gamma_{\mathrm{tot}}}(E) \simeq \frac{\Gamma_{\mathrm{f}}}{\Gamma_{\gamma}}(E) \approx C_3 e^{-X(B_{\mathrm{f}}-E)}. \tag{6.6}$$

The constants C_3 and X are assumed to adopt the same value for all isotopes of interest. At excitation energies E moderately above B_{f}, de-excitation by fission should dominate and $\Gamma_{\mathrm{f}}/\Gamma_{tot}(E)$ will thus be close to unity. Since the Q_β value of most known βDF precursors (see Table 6.1) does not exceed B_{f} of the daughter by more than a few MeV, it is further assumed that equation 6.6 remains valid for excitation energies in the daughter nucleus close to Q_β.
Using the above approximations and taking $C = C_1 C_2 C_3$, the right-hand side of equation 6.5 reduces to

$$\lambda_{\beta\mathrm{DF}} = C \int_0^{Q_\beta} (Q_\beta - E)^2 e^{-X(B_{\mathrm{f}}-E)} dE. \tag{6.7}$$

Calculating $\lambda_{\beta\mathrm{DF}}$

Equation (6.7) can be rewritten, in order to isolate the exponential dependence on $(Q_\beta - B_{\mathrm{f}})$, as

$$\lambda_{\beta\mathrm{DF}} = C e^{X(Q_\beta - B_{\mathrm{f}})} \int_0^{Q_\beta} (Q_\beta - E)^2 e^{-X(Q_\beta - E)} dE. \tag{6.8}$$

The integrand in equation 6.8 is thus proportional to the βDF probability at a given E of the daughter nucleus. This function, plotted in Figure 6.2 for different values of X around the deduced value $X \approx 4\,\mathrm{MeV}^{-1}$ from [141], shows that βDF primarily happens at energy levels $0-2\,\mathrm{MeV}$ below Q_β. Moreover, since all Q_β values of the neutron-deficient βDF precursors listed in Table 6.1 exceed $\sim 2\,\mathrm{MeV}$, the value of the integral in equation 6.8 is little dependent on the precise value of Q_β. As a consequence, $\lambda_{\beta\mathrm{DF}}$ primarily depends on the difference $(Q_\beta - B_{\mathrm{f}})$.

In order to prove latter statement analytically, a substitution with $u = X(Q_\beta - E)$ and adjustment of integration borders in equation 6.8 is performed:

$$\lambda_{\beta\mathrm{DF}} = \frac{C e^{X(Q_\beta - B_{\mathrm{f}})}}{X^3} \int_0^{XQ_\beta} u^2 e^{-u} du. \tag{6.9}$$

The integral in equation 6.9 is similar to the mathematical form of the so-called normalized upper incomplete Gamma function, defined as

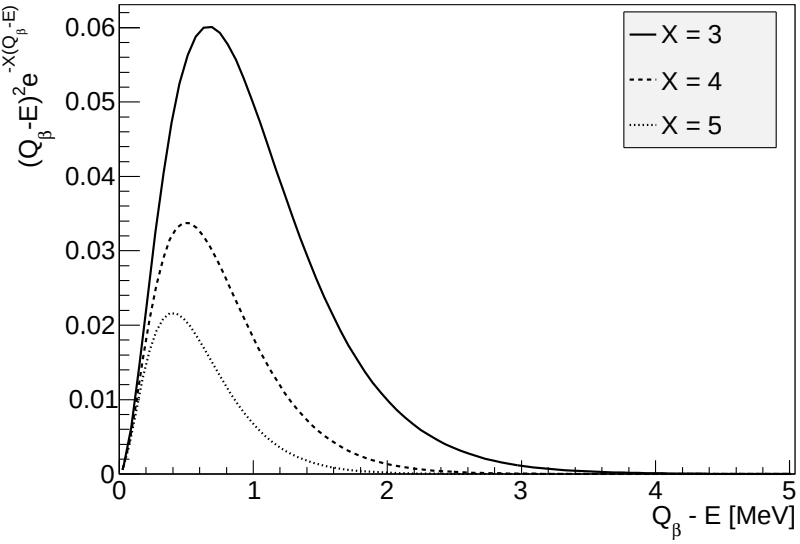

Figure 6.2: Plot showing the integrand of equation 6.8, which is proportional to the βDF probability, for X equal to 3,4 or 5.

$$\Gamma(s,x) = \frac{1}{\Gamma(s)} \int_0^x t^{s-1} e^{-t} dt, \tag{6.10}$$

whereby $\Gamma(s)$ is

$$\Gamma(s) = \int_0^{+\infty} t^{s-1} e^{-t} dt. \tag{6.11}$$

Equation (6.9) thus transforms into

$$\lambda_{\beta\mathrm{DF}} = \frac{C e^{X(Q_\beta - B_\mathrm{f})}}{X^3} \Gamma(3)\Gamma(3, XQ_\beta). \tag{6.12}$$

Table 6.1 shows that all Q_β values of the neutron-deficient βDF precursors exceed 3 MeV, while the fitted values for X in Table 6.4, as well as the theoretical estimate from [141] ($X \approx 4\,\mathrm{MeV}^{-1}$), are all greater than $1.7\,\mathrm{MeV}^{-1}$. The value XQ_β thus exceeds 5 in all discussed cases, implying that, as shown in Figure 6.3, one can thus safely approximate $\Gamma(3, XQ_\beta) \simeq 1$ in equation 6.12.

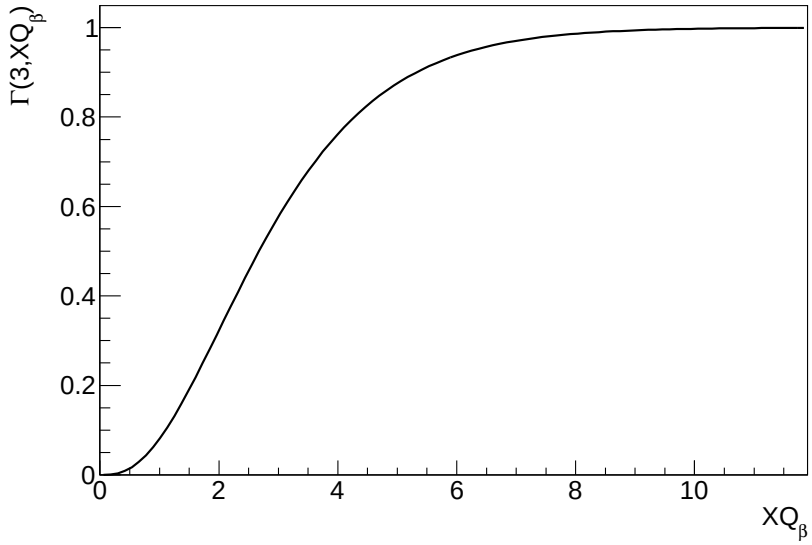

Figure 6.3: The normalized incomplete Gamma function $\Gamma(3, XQ_\beta)$, needed for the calculation of the integral under the βDF probability curves shown in Figure 6.2.

In this simple picture, it is thus found that $\ln(\lambda_{\beta DF})$ depends linearly on $(Q_\beta - B_\mathrm{f})$. In terms of the partial βDF half-life $T_{1/2\mathrm{p},\beta\mathrm{DF}}$ one finds the relation

$$\log_{10}(T_{1/2\mathrm{p},\beta\mathrm{DF}}) = C' - X\log_{10}(e)(Q_\beta - B_\mathrm{f}), \tag{6.13}$$

with the constant C' given by

$$C' = \ln\left(\frac{\ln(2)X^3}{C\Gamma(3)}\right)\log_{10}(e). \tag{6.14}$$

6.1.3 Systematic comparison of experimental data

This section aims at verifying equation 6.13 by using experimental βDF partial half-lives and theoretical values for $(Q_\beta - B_\mathrm{f})$, summarized in Tables 6.1, 6.2, 6.3 and in Figure 6.4. Tabulated fission barriers from four different fission models were used, of which three are based on a macroscopic-microscopic and one a mean-field approach. The latter model is based on the Extended Thomas-

Fermi plus Strutinsky Integral (ETFSI) method [13], but tabulated barriers for the most neutron-deficient isotopes in Table 6.1 are absent in literature. The microscopic-macroscopic approaches all rely on shell corrections from [11] and describe the macroscopic structure of the nucleus by either a Thomas-Fermi (TF) [10], liquid-drop (LDM) [141] or the Finite-Range Liquid-Drop Model (FRLDM) [41]. The Q_β values were taken from the 2012 atomic mass evaluation tables [94] and are derived from the difference between the atomic masses of parent $M_P(Z, A)$ and daughter $M_D(Z', A)$ nuclei as

$$Q_\beta = c^2[M_P(Z, A) - M_D(Z', A)]. \tag{6.15}$$

About half of these values are known from experiments, while the others are deduced from extrapolated atomic masses. In latter cases, the difference of the Q_β values from [94] with the theoretical values from [11] or [76] is always lower than 0.4 MeV.

$T_{1/2\mathrm{p},\beta\mathrm{DF}}$ values were extracted from reported $P_{\beta\mathrm{DF}}$ values using equation 6.3, if the precursor nucleus has a significant β-decay branch ($b_\beta \gtrsim 10\,\%$). When multiple measurements on $P_{\beta\mathrm{DF}}$ were performed, only the reliable value, as evaluated by [42], or the most recent value was tabulated. In case of a dominant α-decay branch ($b_\beta \lesssim 10\,\%$), $T_{1/2\mathrm{p},\beta\mathrm{DF}}$ was calculated by equation 6.2, whereby $N_{\mathrm{dec,tot}}$ was approximated by the observed amount of α decays N_α, corrected for detection efficiency.
Since the isotopes ^{186,188}Bi, ^{192,194}At and ^{202}Fr have all a ground and a low-lying alpha-decaying isomeric state with comparable half-lives, only an overall $N_{\beta\mathrm{DF}}/N_\alpha$ value could be extracted with present experimental techniques. We refer the reader for a detailed discussion of this issue to [48, 49, 74]. Therefore, these precursors have been excluded from the fit in Figure 6.4. Nonetheless, as a first approximation the value for $T_{1/2p,\beta\mathrm{DF}}$ was extracted by defining the half-life $T_{1/2}$, shown in Tables 6.2 and 6.3, as the unweighted average

$$T_{1/2} = \frac{T_{1/2,\mathrm{g}} + T_{1/2,\mathrm{m}}}{2}. \tag{6.16}$$

where the respective half-lives for ground and isomeric states are denoted by $T_{1/2,\mathrm{g}}$ and $T_{1/2,\mathrm{m}}$. The uncertainty $\Delta T_{1/2}$ is conservatively taken as

$$\Delta T_{1/2} = \frac{|T_{1/2,\mathrm{g}} - T_{1/2,\mathrm{m}}|}{2}. \tag{6.17}$$

Table 6.1: List of all precursors for which βDF was observed. $(Q_\beta - B_\mathrm{f})$ is tabulated for fission barriers from four different fission models : Thomas-Fermi (TF) [10], Finite Range Liquid Drop (FRLDM) [41], Liquid Drop (LDM) [141] and the Extended Thomas-Fermi plus Strutinsky Integral (ETFSI) model [13]. Q_β values were taken from [94] and are defined by equation 6.15.

		$Q_\beta - B_\mathrm{f}$ (MeV)			
precursor	Q_β (MeV)	TF	FRLDM	LDM	ETFSI
β^+/EC-delayed fission in the neutron-deficient lead region					
^{178}Tl	11.5	2.5	2.2	3.0	
^{180}Tl	11.0	1.4	1.2	2.6	
^{186g,m}Bi	11.6	2.8	2.0	3.1	
^{188g,m}Bi	10.6	0.9	0.3	1.2	
^{192g,m}At	11.0	4.2	2.8	4.2	
^{194g,m}At	10.3	2.5	0.8	2.7	
^{196}At	9.6	0.3	-0.7	1.1	
^{200}Fr	10.2	3.3	1.5	3.7	
^{202g,m}Fr	9.4	0.8	-0.9	0.7	
β^+/EC-delayed fission in the neutron-deficient uranium region					
^{228}Np	4.4	0.0	-0.8	0.3	
^{232}Am	4.9	1.3	1.7	0.5	
^{234}Am	4.1	0.0	0.3	-0.3	-0.1
^{238}Bk	4.8	1.1	-0.2	0.4	-0.1
^{240}Bk	3.9	-0.3	-1.9	-0.8	-1.6
^{242}Es	5.4	1.8	-0.7	1.2	-0.1
^{244}Es	4.5	0.2	-2.2	-0.3	-1.7
^{246}Es	3.8	-0.8	-3.4	-1.7	-2.7
^{248}Es	3.1	-1.9	-4.2	-2.8	-3.6
^{246m2}Md	5.9	2.1	-0.2	1.6	0.0
^{250}Md	4.6	-0.3	-2.7	-1.0	-2.1
β^--delayed fission in the neutron-rich uranium region					
^{228}Ac	2.1	-4.0	-4.4	-4.4	-4.3
^{230}Ac	3.0	-3.4	-2.7	-3.7	-3.8
^{234g}Pa	2.2	-3.4	-2.7	-3.8	-2.6
^{234m}Pa	2.2	-3.4	-2.7	-3.8	-2.6
^{236}Pa	2.9	-2.9	-2.1	-3.2	-2.3
^{238}Pa	3.6	-2.3	-2.0	-3.2	-2.1
^{256m}Es	1.7	-2.3	-3.4	-3.2	-3.8

Table 6.2: List of all precursors in the lead region for which βDF was observed. The measured half-life $T_{1/2}$, β-branching ratio b_β, βDF probability $P_{\beta\mathrm{DF}}$, ratio of observed βDF to α decays $N_{\beta\mathrm{DF}}/N_\alpha$ and calculated βDF partial half-lives $T_{1/2p,\beta\mathrm{DF}}$ are listed. Reliable values for $T_{1/2p,\beta\mathrm{DF}}$, as evaluated by the criteria in [42], are indicated in bold.

precursor	$T_{1/2}$ (s)	b_β	$P_{\beta\mathrm{DF}}$	$N_{\beta\mathrm{DF}}/N_\alpha$	$T_{1/2p,\beta\mathrm{DF}}$ (s)	ref.
β^+/EC-delayed fission in the neutron-deficient lead region						
^{178}Tl	0.25(2)	0.38(2)	$1.5(6)\times10^{-3}$		$\mathbf{4(2)\times10^{2}}$	[4]
^{180}Tl	1.09(1)	0.94(4)	$3.2(2)\times10^{-5}$		$\mathbf{3.6(3)\times10^{4}}$	[47]
^{186g,m}Bi	0.012(3)[a]	~ 0.006[b]		$2.2(13)\times10^{-4}$	56(35)	[48]
^{188g,m}Bi	0.16(10)[a]	~ 0.03[a]		$3.2(16)\times10^{-5}$	$5(4)\times10^{3}$	[48]
^{192g,m}At	0.05(4)[a]	~ 0.03[a]		$4.2(9)\times10^{-3}$	12(9)	[49]
^{194g,m}At	0.28(3)[a]	~ 0.08[a]		$5.9(4)\times10^{-5}$	$4.8(6)\times10^{2}$	[74]
^{196}At	0.358(5)	0.026(1)	$9(1)\times10^{-5}$	$2.3(2)\times10^{-6}$	$\mathbf{1.5(2)\times10^{5}}$	[74, 103]
^{200}Fr	0.049(4)[c]	$< 0.021(4)$	$> 3.1(17)\times10^{-2}$	$7^{+5}_{-3}\times10^{-4}$	$\mathbf{7^{+6}_{-3}\times10}$	[74]
^{202g,m}Fr	0.33(4)[d]	~ 0.007[a]		$7.3(8)\times10^{-7}$	$4.5(8)\times10^{4}$	[74]

[a] Value extracted according to equation 6.16 by using evaluated experimental data from [1].
[b] Calculated β-branching ratio from [142].
[c] Evaluated value from [1]
[d] Value extracted according to equation 6.16 by using experimental data from [50].

Table 6.3: Idem as Table 6.2, but now for βDF precursors in the uranium region.

precursor	$T_{1/2}$ (s)	b_β	$P_{\beta\mathrm{DF}}$	$N_{\beta\mathrm{DF}}/N_\alpha$	$T_{1/2p,\beta\mathrm{DF}}$ (s)	ref.
β^+/EC-delayed fission in the neutron-deficient uranium region						
^{228}Np	61(1)	0.60(7)	$2.0(9)\times10^{-4}$		$\mathbf{5.1(2)\times10^{5}}$	[143]
^{232}Am	79(2)	$\sim 0.96^{a}$	$6.9(10)\times10^{-4}$		$\mathbf{1.2(2)\times10^{5}}$	[144]
^{234}Am	139(5)	$\sim 1.00^{a}$	$6.6(18)\times10^{-5}$		$\mathbf{2.1(6)\times10^{6}}$	[145]
^{238}Bk	144(5)	$\sim 0.95^{a}$	$4.8(20)\times10^{-4}$		$\mathbf{3.2(13)\times10^{5}}$	[146]
^{240}Bk	252(48)	$\sim 1.00^{a}$	$1.3^{+1.8}_{-0.7}\times10^{-5}$		$\mathbf{1.9^{+2.3}_{-1.1}\times10^{7}}$	[147]
^{242}Es	11(3)	$0.57(3)^{b}$	$6(2)\times10^{-3}$		$\mathbf{3(1)\times10^{3}}$	[133]
^{244}Es	$37(4)^{c}$	$0.96(3)^{c}$	$1.2(4)\times10^{-4}$		$\mathbf{3(1)\times10^{5}}$	[134]
^{246}Es	462(30)	$0.901(18)^{c}$	$3.7^{+8.5}_{-3.0}\times10^{-5}$		$\mathbf{1.4^{+5.9}_{-1.0}\times10^{7}}$	[149]
^{248}Es	$1.4(2)\times10^{3}$	$0.997(3)^{c}$	$3.5(18)\times10^{-6}$		$\mathbf{4.0(21)\times10^{8}}$	[149]
^{246m2}Md	4.4(8)	> 0.77	> 0.1		< 57	[148]
^{250}Md	$52(6)^{c}$	$0.93(3)^{c}$	$2^{+2}_{-1}\times10^{-4}$		$3^{+3}_{-1}\times10^{5}$	[136]
β^--delayed fission in the neutron-rich uranium region						
^{228}Ac	$2.214(7)\times10^{4\,c}$	$\sim 1.00^{a}$	$5(2)\times10^{-12}$		$4(2)\times10^{15}$	[150]
^{230}Ac	$122(3)^{c}$	$\sim 1.00^{a}$	$1.19(40)\times10^{-9}$		$1.0(3)\times10^{10}$	[151]
^{234g}Pa	$2.41(2)\times10^{4\,c}$	$\sim 1.00^{a}$	$3\times10^{-(12\pm1)}$		$8\times10^{(15\pm1)}$	[152]
^{234m}Pa	$69.54(66)^{c}$	0.9984(4)	$10^{-(12\pm1)}$		$7\times10^{(13\pm1)}$	[152]
^{236}Pa	$546(6)^{c}$	$\sim 1.00^{a}$	$10^{-9\pm1}$		$5\times10^{(11\pm1)}$	[152]
^{238}Pa	$138(6)^{c}$	$\sim 1.00^{a}$	$< 2.6\times10^{-8}$		$> 5.3\times10^{9}$	[153]
^{256m}Es	$2.7\times10^{4\,c}$	$\sim 1.00^{a}$	$\sim 2\times10^{-5}$		$\sim 1\times10^{9}$	[154]

[a] Calculated β-branching ratio from [142].
[b] β-branching ratio from [148].
[c] Evaluated value from [1]

Table 6.4: Results of the fits, corresponding to four different fission models, shown in Figure 6.4. The values for the parameters X and C' in equation 6.13 are listed. Also the root-mean-square deviations (RMSD) of the reliable experimental $\log_{10}(T_{1/2\mathrm{p},\beta\mathrm{DF}})$ values (represented by the closed symbols in Figure 6.4) to the fit are given.

Model	X (MeV^{-1})	C' (MeV)	RMSD
TF	3.0(2)	6.2(1)	0.47
FRLDM	1.7(4)	4.9(3)	1.19
ETFSI	2.1(7)	5.0(6)	1.10
LDM	2.2(2)	5.8(2)	0.62

Figure 6.4 shows $\log_{10}(T_{1/2\mathrm{p},\beta\mathrm{DF}})$ against $(Q_\beta - B_\mathrm{f})$ for the fission barriers from the four different models under consideration. Using the same evaluation criteria as proposed in [42] for $P_{\beta\mathrm{DF}}$ measurements, 13 reliable $T_{1/2p,\beta\mathrm{DF}}$ values, marked in bold in Tables 6.2 and 6.3, were selected. These data points, represented by the closed symbols, are fitted by a linear function. An equal weight to all fit points is given because the experimental uncertainties on $\log_{10}(T_{1/2\mathrm{p},\beta\mathrm{DF}})$ are in most cases much smaller than the deviation of the data points with the fitted line, of which the extracted parameters are summarized in Table 6.4. The remaining data points from Tables 6.2 and 6.3 are shown by open symbols and were excluded from the fit. The color code discriminates between the neutron-deficient lead region (red), neutron-deficient (black) and neutron-rich (blue) uranium region.

Figure 6.4 illustrates a linear dependence of $\log_{10}(T_{1/2\mathrm{p},\beta\mathrm{DF}})$ on $(Q_\beta - B_\mathrm{f})$ for TF and LDM barriers for over 7 orders of magnitude of $T_{1/2p,\beta\mathrm{DF}}$. In addition, Table 6.4 shows a relatively small root-mean-square deviation (RMSD) of the 13 reliable experimental $\log_{10}(T_{1/2\mathrm{p},\beta\mathrm{DF}})$ values (represented by the closed symbols in Figure 6.4) to the corresponding values extracted from the fit. The dependence is somewhat less pronounced for the FRLDM model, as evidenced by a larger RMSD value. A similar linear trend is observed for the ETFSI model, but the lack of tabulated fission barriers in the neutron-deficient region, especially in the lead region, prohibits drawing definite conclusions.
Moreover, Table 6.4 shows that the four fitted values for X are similar to each other as well as to the theoretical estimate $X \approx 4\,\mathrm{MeV}^{-1}$ [141]. The extracted values for the offset C' are also found to be comparable.

In contrast to a rather good agreement for most neutron-deficient nuclei, all models show a larger systematical deviation from this linear trend for the

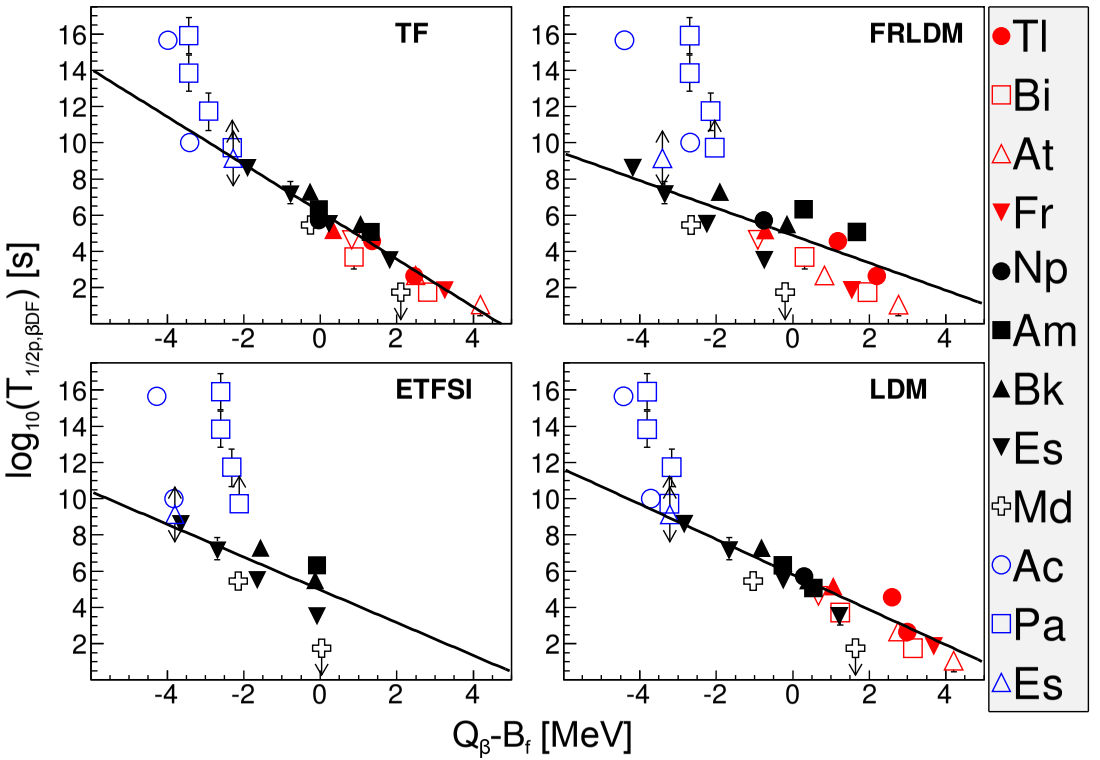

Figure 6.4: (Color online) Plots of $T_{1/2\mathrm{p},\beta\mathrm{DF}}$ versus $(Q_\beta - B_\mathrm{f})$ for different fission models as listed in Tables 6.1, 6.2 and 6.3. The closed symbols, representing reliable values for $T_{1/2p,\beta\mathrm{DF}}$ in Tables 6.2 and 6.3 are used for a linear fit with equal weights to the data points. Other data are indicated by the open symbols. The color code represents the different regions of the nuclear chart for which βDF has been experimentally observed : the neutron-deficient lead region (red), the neutron-deficient (black) and neutron-rich (blue) uranium region.

neutron-rich βDF precursors ^{228}Ac and ^{234,236}Pa. In [42], concerns were raised on the accuracy of the $P_{\beta\mathrm{DF}}$ values measured in this region, which could explain this deviation. Note also that the precursors in this region of the nuclear chart undergo β^- decay in contrast to the EC-delayed fission on the neutron-deficient side for which equation 6.13 was deduced, influencing the numeric value of the offset C'. In particular, the Fermi function for β^- decay is approximately proportional to $(Q_\beta - E)^5$ [18, 19], in contrast to the quadratic dependence on $(Q_\beta - E)$ for EC decay. The parameter X should however remain unchanged, because equation 6.6 approximating $\Gamma_\mathrm{f}/\Gamma_\mathrm{tot}$ remains valid as long as the neutron-separation energy S_n is larger than Q_β. At excitation energies higher than S_n, de-excitation through neutron emission is favored over decay by γ-ray emission, which implies that $\Gamma_\mathrm{tot} \simeq \Gamma_\mathrm{n} \gg \Gamma_\gamma, \Gamma_\mathrm{f}$ [23, 141]. For all nuclei mentioned in Table 6.1 however, Q_β is below S_n. An approximation of $T_{1/2p,\beta\mathrm{DF}}$, similar to equation 6.13, can thus also be derived for neutron-rich βDF precursors by taking into account above considerations. However, considering the limited experimental information on βDF in the neutron-rich region, a detailed derivation is omitted in this paper.

6.1.4 Conclusions

Recent experiments have measured the βDF of 9 precursor nuclei in the neutron-deficient lead region. Because of the dominant α-decay branch in most of these nuclei, βDF probabilities are extracted with large experimental uncertainties. In contrast, the partial half-life for βDF can be determined with a better accuracy. In addition, $T_{1/2\mathrm{p},\beta\mathrm{DF}}$ can be easily derived from the βDF probability by using equation 6.3.

A systematical evaluation of βDF partial half-lives was performed by using fission barriers deduced from four different models for a broad range of nuclei in the lead and uranium regions. A linear relation between $\log_{10}(T_{1/2\mathrm{p},\beta\mathrm{DF}})$ and $(Q_\beta - B_\mathrm{f})$ was observed for neutron-deficient precursor nuclei, when using tabulated fission barriers from the TF or LDM approach, and to a lesser extent for FRLDM and ETFSI barriers. This linear trend persists for values of $T_{1/2\mathrm{p},\beta\mathrm{DF}}$ spanning over 7 orders of magnitude and a wide variety of precursor nuclei going from ^{178}Tl to ^{248}Es with N/Z ratios of 1.20 and 1.51 respectively. This observation may help to assess βDF branching-ratios in very neutron-rich nuclei, which are inaccessible by present experimental techniques but might play a role in the fission-recycling mechanism of the r-process nucleosynthesis.

Acknowledgements

This work has been funded by FWO-Vlaanderen (Belgium), by the Slovak Research and Development Agency (Contract No. APVV-0105-10), by the UK Science and Technology Facilities Council (STFC), by the Slovak grant agency VEGA (contract No. 1/0576/13), by the Reimei Foundation of JAEA, and by the European Commission within the Seventh Framework Programme through I3-ENSAR (Contract No. RII3-CT-2010-262010).

6.2 β-delayed fission probabilities

A similar analysis as presented in section 6.1 can be employed to investigate the dependence of βDF probabilities $P_{\beta\mathrm{DF}}$ with respect to $(Q_\beta - B_\mathrm{f})$. If a constant β-strength function $S_\beta \simeq C_1$ is assumed and $\Gamma_\mathrm{f}/\Gamma_\mathrm{tot}$ is approximated by expression 6.6, equation 6.4 reduces to

$$P_{\beta\mathrm{DF}} \simeq \frac{\int_0^{Q_\beta} F(Q_\beta - E) C_3 e^{-X(B_\mathrm{f}-E)} dE}{\int_0^{Q_\beta} F(Q_\beta - E) dE}. \tag{6.18}$$

Note that the constant C_1 is absent in this expression.
As indicated before, the Fermi function F can be approximated for EC decay by a quadratic dependence on $(Q_\beta - E)$. In the case of β^-/β^+ decay, a dependence of $F(Q_\beta - E)$ to the fifth power of $(Q_\beta - E)$ is assumed [18, 19]. One can therefore write

$$F(Q_\beta - E) = \begin{cases} C_2(Q_\mathrm{EC} - E)^2 & \text{for EC decay,} \\ C_2'(Q_{\beta^+} - E)^5 & \text{for } \beta^+ \text{ decay,} \\ C_2''(Q_{\beta^-} - E)^5 & \text{for } \beta^- \text{ decay,} \end{cases} \tag{6.19}$$

As can be inferred from expression 2.2 if B_n is neglected (typically $\lesssim 100\,\mathrm{keV}$ [17]), Q_EC and Q_{β^-} are defined by equation 6.15 and are thus equal to the Q_β values in Table 6.1. However, Q_{β^+} differs from Q_EC by an energy of $2m_ec^2 = 1.022\,\mathrm{MeV}$ and therefore $Q_{\beta^+} = Q_\beta - 1.022\,\mathrm{MeV}$.
The power-law dependence of F with respect to $(Q_\beta - E)$ implies that the integrand in the denominator of equation 6.18 rises for decreasing values of E. The corresponding integral is thus mostly depending on F at low E. On the other hand, as shown in Figure 6.2, the integral of the numerator is mainly determined by energy levels $0 - 2$ MeV below Q_β. As indicated in section 6.1.2, β^+ decay can be disregarded for the isotopes in the neutron-deficient

uranium region listed in Table 6.1, due to their relatively low Q_β value. However, β^+ decay should dominate for transitions to low-lying excited states in the neutron-deficient lead region, since Q_β can reach $\sim 11\,\mathrm{MeV}$ (see also Table 6.1). Therefore, $P_{\beta\mathrm{DF}}$ should be approximated differently according to the region of the nuclear chart considered:

$$P_{\beta\mathrm{DF}} \simeq \begin{cases} \dfrac{C_2 C_3 \int_0^{Q_\beta} (Q_\beta - E)^2 e^{-X(B_\mathrm{f}-E)} dE}{C_2' \int_0^{Q_\beta} (Q_\beta - E - 1.022\,\mathrm{MeV})^5 dE} & \text{(n-def Pb region)}, \\ \dfrac{C_3 \int_0^{Q_\beta} (Q_\beta - E)^2 e^{-X(B_\mathrm{f}-E)} dE}{\int_0^{Q_\beta} (Q_\beta - E)^2 dE} & \text{(n-def U region)}, \\ \dfrac{C_3 \int_0^{Q_\beta} (Q_\beta - E)^5 e^{-X(B_\mathrm{f}-E)} dE}{\int_0^{Q_\beta} (Q_\beta - E)^5 dE} & \text{(n-rich U region)}. \end{cases} \tag{6.20}$$

The integrals in equation 6.20 can be determined with an analysis similar to section 6.1.2. In the case of βDF in the neutron-rich region, the solution of the integral in equation 6.20 involves the function $\Gamma(6, XQ_\beta)$. As illustrated in Figure 6.5, one can assume $\Gamma(6, XQ_\beta) \simeq 1$ for $X * Q_\beta \gtrsim 5$, which is true for most of the Q_β values given in Table 6.1 and fitted values of X in Table 6.4. In addition, calculations from [140] show that the ratio $C_2/C_2' \simeq 40$. $P_{\beta\mathrm{DF}}$ can therefore be written as

$$P_{\beta\mathrm{DF}} \simeq \begin{cases} \frac{240 C_3 \Gamma(3)}{X^3 (Q_\beta - 1.022\,\mathrm{MeV})^6} e^{X(Q_\beta - B_\mathrm{f})} & \text{(n-def Pb region)}, \\ \frac{C_3 3\Gamma(3)}{X^3 Q_\beta^3} e^{X(Q_\beta - B_\mathrm{f})} & \text{(n-def U region)}, \\ \frac{C_3 6\Gamma(6)}{X^6 Q_\beta^6} e^{X(Q_\beta - B_\mathrm{f})} & \text{(n-rich U region)}. \end{cases} \tag{6.21}$$

Each of these equations can thus be written in the form

$$P_{\beta\mathrm{DF}} \simeq C_3 P(Q_\beta, X) e^{X(Q_\beta - B_\mathrm{f})}. \tag{6.22}$$

Equivalently, one has the relation

$$\log_{10}\left(\frac{P_{\beta\mathrm{DF}}}{P(Q_\beta, X)}\right) = \log_{10}(C_3) + X \log_{10}(e)(Q_\beta - B_\mathrm{f}). \tag{6.23}$$

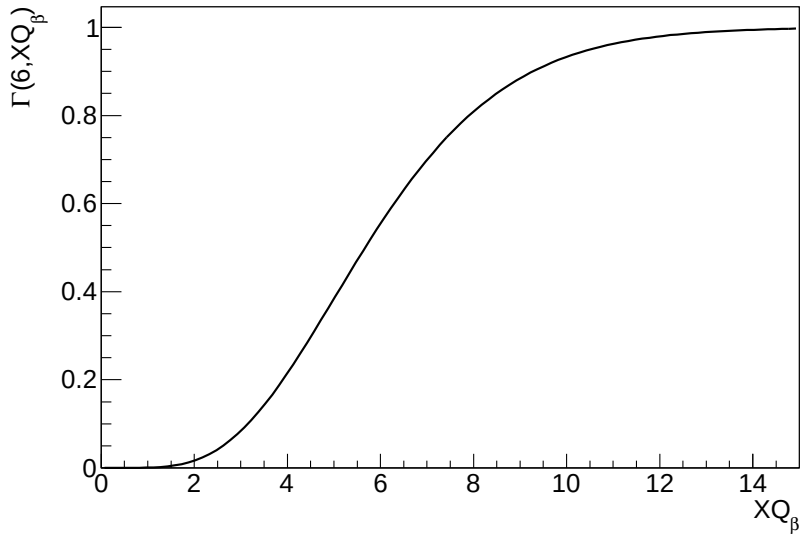

Figure 6.5: The normalized incomplete Gamma function $\Gamma(6, XQ_\beta)$, needed for the calculation of $P_{\beta\mathrm{DF}}$ in the n-rich region of the nuclear chart, which is approximatively given by the expression in equation 6.20.

The validity of equation 6.23 was verified using the literature data in Tables 6.2 and 6.3. In addition, estimated $P_{\beta\mathrm{DF}}$ values for ^{192}At, ^{186,188}Bi were taken from [49] and [48] respectively and the overall $P_{\beta\mathrm{DF}}$ values for ^{194}At and ^{200,202}Fr, listed in Table 4.3, were included in the analysis. In analogy with Figure 6.4, $\log_{10}(P_{\beta\mathrm{DF}}/(P(Q_\beta, X)$ is plotted against $(Q_\beta - B_\mathrm{f})$ in Figure 6.6, whereby B_f is calculated using four fission models: TF, FRLDM, ETFSI or LDM. Since the prefactor P in equation 6.23 depends on X, it was determined by an iterative procedure.
Again, using the evaluation criteria from [42], 12 reliable data points were selected, mostly corresponding to the βDF isotopes in Tables 6.2 and 6.3 for which the $T_{1/2\mathrm{p},\beta\mathrm{DF}}$ values are marked in bold. However, the $P_{\beta\mathrm{DF}}$ value of ^{200}Fr was not selected, since only an upper limit for this value could be extracted.
The linear fits in Figure 6.6 are based on these reliable data points, which are indicated by the closed symbols. The fit parameters, as well as the RMSD of the fitted data points are listed in Table 6.5. Also here, the linear trend indicated in equation 6.23 is observed for a wide range of $P_{\beta\mathrm{DF}}$ values and for all investigated fission models. Within error bars, the values of X corresponding to a given fission model are equal to the ones given in Table 6.4. Remarkably, the fitted values for $\log_{10}(C_3)$ agree well for all four models and an approximate

Table 6.5: Results of the fits, corresponding to four different fission models, shown in Figure 6.6. The values for the parameters X and $\log_{10}(C_3)$ in equation (6.23) are listed. Also the root-mean-square deviations (RMSD) of the reliable values of $\log_{10}(P_{\beta DF}/P(Q_\beta, X))$, represented by the closed symbols in Figure 6.6, to the fit are given.

Model	X (MeV^{-1})	$\log_{10}(C_3)$ (MeV)	RMSD
TF	2.7(3)	-1.5(2)	0.59
FRLDM	1.4(3)	-1.4(3)	0.97
ETFSI	1.7(6)	-1.3(5)	0.86
LDM	2.0(2)	-1.6(2)	0.52

value of $C_3 \approx 0.03$ could be deduced. The RMSD values listed in Table 6.5 also indicates a better fit for the FRLDM and ETFSI model as compared to the fit from Figure 6.4, which might be attributed to the normalization in equation 6.4, removing the constant C_1 associated with the β-strength function.
The data points on the neutron-rich side of the nuclear chart again deviate from this linear trend, although the different functionality of $F(Q_\beta - E)$ for β^- decay in comparison to EC decay was now taken into account. As indicated already in section 6.1.3 however, concerns about the accuracy and reliability of the measured $P_{\beta DF}$ were raised in [42].

6.3 $T_{1/2p,\beta DF}$ for neutron-rich isotopes

The phenomenological description of $T_{1/2p,\beta DF}$ or $P_{\beta DF}$ may aid to predict βDF-branching ratios for super-heavy nuclei important for the fission-recycling in the stellar r-process nucleosynthesis (see also chapter 1). This section therefore aims to verify if the relation 6.13 might still hold for such nuclei.
In contrast to the the βDF isotopes listed in Table 6.1, Q_β is larger than the neutron-separation energy S_n in many nuclides at the end of the nuclear chart [7]. In general, when the excitation energy of a nucleus exceeds S_n, neutron emission is the dominant decay channel over prompt γ-emission [23, 141]. One thus has

$$\Gamma_{tot} \simeq \Gamma_n \gg \Gamma_\gamma \tag{6.24}$$

Therefore, Γ_f/Γ_{tot} in the integrand of equation 6.5 is assumed to be negligibly small if E exceeds S_n. In other words, the upper boundary of the integral in equation 6.5 is approximated by S_n:

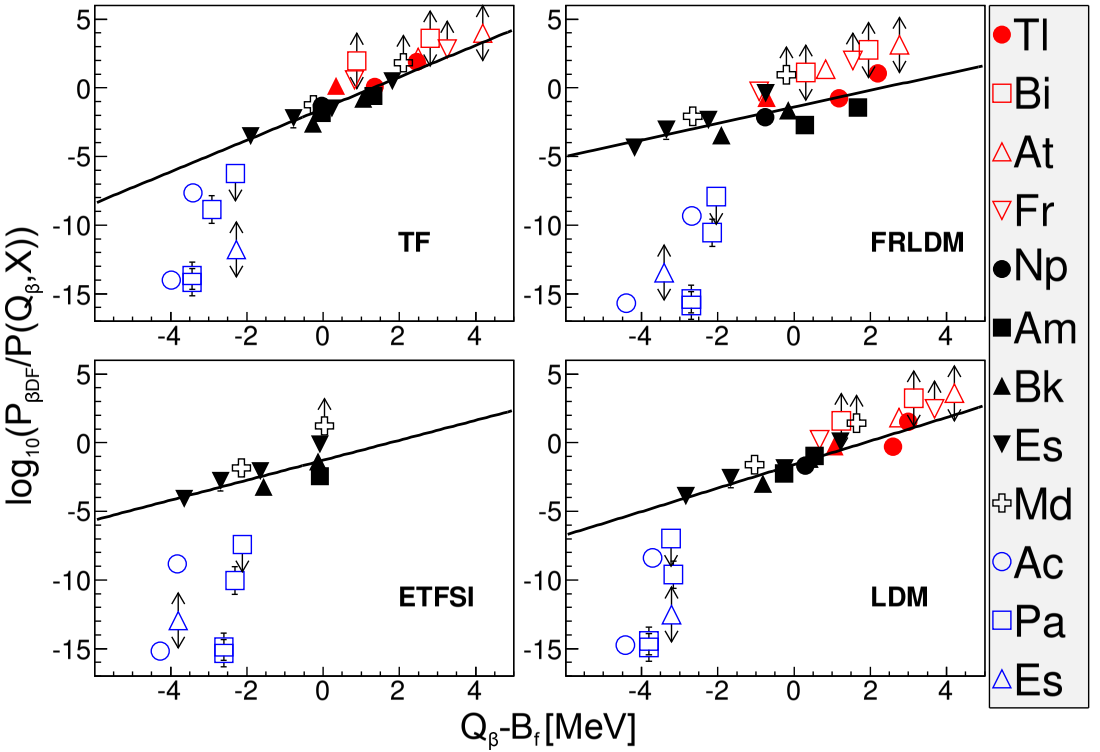

Figure 6.6: (In color) Plots of $\log_{10}(P_{\beta\mathrm{DF}}/(P(Q_\beta, X)$ versus $(Q_\beta - B_\mathrm{f})$ for different fission models as listed in Tables 6.1, 6.2 and 6.3. The closed symbols, representing 12 reliable values for $P_{\beta\mathrm{DF}}$ (see text for more details) are used for a linear fit with equal weights to the data points. Other data are indicated by the open symbols. The color code represents the different regions of the nuclear chart for which βDF has been experimentally observed: the neutron-deficient lead region (red), the neutron-deficient (black) and neutron-rich (blue) uranium region.

$$\lambda_{\beta\mathrm{DF}} \simeq \int_0^{S_n} S_\beta(E) F(Q_\beta - E) \frac{\Gamma_\mathrm{f}(E)}{\Gamma_\mathrm{tot}(E)} dE. \tag{6.25}$$

As in section 6.1.2, S_β is assumed equal to a constant C_1 and $\Gamma_\mathrm{f}/\Gamma_\mathrm{tot}$ is approximated by using equation 6.6. In addition, $F(Q_\beta - E)$ for neutron-rich isotopes is given by equation 6.19. $\lambda_{\beta\mathrm{DF}}$ is thus given by

$$\lambda_{\beta\mathrm{DF}} \simeq D e^{X(Q_\beta - B_\mathrm{f})} \int_0^{S_n} (Q_\beta - E)^5 e^{-X(Q_\beta - E)} dE, \tag{6.26}$$

whereby $D = C_1 C_2'' C_3$. Substituting $u = X(Q_\beta - E)$ and adjusting the integration borders correspondingly yields

$$\lambda_{\beta\mathrm{DF}} \simeq \frac{D e^{X(Q_\beta - B_\mathrm{f})}}{X^6} \int_{X(Q_\beta - S_n)}^{X(Q_\beta)} u^5 e^{-u} du. \tag{6.27}$$

The integral in equation 6.27 can also be written as

$$\int_{X(Q_\beta - S_n)}^{X(Q_\beta)} u^5 e^{-u} du = \int_0^{XQ_\beta} u^5 e^{-u} du - \int_0^{X(Q_\beta - S_n)} u^5 e^{-u} du. \tag{6.28}$$

Applying the definition of the incomplete Γ function in equation 6.10 gives

$$\lambda_{\beta\mathrm{DF}} \simeq \frac{D\Gamma(6)}{X^6} e^{X(Q_\beta - B_\mathrm{f})} [\Gamma(6, XQ_\beta) - \Gamma(6, X(Q_\beta - S_n))]. \tag{6.29}$$

As indicated in section 6.2, $\Gamma(6, XQ_\beta) \simeq 1$ for Q_β values of a few MeV. One can therefore write

$$\lambda_{\beta\mathrm{DF}} \simeq \frac{D\Gamma(6)}{X^6} e^{X(Q_\beta - B_\mathrm{f})} [1 - \Gamma(6, X(Q_\beta - S_n))]. \tag{6.30}$$

The function $1 - \Gamma(6, X(Q_\beta - S_n))$, plotted in Figure 6.7, only drops below 0.1 for $X(Q_\beta - S_n) \approx 9$. From this analysis, it thus seems that neutron emission will only appreciably influence $\lambda_{\beta\mathrm{DF}}$ (more than one order of magnitude) for Q_β values at least $2 - 3$ MeV higher than S_n, thereby assuming values of the exponent X around $2 - 3$. The nuclei in Figure 1.2 to the right of the dashed line are expected to have Q_β values which are at least 3 MeV above S_n. The systematic trends presented in sections 6.1 and 6.2 may thus be employed to

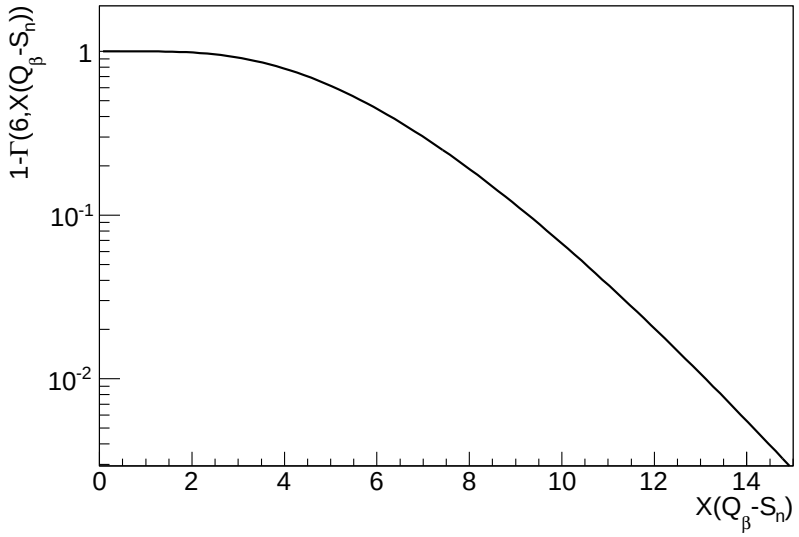

Figure 6.7: The function $1 - \Gamma(6, X(Q_\beta - S_n))$, which appears in the phenomenological description of $\lambda_{\beta\mathrm{DF}}$, given in equation 6.30, for neutron-rich nuclei with $Q_\beta > S_n$.

estimate the βDF probability or partial half-life for a significant amount of heavy and superheavy (neutron-rich) nuclei, situated up to 20 nucleons away from β stability. For the most neutron-rich nuclei however, β-delayed neutron emission should be considered in the analysis.

Chapter 7

Conclusions and Outlook

7.1 Conclusions

Following the recent discovery of asymmetric fission in the βDF of ^{180}Tl [3, 47], different neutron-deficient isotopes in the region between $Z = 80$ and 86 have been studied. This region covers the transition between the asymmetric fission around ^{180}Hg and symmetric fission around ^{204}Rn. Both mass and total kinetic energy distributions were measured.

More specifically, in this work we report on the fission properties of ^{194,196}Po and ^{200,202}Rn, which were studied by means of β-delayed fission (βDF). Relatively pure beams of the βDF precursors ^{194,196}At and ^{200,202}Fr were produced at the online separator ISOLDE, situated in CERN (Geneva, Switzerland) and implanted on a thin carbon foil. Subsequent detection of fission fragments was performed by silicon detectors placed on either side of this foil.

The fission-fragment mass distributions, resulting from the βDF of ^{194,196}At and ^{202}Fr, showed a triple-humped structure. In the case of ^{194,196}At, a narrow symmetric mass distribution was observed for fragments with a higher TKE. Conversely, a broader, possibly asymmetric, structure was found for the fission products with lower TKE. These findings thus indicate a new region of multimodal fission in this scarcely studied (in terms of fission) zone of the nuclear chart.
These results were compared with the macroscopic-microscopic finite-range liquid-drop model (FRLDM) and a self-consistent approach employing the Gogny D1S energy density functional. Potential energy surfaces (PES), generated

within the framework of either model, show a broad and flat plateau with numerous weakly pronounced valleys and ridges. Such features make it challenging to uniquely ascribe fission paths, as compared to the actinide region where strong structures in the PES determine the resulting mass distributions. Indeed, clear discrepancies were observed with theoretical calculations from FRLDM, predicting a gradual decrease of the mass split in the transition from asymmetry in ^{180}Hg to symmetry in ^{204}Rn. These results thus demonstrate once more the need for dynamical fission calculations, and may serve as a benchmark for further theoretical developments.

Next to fission-fragment mass and energy distributions, also the corresponding branching ratio for βDF can be extracted with the current experimental setup. The newly obtained data in the neutron-deficient lead region from this work, in combination with literature data, enable a systematic study of βDF branchings for a wide variety of nuclei. This comparison showed that βDF partial half-lives depend exponentially on the difference of Q_β and fission-barrier energies. Moreover, this dependence could be inferred from simple theoretical calculations. A similar trend was also observed for β-delayed fission probabilities. This simple functionality of the partial βDF half-life can also be used in regions of the nuclear chart where experimental studies are prohibited by the limited production rates.

7.2 Outlook

As pointed out in this work, both a ground and an isomeric level of ^{194}At and ^{202}Fr with similar half-lives were produced during the βDF experiments on these isotopes at ISOLDE-CERN. Although the excitation energy of the isomer is most likely only a few hundred keV, it is believed to have a different spin and parity as compared to the ground state [124], which could lead to different βDF properties. With the current experimental technique however, it remained undetermined to which of these states β-delayed fission fragments should be ascribed. An isomeric separation of these βDF precursors is feasible using selective resonant laser-ionization techniques and would provide a unique experimental way to study possible spin and parity dependence of fission. For example, the recently installed Collinear Resonance Ionization Spectroscopy (CRIS) can be employed to determine separate βDF branching ratios for the ground and isomeric state [127].

Due to the emergence and continuous improvement of experimental facilities and techniques, increasingly exotic nuclei have and will become available for βDF research. For example, a recent measurement at the GAs-filled Recoil Ion Separator (GARIS) [155] setup in RIKEN has successfully identified βDF in the

neutron-deficient ^{230}Am nucleus. In this experiment, ^{230}Am was produced by the fusion-evaporation reaction $^{27}\mathrm{Al} + ^{207}\mathrm{Pb} \rightarrow ^{230}\mathrm{Am} + 4n$. After separation by GARIS, newly created ions are identified by a time-of-flight detector and implanted in a segmented Si-box detector, used for the detection of βDF events. The installation of the ISOLDE Decay Station (IDS) [156] allows an efficient detection of α, β and γ particles, as well as fission fragments, originating from short-lived radioactive species. Using this setup, the βDF of the neutron-rich ^{228,230,232}Fr isotopes, primarily decaying via β^- decay, can be studied.

In August 2012, a novel approach was employed at the FRS at GSI to study the electromagnetically-induced fission of nuclei ranging from ^{183}Hg to ^{238}Np. These so-called SOFIA (Studies On FIssion with ALADIN) experiments combine an ionization chamber with a large-acceptance dipole magnet for the simultaneous identification of both charge and mass of emitted fission fragments. It would be interesting to compare data from this experimental campaign with βDF studies from this and previous work, since both techniques probe fission at excitation energies around the fission barrier, although the excitation mechanisms are vastly different.

In the more distant future, next-generation high-intensity ISOL facilities, such as the Rare Elements in-Gas Laser Ion Source and Spectroscopy (REGLIS) device at the S3 spectrometer (GANIL, France) [157, 158] or the ISOL@MYRRHA facility (SCK•CEN, Belgium) [159], will be constructed. Experimental campaigns at such facilities may increase the statistics for βDF data in the neutron-deficient lead region by several orders of magnitude as compared to the ISOLDE campaigns. Such experiments can thus serve to determine fission-fragment mass distributions of nuclides for which only a few βDF events were detected at ISOLDE, such as ^{178}Tl or ^{200}Fr. In addition, detailed features in the βDF mass distributions of e.g. ^{180}Tl, ^{194,196}At or ^{202}Fr can be identified if a higher fission-fragment rate is available. For example, the dependence of fission-fragment masses with respect to their TKE can be investigated in detail, or possible odd-even staggering effects in the mass and element distributions can be identified. Moreover, these new-generation ISOL facilities may allow the study of βDF properties in increasingly neutron-rich isotopes, situated towards the region of importance for the fission-recycling in the r-process.

As mentioned in this work, considerable progress was made in fission calculations over the past decades. For example, multi-dimensional potential-energy landscapes can now be constructed at various (static) nuclear deformations. Nonetheless, data from this work and other fission studies have indicated several discrepancies with contemporary models. Further theoretical developments, for example by including dynamical effects, may thus greatly advance our

understanding of the fission process.

Appendix A

Detector calibration for fission fragments at ILL

A.1 Introduction

As described in section 4.4.1, silicon detectors suffer from the so-called pulse height defect (PHD) when recording fission fragments. The signal from an incoming heavy ion or fission fragment depends not only on its energy, but also on other properties, such as its atomic number Z and mass number M.
In the 1960's, Schmitt et al. [110] studied the response of Si detectors for bromine and iodine ions. They proposed the simple empirical formula, given by equation 4.11, describing the calibration for fission fragments detected with silicon surface barrier detectors.
A method to determine the calibration constants A, A', B, B', by only using the peak positions P_L,P_H (in channels) of a ^{252}Cf FF energy spectrum, was also presented:

$$\begin{aligned} A &= A_0/(P_L - P_H), \\ A' &= A'_0/(P_L - P_H), \\ B &= B_0 - AP_L, \\ B' &= B'_0 - A'P_L. \end{aligned} \tag{A.1}$$

The so-called Schmitt constants A_0, A'_0, B_0 and B'_0 are supposed to be universal for a given type of detector. Schmitt and co-workers found indeed numerical values for these constants, valid for Silicon Surface Barrier (SSB) detectors. In

Table A.1: Specifications of the silicon detectors under investigation. For each detector, the manufacturing company, serial number, depletion depth ('DD'), active area ('AA'), operational bias voltage and the type (PIPS or SSB) are listed.

Company	Serial number	DD (μm)	AA (mm^2)	Bias (V)	PIPS/SSB
ORTEC	43-051F	$\sim$300	450 [a]	100	SSB
ORTEC	49-186B	$\sim$500	300	120	SSB
ORTEC	47-038D	316	300	120	SSB
Canberra	74-256	303	300	60	PIPS
Canberra	74-257	303	300	60	PIPS

[a] including the hole, having a diameter of 8 mm

1986, Weissenberger et al. re-evaluated these constants for a specific type of surface barriers by using mass- and energy-separated fission fragments from the Lohengrin spectrometer at the Institut Laue-Langevin (ILL) [29]. They found that, by using the original Schmitt constants, fission-fragment kinetic energies were systematically over-estimated by $1-2$ %. Weissenberger and co-workers adjusted these constants in order to have a consistent calibration.

Since Weissenberger et al. only investigated a very specific type of SSB detectors (ORTEC F-series, active area of 100 mm^2), one can raise questions about the validity of these adjusted Schmitt constants for other, more modern SSB detectors and a fortiori for Passivated Implanted Planar Silicon (PIPS) detectors. In order to have a reliable calibration of FF energies and masses during the βDF measurements at ISOLDE-CERN, it was decided to perform a calibration, similar to the one described in [29]. Five detectors, including two PIPS detecors, one annular SSB and two cylindrical SSB detectors were tested. Their properties are summarized in table A.1.

These calibration measurements took place at the Lohengrin spectrometer in ILL in September 2011. The measurements allowed to verify relation 4.11 for FFs and determine the constants A, A', B, B' for various detector types. In addition, the detector response with respect to FFs of grazing incidence has been studied.

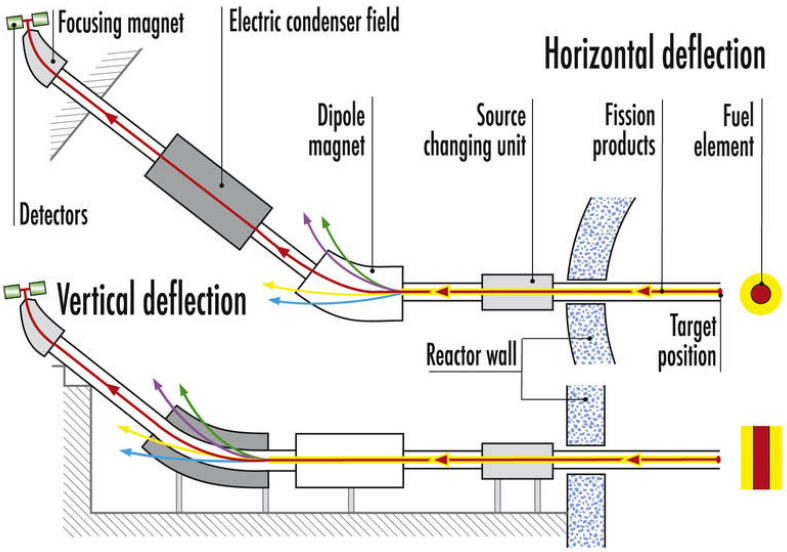

Figure A.1: (In color) A schematic representation of the Lohengrin spectrometer at ILL. Figure taken from [160]

A.2 Experimental setup at the Lohengrin spectrometer at ILL

The Insitut Laue-Langevin (ILL) operates one of the most intense reactor-based neutron sources in the world. These neutrons can be used to initiate fission in fissile target material, placed outside the reactor core. In this case, a ^{235}U target on a Ni-Ti backing was used. The produced fission fragments can then be separated by the Lohengrin spectrometer. Here, fragments can be selected on their mass to charge A/Q and energy to charge E/Q ratios using a combination of a dipole magnet and an electrostatic deflector, see Figure A.1. The typical energy resolution for the fission fragments is expected to be around 100 keV [29].

The silicon detector was mounted at the focal plane of the Lohengrin spectrometer on a rotatable holder. A ^{241}Am calibration source was placed downstream of the detector with respect to the beam direction. Turning the detector by 180° allows to record either FFs or α particles from the ^{241}Am source, without breaking the vacuum. A FF energy spectrum obtained by one

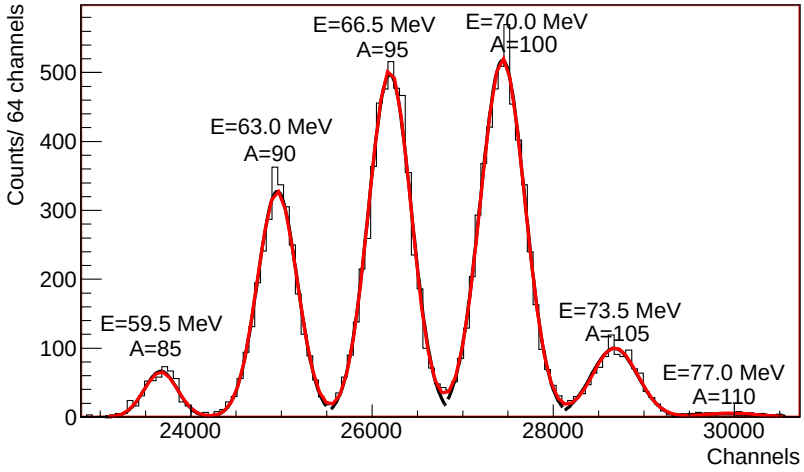

Figure A.2: A typical fission-fragment energy spectrum obtained by the SSB silicon detector with serial number 47-038D. The A/Q ratio and the E/Q ratio of the fragments equal 5 and 3.5 respectively and 6 calibration points can be extracted from this spectrum. The fission fragments were impinging perpendicular to the detector surface. A Gaussian fit of the peaks is shown in red. From this particular fit, peak positions at channels 23670(9), 24954(4), 26195(4), 27442(4), 28681(9) and 29954(54) were extracted.

of the silicon detectors, corresponding to a given A/Q and E/Q ratio of the fragments, is shown in figure A.2. Note that, since the charge state of the separated fragments may vary, different calibration points can be obtained with a single measurement.

A.3 Calibration procedure and results

Figure A.3 shows a set of data points, obtained by Gaussian fits on spectra similar to the one shown in Figure A.2, for detector 49-186B (SSB type). For the other detectors, similar data were obtained. Observed fission-fragment masses range from 80 to 149 amu and energies from 20 to 100 MeV. For each mass separately, an approximate linear dependence was observed, consistent with equation 4.11.
A calibration line for α particles, originating from the ^{241}Am source and from ternary fission of ^{235}U, could also be determined. ^{48}Ti or ^{60}Ni ions, which were sputtered from the backing of the target, were observed as well. Since the latter

ions have a significantly lower mass as compared to typical fission fragments, they have been excluded from the calibration procedure described further.

Since fission fragments have rather high mass numbers M and energies E (see Figure A.3), the calibration equation 4.11 used for fitting the data points was slightly modified to

$$E = (A + A'(M - M_0))(X - X_0) + B + B'(M - M_0). \tag{A.2}$$

X_0 and M_0 are fixed constants equal to the respective mean pulse height and mass of the fitted data set. Similarly, the α-calibration line is given by

$$E_\alpha = a(X - X'_0) + b. \tag{A.3}$$

The results from the fits are shown in table A.2 for each of the detectors separately and correspond to a perpendicular incidence of fission fragments with respect to the detector surface.

The PHD of an incoming ion can be estimated, by comparing its energy E with the α-calibration line given in equation A.3, as

$$\text{PHD} = E - a(X - X'_0) + b, \tag{A.4}$$

where X is the recorded pulse height and a and b are taken from Table A.2. Figures A.4 and A.5 show the PHD of the SSB and PIPS detectors respectively for a subset of the available data. The fitted PHD, deduced from the calibration equation A.2 and the corresponding constants in Table A.2, shows a good agreement with the experimental data points for both SSB and PIPS detectors. The PIPS detectors exhibit a very similar behavior of the PHD with respect to each other, which could be expected, since their serial numbers only differ by one digit. The PHD observed in these detectors is larger than in SSB detectors by about $0.5 - 1$ MeV.
Figure A.4 shows that the cylindrical and annular SSB detectors with numbers 49-186B and 43-051F respectively display a very similar behavior. The PHD recorded by detector 47-038D, however, shows significant differences, such as a decreasing behavior for mass 85.

Further characterization measurements on these detectors were performed at SCK•CEN (Mol, Belgium) in February 2012 using a ^{252}Cf fission source. A detailed investigation of the α spectra measured during these campaigns, see Figure A.6, showed that the fission source was severely contaminated by ^{250}Cf

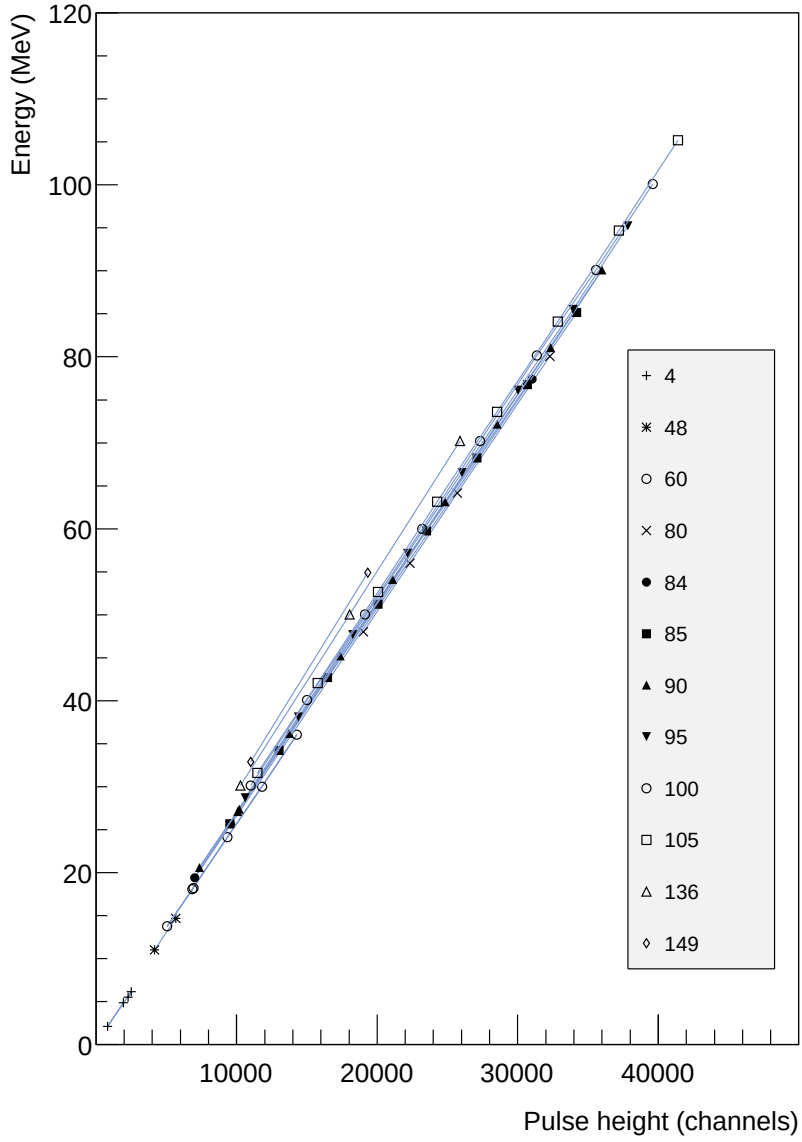

Figure A.3: The different data points obtained by the detector with serial number 49-186B. Data points corresponding to the same mass numbers are indicated by the same symbol, given in the legend, and are connected by straight lines. Next to fission fragments and α particles, also ^{48}Ti or ^{60}Ni ions, sputtered from the backing of the ^{235}U target, were recorded. The error bars corresponding to the data points are much smaller than the dimensions of the markers.

Table A.2: The calibration constants for each of the 5 detectors as given by equations A.2 and A.3. The constants M_0 and X_0 were kept fixed during the fit and taken as the mean of the respective masses and pulse heights of the corresponding data sets.

	47-038D	49-186B	43-051F	74-256	74-257
a (MeV^{-1})	$2.418(4) \times 10^{-3}$	$2.405(8) \times 10^{-3}$	$2.484(8) \times 10^{-3}$	$2.42(2) \times 10^{-5}$	$2.421(7) \times 10^{-3}$
b (MeV)	6.295(2)	4.593(3)	4.589(3)	$4.298(9) \times 10^{-3}$	4.594(3)
X_0' [a]	2611.6	1904.5	1835.7	1770.9	1897.2
A (MeV^{-1})	$2.410(2) \times 10^{-3}$	$2.437(2) \times 10^{-3}$	$2.526(2) \times 10^{-3}$	$2.486(3) \times 10^{-3}$	$2.486(2) \times 10^{-3}$
A' (MeV^{-1})	$2.7(1) \times 10^{-6}$	$2.4(2) \times 10^{-7}$	$2.4(2) \times 10^{-7}$	$3.5(4) \times 10^{-7}$	$3.1(2) \times 10^{-6}$
B (MeV)	72.70(1)	56.72(2)	55.20(2)	50.74(3)	54.76(2)
B' (MeV)	0.101(1)	0.086(2)	0.085(1)	0.084(3)	0.087(2)
M_0 [a]	95.57	95.7	97.11	96.66	96.77
X_0 [a]	28782.4	22131.3	20709.7	19163.9	20780.0

[a] Parameter kept fixed during fit.

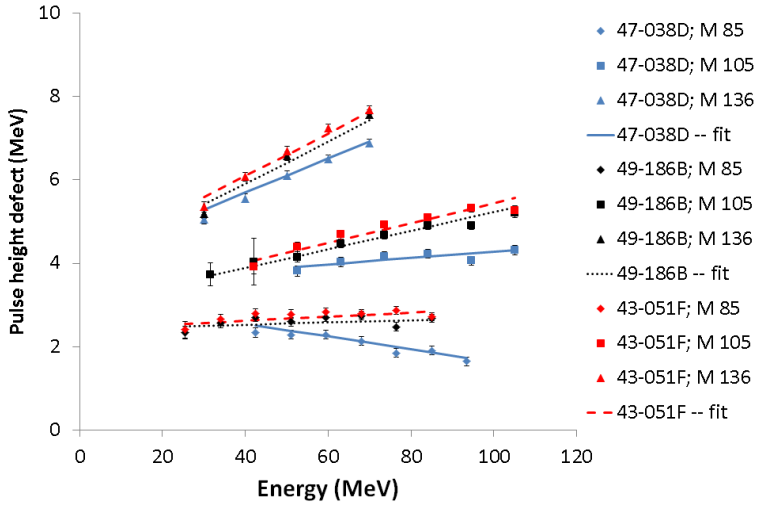

Figure A.4: The PHD defined by formula A.4, for M equal to 80,105 and 136, is shown for the surface barrier detectors with serial numbers 47-038D, 49-186B and 43-051F (annular). The straight lines show the behavior of the fitted PHD, obtained by calculating the energy of the fragment E from equation A.2, whereby the values of the constant are given in Table A.2.

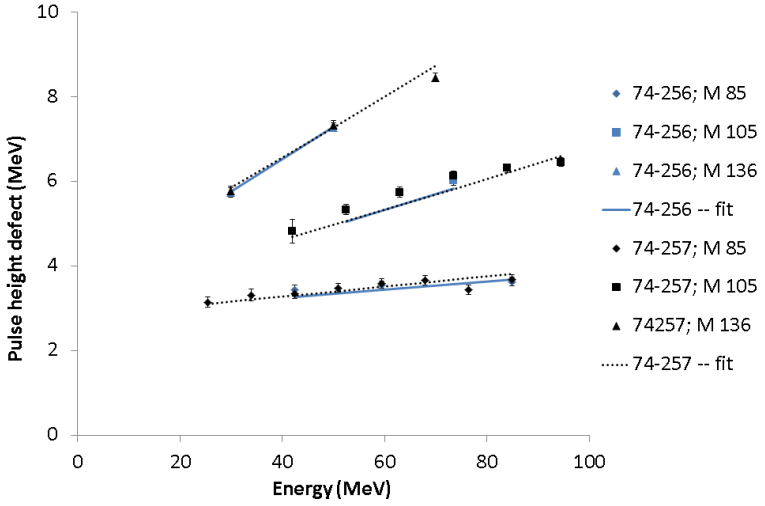

Figure A.5: Similar to Figure A.4, but now for the PIPS detectors 74-256 and 74-257.

Table A.3: The positions of the low (E_L) and high-energy (E_H) peak of the FF energy spectra, measured during the SCK•CEN run in February 2012 with a Cf fission source (see Figure A.5). The peak centroids were determined, by a double-Gaussian fit, for the different detectors used in the ILL calibration run in September 2011. The energy calibration was performed by using the observed α-decay lines originating from the source.

detector (type)	E_L (MeV)	E_H MeV)
47-038D (SSB)	66.2(1)	93.6(1)
43-051F (SSB)	66.0(1)	93.2(1)
49-186B (SSB)	66.2(1)	93.7(1)
74-257 (PIPS)	64.3(1)	91.7(1)
74-256 (PIPS)	64.5(1)	91.4(1)

and to a lesser extent by ^{249,251}Cf. In fact, about 1/5 of the recorded fission fragments originate from the spontaneous fission of ^{250}Cf. In addition, the fission source was covered by a thin polymide foil ($51\,\mu g/cm^2$) to prevent contamination of the silicon detectors. A reliable comparison with the revised constants Schmitt calibration constants from [29], by using equation A.1, was thus not possible.

A relative comparison of the detectors' response to FFs was feasible by extracting the peak positions of the FF energy spectrum from a double-Gaussian fit on the uncalibrated data. The energy values given in Table A.3 were then determined from the corresponding α-energy calibration. This table shows comparable values for the SSB and the PIPS detectors, suggesting a similar PHD for detectors of the same type. A higher PHD is observed for PIPS detectors as compared to SSB detectors, as is also apparent from Figures A.4 and A.5.
Figure A.4 shows a different behavior of the PHD for detector 47-038D with respect to the other SSB detectors 49-186B and 43-051F, in contradiction with the results from Table A.3. Since the detector 47-038D was calibrated first at ILL, several test runs with fission fragments were performed, which may have induced temporary radiation damage. This effect could have led to a different response of the detector to fission fragments and/or α particles, resulting in a systematic shift of the calibration by 0.5 MeV. The calibration constants from detector 49-186B were therefore used in the extraction of FF masses and energies in the ISOLDE βDF experiments, described in section 4.4.1.

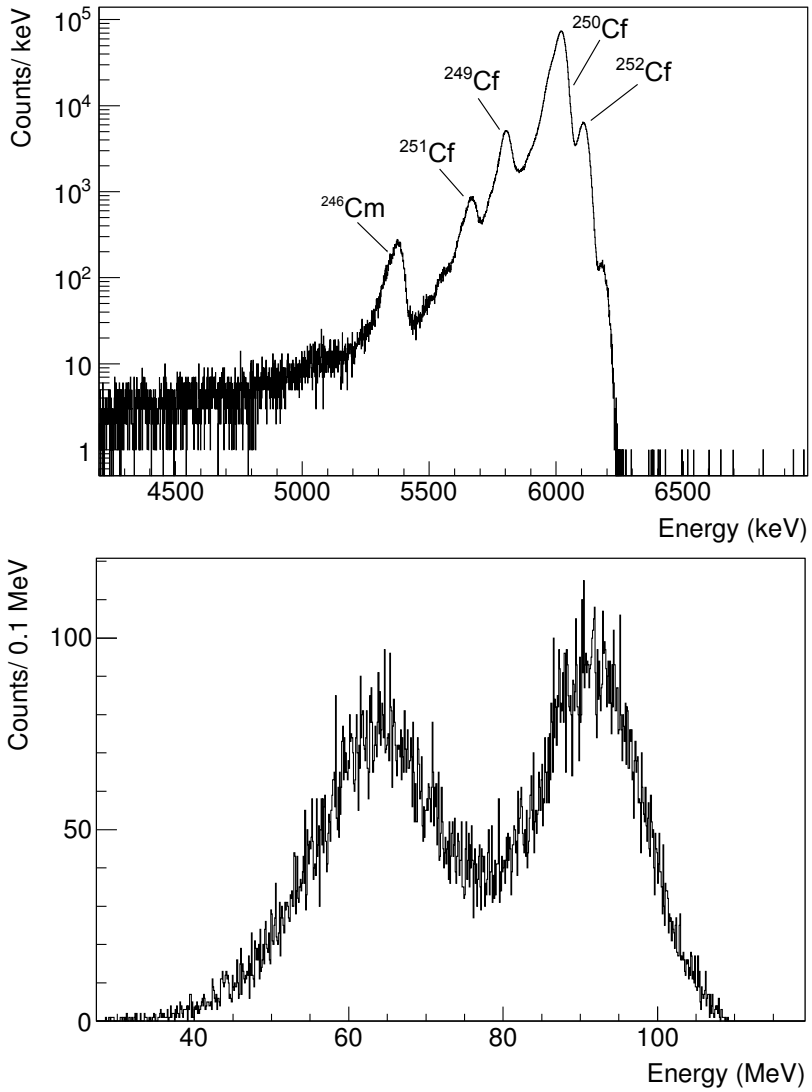

Figure A.6: Energy spectrum as recorded by silicon PIPS detector 74256 during measurements on a ^{252}Cf fission source at SCK•CEN. The upper part of the figure shows the corresponding α spectrum, demonstrating a severe contamination of ^{250}Cf in the fission source. The fission-fragment energy spectrum, using the energy calibration from the observed α lines, is shown in the lower part of the figure.

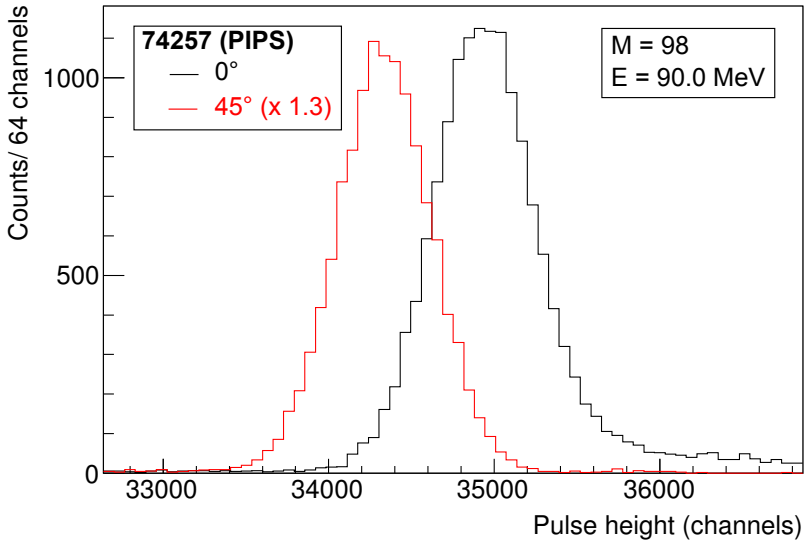

Figure A.7: Measured pulse-height spectrum for FFs with mass number $M = 98$ and an energy E of 90.0 MeV impinging on the PIPS detector 74-257 with an incident angle of 0° (black color) or 45° (red). The latter spectrum was scaled by a factor of 1.3.

A.4 Angular dependence of the pulse height defect

The results discussed in this appendix until now only include measurements for perpendicular incidence of fission fragments on the detector surface. As shown by Figure 4.11, detected fission fragments in ISOLDE hit the detector with a mean incident angle of 44°. Therefore, measurements at ILL were performed whereby the rotatable holder of the detector was placed at an angle of 45° with respect to the beam axis. A construction involving a mirror and a laser pointer ensured that this grazing angle was reproducible for measurements on the different detectors. Figures A.7 and A.8 compare the measured pulse height for FFs, having $E = 90\,\text{MeV}$ and $M = 90$, at perpendicular and 45° angle of incidence.

For the PIPS type detector with number 74-257 (Figure A.7), the difference between the centroid positions for 0° and 45° is 611(4) channels, corresponding to an energy difference $\Delta E_{0°-45°,\text{exp}}$ of 1.5 MeV. Similar measurements on FFs with other energies and masses show that $\Delta E_{0°-45°,\text{exp}}$ for both investigated

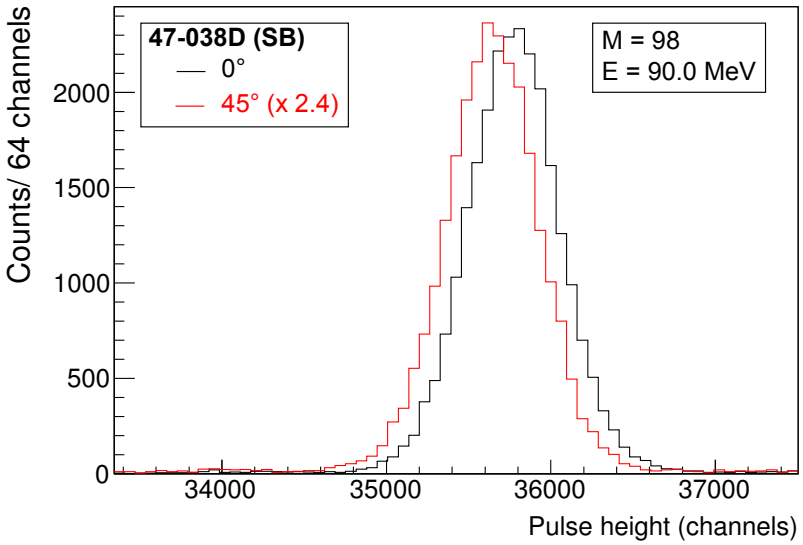

Figure A.8: Similar to FigureA.7, but in this case the spectra were recorded by the SSB type detector with serial number 47-038D.

PIPS detectors varies between 0.5 and 1.5 MeV. The observed shift in pulse height for SSB type detectors was observed to be much smaller, as evidenced by Figure A.8 for detector 47-038D. In this case, a shift of 129(3) channels, corresponding to $\Delta E_{0°-45°,\mathrm{exp}} = 0.3\,\mathrm{MeV}$ was observed. Other measurements with different SSB detectors, FF energies and masses show also shifts of typically 0.3 MeV, significantly lower than for PIPS detectors. However, according to the detector specifications (see [161] and [162]), PIPS detectors should have an entrance window almost half as thin as compared to SSB detectors. The observed energy shift $\Delta E_{0°-45°,\mathrm{exp}}$ is thus expected to be *smaller* for PIPS detectors, in contrast to the measurements.

In general, the energy loss E'_θ, in the dead layer with thickness t, of ions having an initial energy E and an incident angle θ with respect to the detector surface, is expressed by

$$E'_\theta = S_x(E, Z, M)t/\cos\theta. \tag{A.5}$$

The energy loss per unit of distance is denoted by the stopping power $S_x(E, Z, M)$, and is specific to the material x of the layer and E, Z and

Table A.4: The expected difference in energy loss $\Delta E_{0^\circ-45^\circ,\mathrm{calc}}$ for 90 MeV ^{98}Y nuclei with a grazing angle of 45° with respect to ions impinging perpendicular on the detector surface. $\Delta E_{0^\circ-45^\circ,\mathrm{calc}}$ is calculated using equation A.6 with $S_{\mathrm{Si}}(90\,\mathrm{MeV},^{98}\mathrm{Y})= 8.44\,\mathrm{keV/nm}$ [115] and t_{eq} equal to a typical entrance-window thickness for PIPS [161] or SSB [162] detectors. The last column lists the measured $\Delta E_{0^\circ-45^\circ,\mathrm{exp}}$ values, derived from Figures A.7 and A.8.

Detector	t_{eq} (nm Si eq)	$\Delta E_{0^\circ-45^\circ,\mathrm{calc}}$ (MeV)	$\Delta E_{0^\circ-45^\circ,\mathrm{exp}}$ (MeV)
74-257 (PIPS)	<50	0.2	1.5
47-038D (SSB)	80	0.3	0.3

M of the incoming ion. The dead-layer thickness is often expressed in silicon equivalent (Si eq), equal to the thickness t_{eq} of a silicon layer which would cause the same energy loss inside the material. The expected difference of energy loss in the entrance window between an ion of perpendicular and grazing incidence $\Delta E_{0^\circ-\theta,\mathrm{calc}}$ can be written as

$$\Delta E_{0^\circ-\theta,\mathrm{calc}} = S_{\mathrm{Si}}(E,Z;M)t_{\mathrm{eq}}\left(\frac{1}{cos\theta}-1\right). \tag{A.6}$$

According to [161], the thickness of the entrance window for PIPS detectors should be less than 50 nm Si eq. For the SSB detectors used in the ILL calibration experiments, a window thickness of 80 nm Si eq is estimated [162]. In Table A.4, $\Delta E_{0^\circ-45^\circ,\mathrm{exp}}$ values from Figures A.7 and A.8 are compared to the expected energy loss in a typical dead-layer of SSB and PIPS detectors, expressed in Si eq. To this end, mono-energetic nuclei of ^{98}Y, the most probable FF of mass 98 produced in the neutron-induced fission of ^{235}U [107], were considered to impinge on a silicon layer. The calculated stopping power $S_{\mathrm{Si}}(90\,\mathrm{MeV},^{98}\mathrm{Y})$, according to [115], equals 8.44 keV/ nm.

In the case of SSB detectors, the calculated value for $\Delta E_{0^\circ-45^\circ,\mathrm{calc}}$ is close to the energy shift observed in Figure A.8. For the PIPS detectors the measured energy shift is a factor of 7 larger as compared to the calculated value. Later measurements in the IKS laboratories, using the PIPS detector 74257 with 5.486 MeV α particles from a ^{241}Am source, are consistent with an entrance window of $\sim 10^2$ nm, reasonably close to the advertised value in [161]. The effective dead layer thus seems considerably larger for heavy ions, as compared to lighter ions, such as α particles. Further dedicated dead-layer measurements with heavy ions are desired to clarify this issue.

A.5 Conclusions

In order to have a reliable energy calibration for fission fragments during the ISOLDE-CERN βDF campaigns (see [47, 74]), dedicated measurements were performed at the Lohengrin spectrometer in ILL. The response of five detectors was tested, including two PIPS, one annular and two cylindrical SSB detectors. For all of these detectors a linear dependence of the PHD on both mass and energy (see equation 4.11), as proposed by [110], was proven for typical FF energies and masses.

Detectors of the same type (SSB or PIPS) were found to exhibit a similar behavior with respect to the detection of FFs. The PHD for a FF with specific mass and energy was observed to be up to 1 MeV higher for PIPS detectors as compared to SSB detectors. These calibration measurements thus suggest that one set of Schmitt constants (see equation A.1) may describe the PHD for a specific type of detector, but will differ between SSB and PIPS detectors.

Since the detector was mounted on a rotatable holder, also the response of the detectors to FFs with grazing angle was investigated. More specifically, measurements were performed at an incident angle of 45 degrees with respect to the detector surface, nearly equal to the mean angle of incidence of FFs in the ISOLDE campaigns. In the case of SSB detectors, the shift of the recorded pulse height with respect to fragments of perpendicular incidence is consistent with the expected energy loss in the entrance window of the detector. Although having a thinner entrance window for light particles, the PIPS detectors exhibit a much larger shift in measured pulse height for FFs as compared to SSB type detectors, indicating a larger effective dead layer for heavy ions.

Appendix B

Logics and data communication in laser-spectroscopy experiments at ISOLDE

Apart from βDF and other decay studies, the 'Windmill' detection setup is also used in several in-source laser-spectroscopy experiments at ISOLDE (see for example [92, 163–165]). Such studies aim at investigating the atomic hyperfine structure of several isotopes by varying the frequency of one of the lasers from the Resonance Ionization Laser Ion Source (RILIS). The position of the resonances are determined by measuring the rate of ionized atoms for the isotope in question with respect to the laser.
The Windmill system is ideally suited to measure efficiently relative production rates of α-decaying exotic nuclei, for example in the neutron-deficient lead region. Moreover, by gating on different α energies, hyperfine spectra of ground and possible low-lying isomeric states can be extracted.

In practice, the output frequencies of the RILIS lasers are fixed for a certain amount of time, while the produced ions are mass separated and implanted in one of the carbon foils of the WM setup. In the meantime, α, β and γ particles, originating from the implanted isotopes of interest, are recorded by the silicon and germanium detectors. In order to have consistent measurements for each laser frequency, the duty cycle is synchronized with the PSB super cycle.

In the course of this PhD work, several in-source laser-spectroscopy studies were performed at ISOLDE on Hg (IS598), At (IS534-II, IS534-III), Au (IS534-II, IS534-IV) and Po (IS456-III) isotopes. With respect to earlier studies, a major upgrade on the data-exchange between the WM system and RILIS has been established, relying on a Labview-based communication system. This upgrade allows to record multiple variables during a laser scan, such as the average wavenumber and corresponding spread, the laser power and integrated proton current on the ISOLDE target. Furthermore, live α spectra as well as a preliminary hyperfine spectrum are provided during a scan.

The Figures B.1 and B.2 give the electronic scheme used for the data recording and synchronization with both the RILIS lasers and PSB SC. This scheme is largely based on the system described in [166]. As shown in Figure B.2, the signal of Si 1 is splitted in order to provide a live α signal to the labview system. Figure B.3 depicts a schematic view of the measurement duty cycle, governed by a series of clocks, depicted in Figure B.1. The SC pulse from the PSB is first delayed by a fixed amount of time to match with the arrival of a proton pulse to the ISOLDE target. If the RILIS laser are stabilized (indicated by the 'Laser OK' signal) and the WM is ready for operation (governed by the 'Master' clock) a new measurement cycle is started. The macro beamgate is then opened for a fixed amount of time, allowing beam implantation. After closing the beamgate, lasers are set to a new frequency, while the data acquisition (DAQ) may continue to measure the radioactive decay. After the DAQ is stopped, the wheel is turned and a new measurement cycle can start.
During a laser scan, the detector signals of Si 1 as well as the laser performance are monitored and recorded by the Labview system, of which the key variables are listed in Table B.1. Figure B.4 shows schematically how these variables change during a a typical laser scan.
During a scan, a text file is created with the corresponding variables for each step. Hyperfine spectra are then finally created by linking this file to the binary data file from the digital acquisition system for the detector signals ('DGF'). Table B.2 shows an example of the listed values in the recorded text file, corresponding to the schematically depicted measurement in Figures B.3 and B.4.

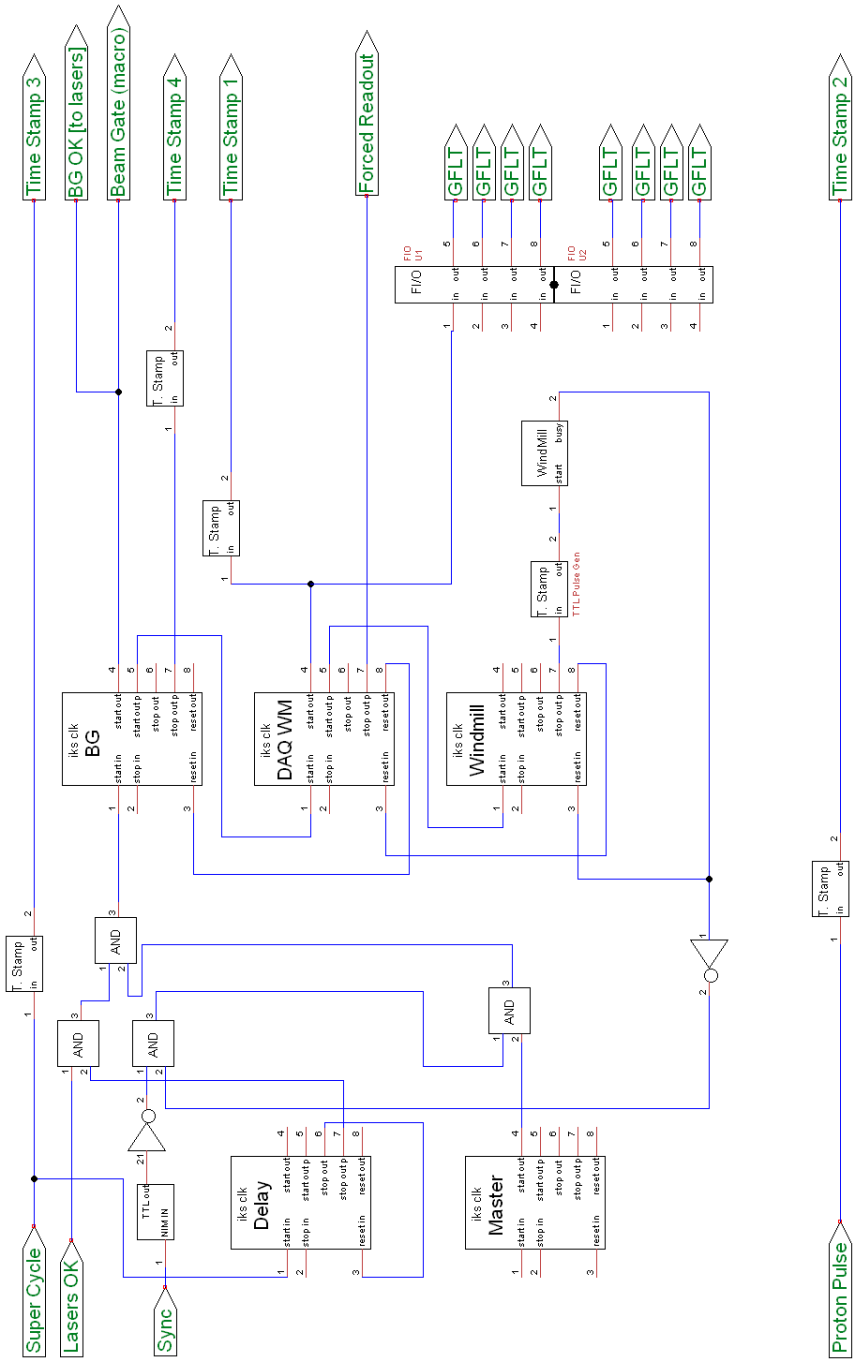

Figure B.1: (In color) Electronic scheme of the windmill detection system at ISOLDE.

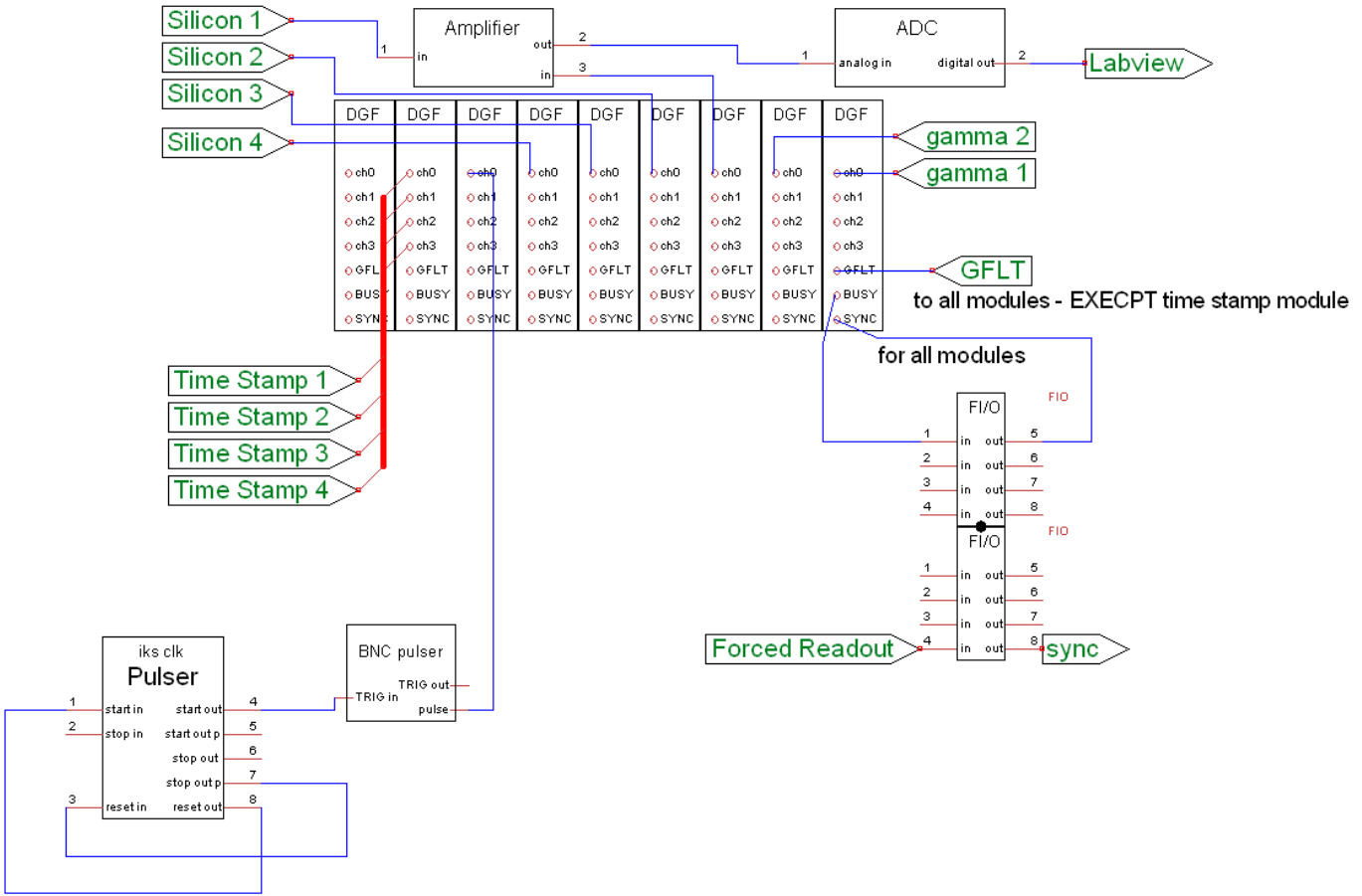

Figure B.2: (In color) Electronic scheme of the windmill detection system at ISOLDE. (Continued)

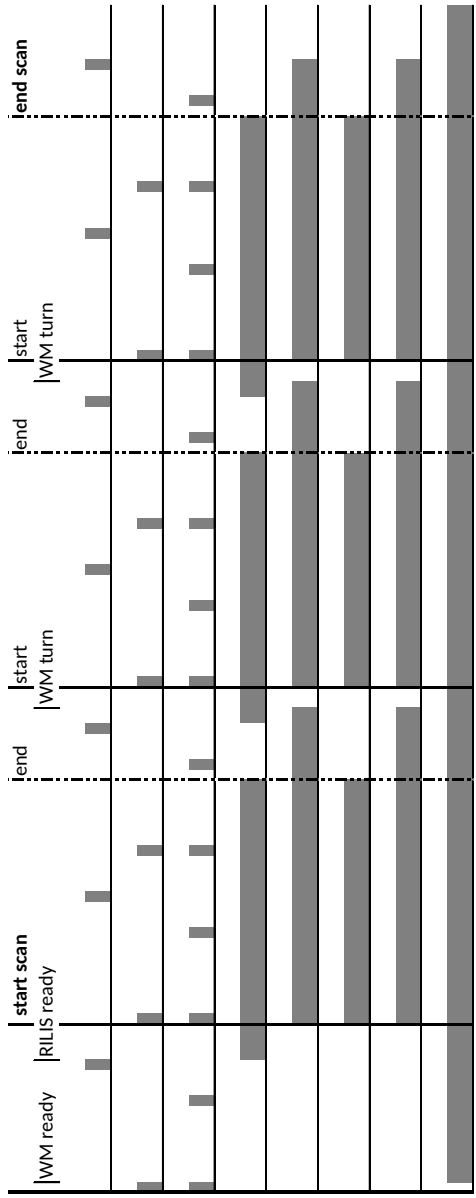

Figure B.3: Schematic view of a typical measurement duty cycle during laser-spectroscopy experiments at ISOLDE using the WM

Table B.1: Key variables used in the Labview system, responsible for the data communication between WM and RILIS. The different variables are characterized by their name, type and origin ('WM', 'RILIS' or 'PSB). A short description is also provided.

Name	Type	Origin	Description
Super Cycle	Boolean	PSB	Start PSB SC
Proton Pulse	Boolean	PSB	PP to ISOLDE target
protons per pulse	Double	PSB	Total protons on target per pulse
laser OK	Boolean	RILIS	'True' when RILIS laser stabilized
Scan Complete	Boolean	RILIS	'True' when RILIS scan finished
TimeStamp	Timestamp	RILIS	Start of new data point
wvnum request	Double	RILIS	Requested wavenumber (in cm^{-1})
wavenumber	Double	RILIS	Averaged wavenumber (in cm^{-1})
StandardDev Wvnumber	Double	RILIS	Measured spread of wavenumber (in cm^{-1})
Laser Power	Double	RILIS	Averaged laser power
StepNumber	Integer	RILIS	Counter of data points
Beamgate WM	Boolean	WM	'True' when Beamgate WM open
Integral	Double	WM	Integrated α counts (online)
alpha spectrum	Array of Integers	WM	Live α spectrum (in channels)
From	Double	WM	Left integration border (in channels)
To	Double	WM	Right integration border (in channels)

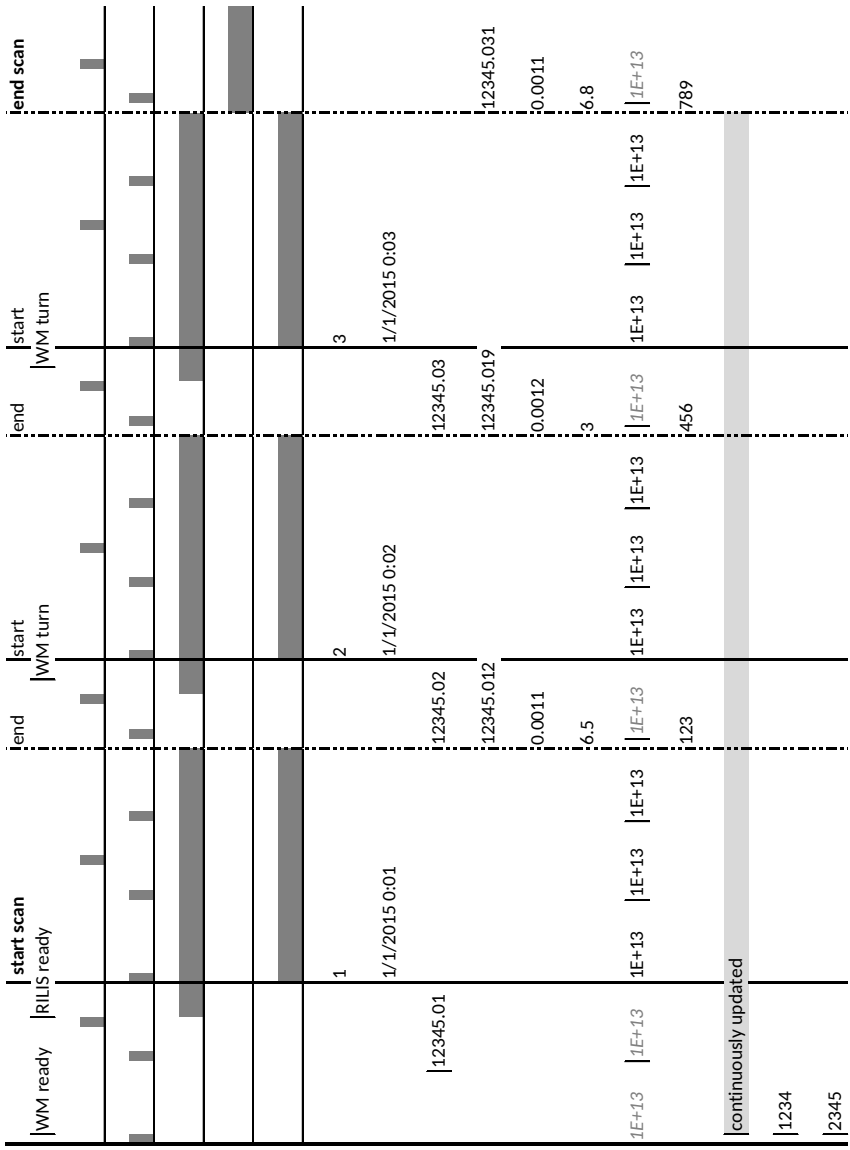

Figure B.4: Values of the variables listed in Table B.1 during a typical laser scan.

Table B.2: An example of the output text file corresponding to Figure B.4.

Date	Time	Step	wvnumber request	wavenumber	StandardDev	integral	total protons	Power
1/1/2015	0:01	1	12345.01	12345.012	0.0011	123	3×10^{13}	6.5
1/1/2015	0:02	2	12345.02	12345.019	0.0012	456	3×10^{13}	3
1/1/2015	0:03	3	12345.03	12345.031	0.0011	789	3×10^{13}	6.8

Appendix C

Search for βDF in ^{182}Tl

During the IS466-II ISOLDE campaign in July 2010, measurements were performed to search for the βDF decay of ^{182}Tl. This campaign employed the 'Windmill' (WM) detection setup, similar as the one described in chapter 3 but using different α detectors, for the detection of α, β, γ and fission particles. The ^{182}Tl beam with an intensity of 6×10^3 pps was produced in a similar way as reported in chapter 3 and [47]. A detailed description of this setup and the analysis of the α-decay data is provided in [167]. However, after 5.3 hours of dedicated measurements, no fission events were observed.
Similar to the case of ^{194}At and ^{202}Fr, the decay of at least one longer-living isomeric level of ^{182}Tl was observed together with the ground state. The difference in β-branching ratio, production rate and half-life between isomeric and ground-state level are currently unknown, but global properties can be derived. This appendix calculates the overall upper limit for the βDF partial half-life $T_{1/2\mathrm{p},\beta\mathrm{DF}}$ of ^{182}Tl by using the timing and energy information of detected α and γ particles. This experimental limit is also compared to the systematic behavior of $T_{1/2\mathrm{p},\beta\mathrm{DF}}$ values across the nuclear chart presented in section 6.1

The overall half-life $T_{1/2}$, a crucial variable for the extraction of $T_{1/2\mathrm{p},\beta\mathrm{DF}}$, was determined at 1.9(1)s by using the timing behavior of α particles originating from ^{182}Tl [167]. The overall α-branching ratio can be estimated by comparing the amount of observed β and α decays from ^{182}Tl. The latter was determined from the $3.676(6) \times 10^5$ α particles from ^{182}Tl detected in silicon detector Si 2, having a geometrical efficiency of 30 %. The number of β decays are inferred from the $3.879(9) \times 10^5$ observed γ transitions in Ge 2 of the $2^+ - 0^+$ transitions at 351 keV in the β-decay daughter ^{182}Hg. The detection efficiency (taking into

account the summing effect described in section 3.2) is estimated at 0.44(4)%. The relative amount of β decays of ^{182}Tl which are not followed by a γ photon from the 351 keV transition is estimated at 26(1)%. Using this information, a total amount of $1.2(1) \times 10^8$ β decays N_β of ^{182}Tl was calculated, exceeding the number of α decays by two orders of magnitude.
By considering that ^{182}Tl primarily undergoes β decay, $N_{\mathrm{dec,tot}}$ in equation 2.15 can be approximated by N_β and $T_{1/2\mathrm{p},\beta\mathrm{DF}}$ is given by

$$T_{1/2\mathrm{p},\beta\mathrm{DF}} = T_{1/2} \frac{N_\beta}{N_{\beta\mathrm{DF}}}, \tag{C.1}$$

A lower limit for the βDF partial half-life $T_{1/2\mathrm{p},\beta\mathrm{DF}}$ of $1.4(1) \times 10^8$ s was extracted by considering that less than one βDF fission event was observed. In a similar way, the upper limit for the βDF probability was found at $P_{\beta\mathrm{DF}} < 1.4(1) \times 10^{-8}$.

Using the Q_β values [94] and theoretical fission barriers of the daughter of ^{182}Hg from the TF [10], FRLDM [41] or LDM [141] model, $Q_\beta - B_\mathrm{f}$ values of -0.2, -0.6 and $+0.4$ MeV were obtained respectively. From the systematic behavior of $T_{1/2\mathrm{p},\beta\mathrm{DF}}$ with respect to $Q_\beta - B_\mathrm{f}$, presented in section 6.1, a $T_{1/2\mathrm{p},\beta\mathrm{DF}}$ value in the order of 10^5-10^6 s is expected for ^{182}Tl. The lower limit for $T_{1/2\mathrm{p},\beta\mathrm{DF}}$ in the βDF decay of ^{182}Tl is thus more than two orders of magnitude larger than the estimated values from systematics. This discrepancy might be caused, for example, by an unusually weak β-strength function at higher excitation energies, as compared to other nuclei in the neutron-deficient lead region. This hypothesis could be verified by experimentally measuring the β-strength function for ^{182}Tl and neighboring nuclei using total absorption spectroscopy (TAS) measurements.

Bibliography

[1] G. Audi, F. G. . Kondev, M. Wang, B. Pfeiffer, X. Sun, J. Blachot, and M. MacCormick, "The NUBASE2012 evaluation of nuclear properties," *Chinese Physics C*, vol. 36, no. 12, pp. 1157–1286, 2012.

[2] O. Hahn and F. Strassmann, "über den Nachweis und das Verhalten der bei der Bestrahlung des Urans mittels Neutronen entstehenden Erdalkalimetalle," *Die Naturwissenschaften*, vol. 27, pp. 11–15, Jan. 1939.

[3] A. N. Andreyev, J. Elseviers, M. Huyse, P. Van Duppen, S. Antalic, A. Barzakh, N. Bree, T. E. Cocolios, V. F. Comas, J. Diriken, D. Fedorov, V. N. Fedosseev, S. Franchoo, J. A. Heredia, O. Ivanov, U. Köster, B. A. Marsh, K. Nishio, R. D. Page, N. Patronis, M. Seliverstov, I. Tsekhanovich, P. Van den Bergh, J. Van De Walle, M. Venhart, S. Vermote, M. Veselsky, C. Wagemans, T. Ichikawa, A. Iwamoto, P. Möller, and A. J. Sierk, "New Type of Asymmetric Fission in Proton-Rich Nuclei," *Physical Review Letters*, vol. 105, p. 252502, Dec. 2010.

[4] V. Liberati, A. N. Andreyev, S. Antalic, A. Barzakh, T. E. Cocolios, J. Elseviers, D. Fedorov, V. N. Fedoseeev, M. Huyse, D. T. Joss, Z. Kalaninová, U. Köster, J. F. W. Lane, B. Marsh, D. Mengoni, P. Molkanov, K. Nishio, R. D. Page, N. Patronis, D. Pauwels, D. Radulov, M. Seliverstov, M. Sjödin, I. Tsekhanovich, P. Van den Bergh, P. Van Duppen, M. Venhart, and M. Veselský, "β-delayed fission and α decay of ^{178}Tl," *Physical Review C*, vol. 88, p. 044322, Oct. 2013.

[5] K.-H. Schmidt, S. Steinhäuser, C. Böckstiegel, A. Grewe, A. Heinz, A. R. Junghans, J. Benlliure, H. G. Clerc, M. de Jong, J. Müller, M. Pfützner, and B. Voss, "Relativistic radioactive beams: A new access to nuclear-fission studies," *Nuclear Physics A*, vol. 665, pp. 221–267, 2000.

[6] K.-H. Schmidt, J. Benlliure, and A. R. Junghans, "Fission of nuclei far from stability," *Nuclear Physics A*, vol. 693, no. 1-2, pp. 169–189, 2001.

[7] I. V. Panov, E. Kolbe, B. Pfeiffer, T. Rauscher, K.-L. Kratz, and F.-K. Thielemann, "Calculations of fission rates for r-process nucleosynthesis," *Nuclear Physics A*, vol. 747, pp. 633–654, Jan. 2005.

[8] I. Petermann, K. Langanke, G. Martínez-Pinedo, I. V. Panov, P. G. Reinhard, and F. K. Thielemann, "Have superheavy elements been produced in nature?," *The European Physical Journal A*, vol. 48, p. 122, Sept. 2012.

[9] S. Goriely, "The fundamental role of fission during r-process nucleosynthesis in neutron star mergers," *The European Physical Journal A*, vol. 51, p. 22, 2015.

[10] W. J. Myers and W. J. Swiateckii, "Thomas-Fermi fission barriers," *Physical Review C*, vol. 60, p. 014606, June 1999.

[11] P. Möller, J. R. Nix, W. D. Myers, and W. J. Swiatecki, "Nuclear ground-state masses and deformations," *Atomic Data and Nuclear Data Tables*, vol. 59, pp. 185–381, 1995.

[12] Y. Aboussir, J. M. Pearson, A. K. Dutta, and F. Tondeur, "Nuclear mass formula via an approximation to the Hartree-Fock method," *Atomic Data and Nuclear Data Tables*, vol. 61, pp. 127–176, Sept. 1995.

[13] A. Mamdouh, J. M. Pearson, M. Rayet, and F. Tondeur, "Fission barriers of neutron-rich and superheavy nuclei calculated with the ETFSI method," *Nuclear Physics A*, vol. 679, pp. 337–358, Jan. 2001.

[14] L. Meitner and O. R. Frisch, "Disintegraion of Uranium by Neutrons: a new Type of nuclear reaction," *Nature*, vol. 143, pp. 239–240, 1939.

[15] K. Krane, *Introductory nuclear physics*. John Wiley & Sons, Inc, 1988.

[16] H. V. Klapdor, "The shape of the beta strength function and consequences for nuclear physics and astrophysics," *Progress in Particle and Nuclear Physics*, vol. 10, pp. 131–225, Jan. 1983.

[17] R. B. Firestone, *Table of isotopes*. Wiley, 8 ed., 1999.

[18] V. I. Kuznetsov and N. K. Skobelev, "Delayed nuclear fission," *Physics of Particles and Nuclei*, vol. 30, p. 666, Nov. 1999.

[19] H. L. Hall and D. C. Hoffman, "Delayed Fission," *Annual Review of Nuclear and Particle Science*, vol. 42, pp. 147–175, Dec. 1992.

[20] I. N. Izosimov, V. G. Kalinnikov, and A. A. Solnyshkin, "Fine structure of strength functions for beta decays of atomic nuclei," *Physics of Particles and Nuclei*, vol. 42, pp. 963–997, Nov. 2011.

[21] M. Veselský, A. N. Andreyev, S. Antalic, M. Huyse, P. Möller, K. Nishio, A. J. Sierk, P. Van Duppen, and M. Venhart, "Fission-barrier heights of neutron-deficient mercury nuclei," *Physical Review C*, vol. 86, p. 024308, Aug. 2012.

[22] C. Wagemans, *The nuclear fission process*. 1991.

[23] N. Bohr and J. A. Wheeler, "The mechanism of nuclear fission," *Physical Review*, vol. 56, p. 426, 1939.

[24] H. Diehl and W. Greiner, "Ternary fission in the liquid drop model," *Physics Letters B*, vol. 45, pp. 35–37, June 1973.

[25] H. Diehl and W. Greiner, "Theory of ternary fission in the liquid drop model," *Nuclear Physics A*, vol. 229, pp. 29–46, Aug. 1974.

[26] S. Bjørnholm and J. E. Lynn, "The double-humped fission barrier," *Reviews of Modern Physics*, vol. 52, pp. 725–931, Oct. 1980.

[27] M. Mayer, "Nuclear Configurations in the Spin-Orbit Coupling Model. I. Empirical Evidence," *Physical Review*, vol. 78, pp. 16–21, Apr. 1950.

[28] Y. Zhao, I. Nishinaka, Y. Nagame, M. Tanikawa, K. Tsukada, S. Ichikawa, K. Sueki, Y. Oura, H. Ikezoe, S. Mitsuoka, H. Kudo, T. Ohtsuki, and H. Nakahara, "Symmetric and Asymmetric Scission Properties: Identical Shape Elongations of Fissioning Nuclei," *Physical Review Letters*, vol. 82, no. 17, pp. 3408–3411, 1999.

[29] E. Weissenberger, P. Geltenbort, A. Oed, and F. Gönnenwein, "Energy calibration of surface barrier detectors for fission fragments," *Nuclear Instruments and Methods in Physics Research A*, vol. 96, pp. 506–515, 1986.

[30] Y. Nagame and H. Nakahara, "Two-mode fission – experimental verification and characterization of two fission-modes," *Radiochimica Acta*, vol. 100, pp. 605–614, Aug. 2012.

[31] K. Nishio, H. Ikezoe, S. Mitsuoka, I. Nishinaka, Y. Nagame, Y. Watanabe, T. Ohtsuki, K. Hirose, and S. Hofmann, "Effects of nuclear orientation on the mass distribution of fission fragments in the reaction of ^{36}S + ^{238}U," *Physical Review C*, vol. 77, p. 064607, June 2008.

[32] E. Prasad, D. J. Hinde, K. Ramachandran, E. Williams, M. Dasgupta, I. P. Carter, K. J. Cook, D. Y. Jeung, D. H. Luong, S. McNeil, C. S. Palshetkar, D. C. Rafferty, C. Simenel, A. Wakhle, J. Khuyagbaatar, C. E. Düllmann, B. Lommel, and B. Kindler, "Observation of mass-asymmetric

fission of mercury nuclei in heavy ion fusion," *Physical Review C*, vol. 91, p. 064605, June 2015.

[33] K. Nishio, A. N. Andreyev, R. Chapman, X. Derkx, C. E. Düllmann, L. Ghys, F. P. Heß berger, K. Hirose, H. Ikezoe, J. Khuyagbaatar, B. Kindler, B. Lommel, H. Makii, I. Nishinaka, T. Ohtsuki, S. D. Pain, R. Sagaidak, I. Tsekhanovich, M. Venhart, Y. Wakabayashi, and S. Yan, "Excitation energy dependence of fragment-mass distributions from fission of ^{180,190}Hg formed in fusion reactions of ^{36}Ar + ^{144,154}Sm," *Physics Letters B*, vol. 748, pp. 89–94, Sept. 2015.

[34] G. N. Flerov and K. A. Petrzhak, "Spontaneous fission of uranium," *Physical Review*, vol. 58, pp. 275–279, 1940.

[35] I. Croall and J. Cuninghame, "Fragment distributions in the fission of 232Th by protons of energies 13 to 53 MeV," *Nuclear Physics A*, vol. 125, pp. 402–416, Mar. 1969.

[36] M. G. Itkis, V. N. Okolovich, and G. N. Smirenkin, "Symmetric and asymmetric fission of nuclei lighter than radium," *Nuclear Physics A*, vol. 502, pp. 243c–260c, 1989.

[37] M. G. Itkis, N. A. Kondrat'ev, S. I. Mul'gin, V. N. Okolovich, Y. A. Rusanov, and G. N. Smirenkin, "Mass asymmetry of symmetric fission of nuclei with A $\simeq$ 200," *Soviet Journal of Nuclear Physics*, vol. 52, no. 4, pp. 601–611, 1990.

[38] M. G. Itkis, N. A. Kondrat'ev, and S. I. Mul'gin, "Low-energy fission of nuclei lighter than Hg," *Soviet Journal of Nuclear Physics*, vol. 53, no. 5, pp. 757–763, 1991.

[39] M. Caamaño, O. Delaune, F. Farget, X. Derkx, K.-H. Schmidt, L. Audouin, C.-O. Bacri, G. Barreau, J. Benlliure, E. Casarejos, A. Chbihi, B. Fernández-Domínguez, L. Gaudefroy, C. Golabek, B. Jurado, A. Lemasson, A. Navin, M. Rejmund, T. Roger, A. Shrivastava, and C. Schmitt, "Isotopic yield distributions of transfer- and fusion-induced fission from ^{238}U + ^{12}C reactions in inverse kinematics," *Physical Review C*, vol. 88, p. 024605, Aug. 2013.

[40] E. Pellereau, G. Bélier, G. Boutoux, A. Chatillon, A. Ebran, T. Gorbinet, B. Laurent, J.-F. Martin, J. Taieb, L. Audouin, L. Tassan-Got, B. Jurado, H. Álvarez Pol, Y. Ayyad, J. Benlliure, M. Caamaño, D. Cortina-Gil, B. Fernández-Domínguez, C. Paradela, J. Rodríguez-Sánchez, J. Vargas, E. Casarejos, A. Heinz, A. Kelić-Heil, N. Kurz, C. Nociforo, S. Pietri, A. Prochazka, D. Rossi, K.-H. Schmidt, H. Simon, B. Voss, H. Weick, and

J. Winfield, "SOFIA: An innovative setup to measure complete isotopic yield of fission fragments," *EPJ Web of Conferences*, vol. 62, p. 06005, Dec. 2013.

[41] P. Möller, A. J. Sierk, T. Ichikawa, A. Iwamoto, and M. Mumpower, "Fission barriers at the end of the chart of the nuclides," *Physical Review C*, vol. 91, no. 2, p. 024310, 2015.

[42] A. N. Andreyev, M. Huyse, and P. Van Duppen, "Colloquium: Beta-delayed fission of atomic nuclei," *Reviews of Modern Physics*, vol. 85, pp. 1541–1559, Oct. 2013.

[43] V. I. Kuznetsov, N. K. Skobelev, and G. N. Flerov, "Spontaneously Fissile Neutron-Deficient Neptunium Isotope with 60-sec Half-Life," *Soviet Journal of Nuclear Physics*, vol. 4, p. 202, 1967.

[44] V. I. Kuznetsov, N. K. Skobelev, and G. N. Flerov, "Study of Spontaneously Fissile Products in Nuclear Reactions ^{230}Th+ ^{10}B and ^{230}Th+ ^{11}B," *Sov. J. Nucl. Phys*, vol. 5, p. 191, 1967.

[45] Y. A. Lazarev, Y. T. Oganessian, I. Shirokovsky, S. Tretyakova, V. K. Utyonkov, and G. V. Buklanov, "Beta-Delayed Fission of Extremely Proton-Rich Nuclei in the Region of Mercury to Polonium," *6th International Conference on Nuclei far from Stability and 9th International Conference on Atomic Masses and Fundamental Constants, Bernkastel-Kues, Germany, July 19-24,1992*, vol. 132, pp. 739–741, 1993.

[46] A. N. Andreyev, D. D. Bogdanov, S. Saro, G. M. Ter-Akopian, M. Veselsky, and A. V. Yeremin, "Fission barrier heights for the ultra neutron-deficient nuclei ^{188}Pb and ^{196}Po," *Physics Letters B*, vol. 312, pp. 49–52, 1993.

[47] J. Elseviers, A. N. Andreyev, M. Huyse, P. Van Duppen, S. Antalic, A. Barzakh, N. Bree, T. E. Cocolios, V. F. Comas, J. Diriken, D. Fedorov, V. N. Fedosseev, S. Franchoo, L. Ghys, J. A. Heredia, O. Ivanov, U. Köster, B. A. Marsh, K. Nishio, R. D. Page, N. Patronis, M. D. Seliverstov, I. Tsekhanovich, P. Van den Bergh, J. Van De Walle, M. Venhart, S. Vermote, M. Veselský, and C. Wagemans, "β-delayed fission of ^{180}Tl," *Physical Review C*, vol. 88, no. 4, p. 044321, 2013.

[48] J. F. W. Lane, A. N. Andreyev, S. Antalic, D. Ackermann, J. Gerl, F. P. Hessberger, S. Hofmann, M. Huyse, H. Kettunen, A. Kleinböhl, B. Kindler, I. Kojouharov, M. Leino, B. Lommel, G. Münzenberg, K. Nishio, R. D. Page, S. Šáro, H. Schaffner, M. J. Taylor, and P. Van Duppen, "β-delayed fission of ^{186,188}Bi isotopes," *Physical Review C*, vol. 87, p. 014318, Jan. 2013.

[49] A. N. Andreyev, S. Antalic, D. Ackermann, L. Bianco, S. Franchoo, S. Heinz, F. P. Hessberger, S. Hofmann, M. Huyse, Z. Kalaninová, I. Kojouharov, B. Kindler, B. Lommel, R. Mann, K. Nishio, R. D. Page, J. J. Ressler, B. Streicher, S. Šáro, B. Sulignano, and P. VanDuppen, "β-delayed fission of ^{192,194}At," *Physical Review C*, vol. 87, p. 014317, Jan. 2013.

[50] Z. Kalaninová, S. Antalic, A. N. Andreyev, F. P. Hessberger, D. Ackermann, B. Andel, L. Bianco, S. Hofmann, M. Huyse, B. Kindler, B. Lommel, R. Mann, R. D. Page, P. J. Sapple, J. Thomson, P. Van Duppen, and M. Venhart, "Decay of $^{201-203}$Ra and $^{200-202}$Fr," *Physical Review C*, vol. 89, p. 054312, May 2014.

[51] E. K. Hulet, J. F. Wild, R. J. Dougan, R. W. Lougheed, J. H. Landrum, A. D. Dougan, M. Schädel, R. L. Hahn, P. A. Baisden, C. M. Henderson, R. J. Dupzyk, K. Sümmerer, and G. R. Bethune, "Bimodal symmetric fission observed in the heaviest elements," *Physical review letters*, vol. 56, no. 4, pp. 313–316, 1986.

[52] E. K. Hulet, J. F. Wild, R. J. Dougan, R. W. Lougheed, J. H. Landrum, A. D. Dougan, P. A. Baisden, C. M. Henderson, R. J. Dupzyk, R. L. Hahn, M. Schädel, K. Sümmerer, and G. R. Bethune, "Spontaneous fission properties of ^{258}Fm, ^{259}Md, ^{260}Md,^{258}No, and ^{260}[104]: Bimodal fission," *Physical Review C*, vol. 40, pp. 770–784, Aug. 1989.

[53] H. C. Britt, H. E. Wegner, and J. C. Gursky, "Energetics of charged particle-induced fission reactions," *Physical Review*, vol. 129, no. 5, pp. 2239–2252, 1963.

[54] E. Konecny and H. W. Schmitt, "Fission Energetics and Neutron Emission in 13-MeV Proton-Induced Fission of ^{226}Ra," *Physical Review*, vol. 172, no. 4, pp. 1213–1226, 1968.

[55] E. Konecny, H. J. Specht, and J. Weber, "Symmetric and asymmetric fission of Ra and Ac isotopes," in *Third IAEA Symposium on Physics and Chemistry of Fission*, pp. 3–18, 1974.

[56] U. Brosa, S. Grossmann, and A. Müller, "Nuclear scission," *Physics Reports*, vol. 197, pp. 167–262, Dec. 1990.

[57] P. Möller, D. G. Madland, A. J. Sierk, and A. Iwamoto, "Nuclear fission modes and fragment mass asymmetries in a five-dimensional deformation space," *Nature*, vol. 409, no. 6822, pp. 785–790, 2001.

[58] K. H. Schmidt and B. Jurado, "Global view on fission observables – new insights and new puzzles," *Physics Procedia*, vol. 31, pp. 147–157, 2012.

[59] K. Flynn, E. P. Horwitz, C. A. A. Bloomquist, R. F. Barnes, R. K. Sjoblom, P. R. Fields, and L. E. Glendenin, "Distribution of Mass in Spontaneous Fission of ^{256}Fm," *Physical Review C*, vol. 5, no. 5, pp. 1725–1729, 1972.

[60] P. Möller, J. Randrup, and A. J. Sierk, "Calculated fission yields of neutron-deficient mercury isotopes," *Physical Review C*, vol. 85, p. 024306, Feb. 2012.

[61] M. Warda, A. Staszczak, and W. Nazarewicz, "Fission modes of mercury isotopes," *Physical Review C*, vol. 86, p. 024601, Aug. 2012.

[62] S. Panebianco, J.-L. Sida, H. Goutte, J.-F. Lemaître, N. Dubray, and S. Hilaire, "Role of deformed shell effects on the mass asymmetry in nuclear fission of mercury isotopes," *Physical Review C*, vol. 86, p. 064601, Dec. 2012.

[63] A. V. Andreev, G. G. Adamian, and N. V. Antonenko, "Mass distributions for induced fission of different Hg isotopes," *Physical Review C*, vol. 86, p. 044315, Oct. 2012.

[64] Y. Oganessian, "Heaviest nuclei from ^{48}Ca-induced reactions," *Journal of Physics G: Nuclear and Particle Physics*, vol. 34, no. 4, pp. R165–R242, 2007.

[65] V. M. Strutinsky, "Shell effects in nuclear masses and deformation energies," *Nuclear Physics A*, vol. 95, no. 2, pp. 420–442, 1967.

[66] V. M. Strutinsky, ""Shells" in deformed nuclei," *Nuclear Physics A*, vol. 122, no. 1, pp. 1–33, 1968.

[67] P. Moller, J. R. Nix, and W. J. Swiatecki, "New developments in the calculation of heavy-element fission barriers," *Nuclear Physics A*, vol. 492, pp. 349–387, 1989.

[68] H. J. Krappe, J. R. Nix, and A. J. Sierk, "Unified nuclear potential for heavy-ion elastic scattering, fusion, fission, and ground-state masses and deformations," *Physical Review C*, vol. 20, no. 3, pp. 992–1013, 1979.

[69] P. Möller and J. R. Nix, "Nuclear mass formula with a Yukawa-plus-exponential macroscopic model and a folded-Yukawa single-particle potential," *Nuclear Physics A*, vol. 361, no. 1, pp. 117–146, 1981.

[70] P. Möller and J. R. Nix, "Nuclear pairing models," *Nuclear Physics A*, vol. 536, pp. 20–60, 1992.

[71] P. Möller, A. J. Sierk, T. Ichikawa, A. Iwamoto, R. Bengtsson, H. Uhrenholt, and S. Aberg, "Heavy-element fission barriers," *Physical Review C*, vol. 79, p. 064304, June 2009.

[72] T. Ichikawa, A. Iwamoto, P. Möller, and A. J. Sierk, "Contrasting fission potential-energy structure of actinides and mercury isotopes," *Physical Review C*, vol. 86, p. 024610, Aug. 2012.

[73] J. Randrup and P. Möller, "Brownian shape motion on five-dimensional potential-energy surfaces: Nuclear fission-fragment mass distributions," *Physical review letters*, vol. 106, no. April, p. 132503, 2011.

[74] L. Ghys, A. N. Andreyev, M. Huyse, P. Van Duppen, S. Sels, B. Andel, S. Antalic, A. Barzakh, L. Capponi, T. E. Cocolios, X. Derkx, H. De Witte, J. Elseviers, D. V. Fedorov, V. N. Fedosseev, F. P. Hessberger, Z. Kalaninová, U. Köster, J. F. W. Lane, V. Liberati, K. M. Lynch, B. A. Marsh, S. Mitsuoka, P. Möller, Y. Nagame, K. Nishio, S. Ota, D. Pauwels, R. D. Page, L. Popescu, D. Radulov, M. M. Rajabali, J. Randrup, E. Rapisarda, S. Rothe, K. Sandhu, M. D. Seliverstov, A. M. Sjödin, V. L. Truesdale, C. Van Beveren, P. Van den Bergh, Y. Wakabayashi, and M. Warda, "Evolution of fission-fragment mass distributions in the neutron-deficient lead region," *Physical Review C*, vol. 90, p. 041301, Oct. 2014.

[75] W. D. Myers and W. J. Swiatecki, "A Thomas-Fermi Model of Nuclei. Part I . Formulation and First Results.," *Annals of physics*, vol. 204, pp. 401–431, 1990.

[76] W. D. Myers and W. J. Swiatecki, "Nuclear properties according to the Thomas-Fermi model," *Nuclear Physics A*, vol. 601, pp. 141–167, May 1996.

[77] W. D. Myers and W. J. Swiatecki, "The congruence energy: a contribution to nuclear masses, deformation energies and fission barriers," *Nuclear Physics A*, vol. 612, pp. 249–261, Jan. 1997.

[78] P. Ring and P. Schuck, *The Nuclear Many-Body Problem*. Springer-Verlag, 1980.

[79] M. Bender, P.-H. Heenen, and P.-G. Reinhard, "Self-Consistent Mean-Field Models for Nuclear Structure and Dynamics," *Reviews of Modern Physics*, vol. 75, pp. 121–153, 2003.

[80] D. Vautherin and D. M. Brink, "Hartree-fock calculations with skyrme's interaction. I. Spherical nuclei," *Physical Review C*, vol. 5, no. 3, pp. 626–647, 1972.

[81] D. Gogny, "Proceedings of the International Conference on Nuclear Physics, Munich, 1973," 1973.

[82] J. Berger and D. Gogny, "A self-consistent microscopic approach to the $^{12}C+^{12}C$ reaction at low energy," *Nuclear Physics A*, vol. 333, no. 2, pp. 302–332, 1980.

[83] J. Walecka, "A theory of highly condensed matter," *Annals of Physics*, vol. 83, no. 2, pp. 491–529, 1974.

[84] J. Boguta and A. R. Bodmer, "Relativistic calculation of nuclear matter and the nuclear surface," *Nuclear Physics A*, vol. 292, no. 3, pp. 413–428, 1977.

[85] J. D. Mcdonnell, W. Nazarewicz, J. A. Sheikh, A. Staszczak, and M. Warda, "Excitation energy dependence of fission in the mercury region," *Physical Review C*, vol. 021302, pp. 18–23, 2014.

[86] V. Hellemans, M. Bender, and P. H. Heenen, "Octupole collectivity from a beyond-mean field point of view (presentation at the BriX meeting 2014)," 2014.

[87] B. D. Wilkins, E. P. Steinberg, and R. R. Chasman, "Scission-point model of nuclear fission based on deformed-shell effects," *Physical Review C*, 1976.

[88] S. Heinrich, *Développement d ' un nouveau modèle de point de scission , basé sur des ingrédients microscopiques.* PhD thesis, Université Paris XI, 2006.

[89] "`http://te-dep-epc.web.cern.ch/te-dep-epc/machines/pagesources/Cern-Accelerator-Complex.jpg`."

[90] E. Kugler, "The ISOLDE facility," *Hyperfine Interactions*, vol. 129, pp. 23–42, 2000.

[91] P. Van Duppen, *The Euroschool Lectures on Physics With Exotic Beams, Vol. II: Isotope Separation On Line and Post Acceleration*, vol. 700. Springer-Verlag Berlin Heidelberg, 2006.

[92] S. Rothe, A. N. Andreyev, S. Antalic, A. Borschevsky, L. Capponi, T. E. Cocolios, H. De Witte, E. Eliav, D. V. Fedorov, V. N. Fedosseev, D. A. Fink, S. Fritzsche, L. Ghys, M. Huyse, N. Imai, U. Kaldor, Y. Kudryavtsev, U. Köster, J. F. W. Lane, J. Lassen, V. Liberati, K. M. Lynch, B. A. Marsh, K. Nishio, D. Pauwels, V. Pershina, L. Popescu, T. J. Procter, D. Radulov, S. Raeder, M. M. Rajabali, E. Rapisarda, R. E. Rossel, K. Sandhu, M. D. Seliverstov, A. M. Sjödin, P. Van den Bergh, P. Van Duppen, M. Venhart, Y. Wakabayashi, and K. D. A. Wendt, "Measurement of the first ionization potential of astatine by laser ionization spectroscopy.," *Nature communications*, vol. 4, no. May, p. 1835, 2013.

[93] M. J. G. Borge, "ISOLDE highlights and the HIE-ISOLDE project," *EPJ Web of Conferences*, vol. 66, p. 11005, 2014.

[94] M. Wang, G. Audi, A. H. Wapstra, F. G. Kondev, M. MacCormick, X. Xu, and B. Pfeiffer, "The AME2012 atomic mass evaluation," *Chinese Physics C*, vol. 36, pp. 1603–2014, Dec. 2012.

[95] J. Camplan, "Ion optics of isotope separators," 1981.

[96] N. Bree, *Shape coexistence in the neutron-deficient mercury isotopes studied through Coulomb excitation.* PhD thesis, KU Leuven, 2014.

[97] "`http://www.xia.com/`."

[98] G. Bortels and P. Collaers, "Analytical function for fitting peaks in alpha-particle spectra from Si detectors," *International Journal of Radiation Applications and Instrumentation. Part A. Applied Radiation and Isotopes*, vol. 38, pp. 831–837, 1987.

[99] A. N. Andreyev, S. Antalic, D. Ackermann, L. Bianco, S. Franchoo, S. Heinz, F. P. Hessberger, S. Hofmann, M. Huyse, I. Kojouharov, B. Kindler, B. Lommel, R. Mann, K. Nishio, R. D. Page, J. J. Ressler, P. Sapple, B. Streicher, S. Šáro, B. Sulignano, J. Thomson, P. Van Duppen, and M. Venhart, "α decay of ^{194}At," *Physical Review C*, vol. 79, p. 064320, June 2009.

[100] J. Tuli and T. Johnson, "http://www.nndc.bnl.gov/ensdf/."

[101] J. Cubiss et al., "*in preparation.*" 2015.

[102] S. Sels, "β -delayed fission and α -decay spectroscopy of ^{194,196}At (Master Thesis, KU Leuven)," 2013.

[103] V. L. Truesdale et al. *(to be submitted)*, "beta- delayed fission and alpha decay of ^{196}At," 2015.

[104] L. Ghys et al., "α decay study of ^{202}Fr-^{198}At-^{194}Bi at ISOLDE-CERN (in preparation)." 2015.

[105] J. Wauters, P. Dendooven, M. Huyse, G. Reusen, P. Van Duppen, and P. Lievens, "α-decay properties of neutron-deficient polonium and radon nuclei," *Physical Review C*, vol. 47, pp. 1447–1454, Apr. 1993.

[106] G. F. Knoll, *Radiation Detection and Measurement.* John Wiley & Sons, 2010.

[107] E. C. Finch, M. Asghar, M. Forte, G. Siegert, J. Greif, and D. Recker, "The response of a surface barrier detector to mass and energy separated fission fragments," *Nuclear Instruments and Methods*, vol. 142, pp. 539–552, 1977.

[108] B. Wilkins, M. Fluss, S. Kaufman, C. Gross, and E. Steinberg, "Pulse-height defects for heavy ions in a silicon surface-barrier detector," *Nuclear Instruments and Methods*, vol. 92, pp. 381–391, Apr. 1971.

[109] M. Ogihara, Y. Nagashima, W. Galster, and T. Mikumo, "Systematic measurements of pulse height defects for heavy ions in surface-barrier detectors," *Nuclear Instruments and Methods in Physics Research A*, vol. 251, pp. 313–320, 1986.

[110] H. W. Schmitt, W. E. Kiker, and C. W. Williams, "Precision Measurements of Correlated Energies and Velocities of 252Cf Fission Fragments," *Physical Review*, vol. 137, no. 1964, pp. B837–B847, 1965.

[111] E. C. Finch, "An analysis of the pulse height defect and its mass dependence for heavy-ion silicon detectors," *Nuclear Instruments and Methods*, vol. 113, pp. 41–49, 1973.

[112] J. B. Moulton, J. E. Stephenson, R. P. Schmitt, and G. J. Wozniak, "A new method for calibrating the pulse-height defect in solid state detectors," 1978.

[113] A. Menchaca-Rocha, J. I. Cabrera, R. Alfaro, E. Belmont-Moreno, and A. Martínez-Dávalos, "A new approach to deal with non-linearities in Si detector response," *Nuclear Instruments and Methods in Physics Research, Section B: Beam Interactions with Materials and Atoms*, vol. 207, pp. 356–367, 2003.

[114] L. Demattè, *Investigation of the fission fragments' mass and energy distributions of* ^{236,238,240,242,244}*Pu (SF)*. PhD thesis, University of Ghent, 1996.

[115] J. F. Ziegler, "The Stopping and Range of Ions in Matter (SRIM computer program)," 2013.

[116] J. Elseviers, "Electron capture delayed fission of ^{180}Tl (Master Thesis, KU Leuven)," 2009.

[117] H. L. Hall and D. C. Hoffman, "Low-energy nuclear fission and our understanding of the nucleus," *Journal of radioanalytical and nuclear chemistry*, vol. 142, no. 1, pp. 53–78, 1990.

[118] J. F. Berger, M. Girod, and D. Gogny, "Microscopic analysis of collective dynamics in low energy fission," *Nuclear Physics A*, vol. 428, pp. 23c–26c, 1984.

[119] P. Möller, J. R. Nix, and W. J. Swiatecki, "Calculated fission properties of the heaviest elements," *Nuclear Physics A*, vol. 469, pp. 1–50, July 1987.

[120] S. Ćwiok, P. Rozmej, A. Sobiczewski, and Z. Patyk, "Two fission modes of the heavy fermium isotopes," *Nuclear Physics A*, vol. 491, pp. 281–289, Jan. 1989.

[121] A. V. Andreev, G. G. Adamian, N. V. Antonenko, and A. N. Andreyev, "Isospin dependence of mass-distribution shape of fission fragments of Hg isotopes," *Physical Review C*, vol. 88, p. 047604, Oct. 2013.

[122] J. Randrup and P. Möller, "Energy dependence of fission-fragment mass distributions from strongly damped shape evolution," *Physical Review C*, vol. 88, p. 064606, Dec. 2013.

[123] M. D. Seliverstov, T. E. Cocolios, W. Dexters, A. N. Andreyev, S. Antalic, A. E. Barzakh, B. Bastin, J. Büscher, I. G. Darby, D. V. Fedorov, V. N. Fedosseev, K. T. Flanagan, S. Franchoo, G. Huber, M. Huyse, M. Keupers, U. Köster, Y. Kudryavtsev, B. A. Marsh, P. L. Molkanov, R. D. Page, A. M. Sjödin, I. Stefan, P. Van Duppen, M. Venhart, and S. G. Zemlyanoy, "Electromagnetic moments of odd-A $^{193-203,211}$Po isotopes," *Physical Review C*, vol. 89, p. 034323, Mar. 2014.

[124] M. Huyse, P. Decrock, P. Dendooven, G. Reusen, P. Van Duppen, and J. Wauters, "Isomers in three doubly odd Fr-At-Bi alpha-decay chains," *Physical Review C*, vol. 46, no. 4, pp. 1209–1217, 1992.

[125] V. N. Fedosseev, D. V. Fedorov, R. Horn, G. Huber, U. Köster, J. Lassen, V. I. Mishin, M. D. Seliverstov, L. Weissman, and K. Wendt, "Atomic spectroscopy studies of short-lived isotopes and nuclear isomer separation with the ISOLDE RILIS," *Nuclear Instruments and Methods in Physics Research Section B: Beam Interactions with Materials and Atoms*, vol. 204, pp. 353–358, May 2003.

[126] K. T. Flanagan, K. M. Lynch, J. Billowes, M. L. Bissell, I. Budinčević, T. E. Cocolios, R. P. de Groote, S. De Schepper, V. N. Fedosseev, S. Franchoo, R. F. Garcia Ruiz, H. Heylen, B. A. Marsh, G. Neyens, T. J. Procter, R. E. Rossel, S. Rothe, I. Strashnov, H. H. Stroke, and K. D. A. Wendt, "Collinear Resonance Ionization Spectroscopy of Neutron-Deficient Francium Isotopes," *Physical Review Letters*, vol. 111, p. 212501, Nov. 2013.

[127] K. M. Lynch, J. Billowes, M. L. Bissell, I. Budinčević, T. E. Cocolios, R. P. De Groote, S. De Schepper, V. N. Fedosseev, K. T. Flanagan, S. Franchoo, R. F. Garcia Ruiz, H. Heylen, B. A. Marsh, G. Neyens, T. J. Procter, R. E. Rossel, S. Rothe, I. Strashnov, H. H. Stroke, and K. D. A. Wendt, "Decay-Assisted Laser Spectroscopy of Neutron-Deficient Francium," *Physical Review X*, vol. 4, p. 011055, Mar. 2014.

[128] L. M. Robledo, "HFBaxial code," 2002.

[129] J. L. Egido, L. M. Robledo, and R. R. Chasman, "Nuclear shapes in 176 W with density dependent forces: from ground state to fission," *Physics Letters B*, vol. 393, no. February, pp. 13–18, 1997.

[130] J. Randrup, P. Möller, and A. J. Sierk, "Fission-fragment mass distributions from strongly damped shape evolution," *Physical Review C*, vol. 84, p. 034613, 2011.

[131] P. Möller and J. r. Randrup, "Calculated fission-fragment yield systematics in the region $74 \leq Z \leq 94$ and $90 \leq N \leq 150$," *Physical Review C*, vol. 91, no. 4, p. 044316, 2015.

[132] L. Ghys, A. N. Andreyev, S. Antalic, M. Huyse, and P. Van Duppen, "Empirical description of β -delayed fission partial half-lives," *Physical Review C*, vol. 91, no. 4, pp. 1–7, 2015.

[133] D. A. Shaughnessy, J. L. Adams, K. E. Gregorich, M. R. Lane, C. A. Laue, D. M. Lee, C. A. McGrath, J. B. Patin, D. A. Strellis, E. R. Sylwester, P. A. Wilk, and D. C. Hoffman, "Electron-capture delayed fission properties of ^{242} Es," *Physical Review C*, vol. 61, p. 044609, Nov. 2000.

[134] D. A. Shaughnessy, K. E. Gregorich, J. L. Adams, M. R. Lane, C. A. Laue, D. M. Lee, C. A. McGrath, V. Ninov, J. B. Patin, D. A. Strellis, E. R. Sylwester, P. A. Wilk, and D. C. Hoffman, "Electron-capture delayed fission properties of ^{244}Es," *Physical Review C*, vol. 65, p. 024612, Jan. 2002.

[135] H. Britt, E. Cheifetz, D. Hoffman, J. Wilhelmy, R. Dupzyk, and R. Lougheed, "Fission barriers for ^{255}Es, ^{256}Es, and ^{255}Fm," *Physical Review C*, vol. 21, pp. 761–763, Feb. 1980.

[136] Y. P. Gangrsky, M. B. Miller, L. V. Mikhailov, and I. F. Kharisov, "Study of Delayed Fission of Bk, Es, Md Isotopes," *Soviet Journal of Nuclear Physics*, vol. 31, p. 162, 1980.

[137] K. L. Kratz and G. Herrmann, "Systematics of neutron emission probabilities from delayed neutron precursors," *Zeitschrift für Physik*, vol. 263, pp. 435–442, Oct. 1973.

[138] P. Hornshoj, B. R. Erdal, P. G. Hansen, B. Jonson, K. Aleklett, and G. Nyman, "Beta-strength functions of neutron-deficient isotopes in the xenon and mercury regions," *Nuclear Physics A*, vol. 239, pp. 15–28, 1974.

[139] D. Habs, H. Klewe-Nebenius, V. Metag, B. Neumann, and H. J. Specht, "Determination of the Fission Barrier of ^{232}Pu from β-Delayed Fission and the Problem of the First Barrier," *Zeitschrift für Physik A Atoms and Nuclei*, vol. 285, pp. 53–57, 1978.

[140] M. Emeric and A. Sonzogni, "`http://www.nndc.bnl.gov/logft/`."

[141] V. Zagrebaev, A. Denikin, A. P. Alekseev, A. V. Karpov, V. V. Samarin, M. A. Naumenko, and A. Y. Kozhin, "`http://nrv.jinr.ru/nrv/`."

[142] P. Möller, J. R. Nix, and K.-L. Kratz, "Nuclear properties for astrophysical and radioactive-ion-beam applications," *Atomic Data and Nuclear Data Tables*, vol. 66, pp. 131–343, July 1997.

[143] S. A. Kreek, H. L. Hall, K. E. Gregorich, R. A. Henderson, J. D. Leyba, K. R. Czerwinski, B. Kadkhodayan, M. P. Neu, C. D. Kacher, T. M. Hamilton, M. R. Lane, E. R. Sylwester, A. Türler, D. M. Lee, M. J. Nurmia, and D. C. Hoffman, "Electron-capture delayed fission properties of ^{228}Np," *Physical Review C*, vol. 50, pp. 2288–2296, Nov. 1994.

[144] H. L. Hall, K. E. Gregorich, R. A. Henderson, C. M. Gannett, R. B. Chadwick, J. D. Leyba, K. R. Czerwinski, B. Kadkhodayan, S. A. Kreek, N. J. Hannink, D. M. Lee, M. J. Nurmia, D. C. Hoffman, C. E. A. Palmer, and P. A. Baisden, "Electron-capture-delayed fission properties of ^{232}Am," *Physical Review C*, vol. 42, pp. 1480–1488, Oct. 1990.

[145] H. L. Hall, K. E. Gregorich, R. A. Henderson, C. M. Gannett, R. B. Chadwick, J. D. Leyba, K. R. Czerwinski, B. Kadkhodayan, S. A. Kreek, D. M. Lee, M. J. Nurmia, and D. C. Hoffman, "Electron-capture-delayed fission properties of ^{234}Am," *Physical Review C*, vol. 41, no. 2, pp. 618–630, 1990.

[146] S. A. Kreek, H. L. Hall, K. E. Gregorich, R. A. Henderson, J. D. Leyba, K. R. Czerwinski, B. Kadkhodayan, M. P. Neu, C. D. Kacher, T. M. Hamilton, M. R. Lane, E. R. Sylwester, A. Türler, D. M. Lee, M. J. Nurmia, and D. C. Hoffman, "Electron-capture delayed fission properties of the new isotope ^{238}Bk," *Physical Review C*, vol. 49, no. 4, 1994.

[147] D. Galeriu, "The beta strength function of ^{240}Bk and the fission barrier of neutron-deficient actinides," *Journal of Physics G: Nuclear Physics*, vol. 9, pp. 309–317, 1983.

[148] S. Antalic, F. P. Hessberger, S. Hofmann, D. Ackermann, S. Heinz, B. Kindler, I. Kojouharov, P. Kuusiniemi, M. Leino, B. Lommel, R. Mann, and S. Šáro, "Studies of neutron-deficient mendelevium isotopes at SHIP," *The European Physical Journal A*, vol. 43, pp. 35–44, Nov. 2010.

[149] D. A. Shaughnessy, K. E. Gregorich, M. R. Lane, C. A. Laue, D. M. Lee, C. A. McGrath, D. A. Strellis, E. R. Sylwester, P. A. Wilk, and D. C. Hoffman, "Electron-capture delayed fission probabilities of ^{248}Es and ^{246}Es," *Physical Review C*, vol. 63, p. 037603, Feb. 2001.

[150] X. Yanbing, Z. Shengdong, D. Huajie, Y. Shuanggui, Y. Weifan, N. Yanning, L. Xiting, L. Yingjun, and X. Yonghou, "Search for β-delayed fission of ^{228}Ac," *Physical Review C*, vol. 74, p. 047303, Oct. 2006.

[151] Y. Shuanggui, Y. Weifan, X. Yanbing, P. Qiangyan, X. Bing, H. Jianjun, W. Dong, L. Yingjun, M. Taotao, and Y. Zhenguo, "Search for β-delayed fission of the heavy neutron-rich isotope ^{230}Ac," *The European Physical Journal A*, vol. 10, pp. 1–3, Feb. 2001.

[152] Y. P. Gangrsky, G. M. Marinesky, M. B. Miller, V. N. Samsuk, and I. F. Kharisov, "No Title," *Soviet Journal of Nuclear Physics*, vol. 27, p. 475, 1978.

[153] A. Baas-May, J. V. Kratz, and N. Trautmann, "Absence of delayed fission in the beta-decay of 2.3 min ^{238}Pa," *Zeitschrift für Physik A Atoms and Nuclei*, vol. 322, pp. 457–462, Sept. 1985.

[154] H. Hall, K. Gregorich, R. Henderson, D. Lee, D. Hoffman, M. Bunker, M. Fowler, P. Lysaght, J. Starner, and J. Wilhelmy, "β-delayed fission from ^{256}Es and the level scheme of ^{256}Fm," *Physical Review C*, vol. 39, pp. 1866–1875, May 1989.

[155] K. Morita, K. Morimoto, D. Kaji, S. Goto, H. Haba, E. Ideguchi, R. Kanungo, K. Katori, H. Koura, H. Kudo, T. Ohnishi, A. Ozawa, J. C. Peter, T. Suda, K. Sueki, I. Tanihata, F. Tokanai, H. Xu, A. V. Yeremin, A. Yoneda, A. Yoshida, Y.-L. Zhao, and T. Zheng, "Status of heavy element research using GARIS at RIKEN," *Nuclear Physics A*, vol. 734, pp. 101–108, Apr. 2004.

[156] "`http://isolde.web.cern.ch/experiments/isolde-decay-station-ids`."

[157] S. Gales, "SPIRAL2 at GANIL: Next Generation of ISOL Facility for Intense Secondary Radioactive Ion Beams," *Nuclear Physics A*, vol. 834, no. 1-4, pp. 717c–723c, 2010.

[158] R. Ferrer, B. Bastin, D. Boilley, P. Creemers, P. Delahaye, E. Liénard, X. Fléchard, S. Franchoo, L. Ghys, M. Huyse, Y. Kudryavtsev, N. Lecesne, H. Lu, F. Lutton, E. Mogilevskiy, D. Pauwels, J. Piot, D. Radulov, L. Rens, H. Savajols, J. Thomas, E. Traykov, C. Van Beveren, P. Van den Bergh, and P. Van Duppen, "In gas laser ionization and spectroscopy experiments at the Superconducting Separator Spectrometer (S3): Conceptual studies and preliminary design," *Nuclear Instruments and Methods in Physics Research Section B: Beam Interactions with Materials and Atoms*, vol. 317, pp. 570–581, Dec. 2013.

[159] "`http://isolmyrrha.sckcen.be/`."

[160] "`http://www.ill.eu/instruments-support/instruments-groups/instruments/pn1/`."

[161] "`http://www.canberra.com/products/detectors/pdf/passivated_pips_C39313a.pdf`."

[162] "`http://www.ortec-online.com/download/ORTEC-Catalog-Detectors-Section.pdf`."

[163] H. De Witte, A. N. Andreyev, N. Barré, M. Bender, T. E. Cocolios, S. Dean, D. Fedorov, V. N. Fedoseyev, L. M. Fraile, S. Franchoo, V. Hellemans, P.-H. Heenen, K. Heyde, G. Huber, M. Huyse, H. Jeppessen, U. Köster, P. Kunz, S. R. Lesher, B. A. Marsh, I. Mukha, B. Roussière, J. Sauvage, M. Seliverstov, I. Stefanescu, E. Tengborn, K. Van de Vel, J. Van de Walle, P. Van Duppen, and Y. Volkov, "Nuclear Charge Radii of Neutron-Deficient Lead Isotopes Beyond N=104 Midshell Investigated by In-Source Laser Spectroscopy," *Physical Review Letters*, vol. 98, p. 112502, Mar. 2007.

[164] T. E. Cocolios, W. Dexters, M. D. Seliverstov, a. N. Andreyev, S. Antalic, a. E. Barzakh, B. Bastin, J. Büscher, I. G. Darby, D. V. Fedorov, V. N. Fedosseyev, K. T. Flanagan, S. Franchoo, S. Fritzsche, G. Huber, M. Huyse, M. Keupers, U. Köster, Y. Kudryavtsev, E. Mané, B. a. Marsh, P. L. Molkanov, R. D. Page, a. M. Sjoedin, I. Stefan, J. Van De Walle, P. Van Duppen, M. Venhart, S. G. Zemlyanoy, M. Bender, and P. H. Heenen, "Early onset of ground state deformation in neutron deficient polonium isotopes," *Physical Review Letters*, vol. 106, no. 5, pp. 1–4, 2011.

[165] D. A. Fink, T. E. Cocolios, A. N. Andreyev, S. Antalic, A. E. Barzakh, B. Bastin, D. V. Fedorov, V. N. Fedosseev, K. T. Flanagan, L. Ghys, A. Gottberg, M. Huyse, N. Imai, T. Kron, N. Lecesne, K. M. Lynch, B. A. Marsh, D. Pauwels, E. Rapisarda, S. D. Richter, R. E. Rossel, S. Rothe, M. D. Seliverstov, A. M. Sjödin, C. Van Beveren, P. Van Duppen, and

K. D. A. Wendt, "In-Source Laser Spectroscopy with the Laser Ion Source and Trap: First Direct Study of the Ground-State Properties of Po217,219," *Physical Review X*, vol. 5, no. 1, p. 011018, 2015.

[166] T. E. Cocolios, *Single-Particle and Collective Properties around Closed Shells probed by In-Source Laser Spectroscopy*. PhD thesis, KU Leuven, 2010.

[167] C. Van Beveren, "PhD thesis (in preparation)," 2015.

FACULTY OF SCIENCE
DEPARTEMENT OF PHYSICS AND ASTRONOMY
INSTITUTE FOR NUCLEAR AND RADIATION PHYSICS
Celestijnenlaan 200D box 2418
B-3001 Heverlee
lars.ghys@fys.kuleuven.be
https://fys.kuleuven.be/iks